UNIVERSITY OF CALIFORNIA SAN DIEGO

Seismogeodetic Studies of the Crustal Deformation Cycle for Hazards Mitigation

A dissertation submitted in partial satisfaction of the
requirements for the degree Doctor of Philosophy

in

Earth Sciences

by

Dorian Golriz

Committee in charge:

Yehuda Bock, Chair
Wenyuan Fan
David T. Sandwell
Lisa Tauxe
Michael D. Todd

2023

The Dissertation of Dorian Golriz is approved, and it is acceptable in quality and form for publication on microfilm and electronically.

University of California San Diego

2023

DEDICATION

To my father, who always saw the beauty of nature.

TABLE OF CONTENTS

LIST OF FIGURES

LIST OF TABLES

ACKNOWLEDGEMENTS

I feel very fortunate to complete my PhD here at Scripps, UC San Diego, surrounded by the leading scientists in the Geophysics field. That would not be possible without the help and support of several people in my life which I am grateful for. First and foremost, I want to thank my advisor Yehuda Bock, and his family. You supported me from the moment I started my graduate degree here; from financial perspective, through endless scientific and personal discussions, holiday gatherings, and to some crucial conversations about my next steps. You knew exactly the times when I needed a push and work hard, and when it was the right time to zoom out and see the big picture as a researcher and a student. I am learning a lot from you and I am lucky to have you as my advisor. The rest of my committee - David Sandwell, Wenyuan Fan, Lisa Tauxe, and Michael Todd. Thank you for being so patient with me and my questions, for giving me the right feedback, and for helping me with this successful graduation. The dedicated staff and students of the Scripps Orbital and Permanent Array Center (SOPAC) - Maria Turingan, Anne Sullivan, Peng Fang, Song Jiang, Allen Nance, and Katherine Guns.

I would like to thank many brilliant collaborators, from all corners of the globe. Xiaohua Xu from the University of Science and Technology of China - for numerous lessons about earthquake slip inversions and satellite SAR imagery processing. Barry Hirshorn, an excellent and modest seismologist, for educating me about different seismological aspects and Earthworm modules. Stuart Weinstein and Jonathan Weiss from the Pacific Tsunami Warning Center in Hawaii, for constructive feedback and scientific communications on a bi-weekly basis. Angelyn Moore, Donald Argus, and Zhen Liu from the National Aeronautics and Space Administration (NASA) Jet Propulsion Laboratory (JPL) for being part of the MEaSUREa group. Yariv Hamiel from the Geological Survey of Israel, for providing great datasets and your professional opinion, and teaching me about every single fracture in the Dead Sea Fault region.

My cohort - Nicolas Blanc, Andi Adams, Hugh Harper, Zeyu Jin, Margaret Morris, and Roz King. Thank you for sticking together through COVID-19 era and not missing the opportunity to hang-out with a slice of pizza, a beer, or a casual potluck. Thank you the rest

of the students, postdocs, and faculty from the Institute of Geophysics and Planetary Physics (IGPP) and Scripps. Special thanks to the Information Technology (IT) group at IGPP for your help and assistance.

Thank you my family and friends from Israel. For supporting me from afar through phone and video calls over the years. Last but not least, I would like to thank my best friend and my wife, Rotem. Thank you for sticking next to me all along the way. You bring me joy, happiness, and countless moments of laughter. It is not at all obvious that you are here with me. I love you so much and I am lucky to have you by my side.

Portions of this dissertation have been published or are expected to be published in peer reviewed journals.

Chapter 2, in full, is a reformatted version of material as it appears in Journal of Geophysical Research - Solid Earth: Golriz, D., Bock, Y., & Xu, X. (2021). "Defining the Coseismic Phase of the Crustal Deformation Cycle With Seismogeodesy". *Journal of Geophysical Research: Solid Earth*, 126(10), doi:10.1029/2021JB022002. The dissertation author was the primary investigator and author of this material.

Chapter 3, in full, is a reformatted version of material as it appears in Journal of Geophysical Research - Solid Earth: Golriz, D., Hirshorn, B., Bock, Y., Weinstein, S., & Weiss, J. R. (2022). "Real-Time Seismogeodetic Earthquake Magnitude Estimates for Local Tsunami Warnings". *Journal of Geophysical Research: Solid Earth*, doi:10.1029/2022JB025555. The dissertation author was the primary investigator and author of this material.

Chapter 4, in part, is currently in preparation for publication as: Golriz, D., Xu, X., Hamiel, Y., Bock, Y., & Sandwell D. T. "Interseismic Deformation in the Dead Sea Fault Region Revealed by InSAR and GNSS Measurements", *in prep.* The dissertation author was the primary investigator and author of this material.

Portions of Appendix A are currently in preparation for online repository publication

as: Golriz, D., & Bock, Y. ”High-Rate GNSS and Seismogeodetic Data Archive for Historical Earthquakes”, *in prep.* The dissertation author was the primary investigator and author of this

VITA

2015	B.S. in Geophysics, Tel-Aviv University, Israel
2017	M.S. in Geophysics, Tel-Aviv University, Israel
2021	M.S. in Earth Sciences, University of California San Diego
2023	Ph.D. in Earth Sciences, University of California San Diego

PUBLICATIONS

Golriz, D., Xu, X., Hamiel, Y., Bock, Y., & Sandwell D. T. "Interseismic Deformation in the Dead Sea Fault Region Revealed by InSAR and GNSS Measurements", *in prep.*

Golriz, D., & Bock, Y. "High-Rate GNSS and Seismogeodetic Data Archive for Historical Earthquakes", *in prep.*

Golriz, D., Hirshorn, B., Bock, Y., Weinstein, S., & Weiss, J. R. (2022). "Real-Time Seismogeodetic Earthquake Magnitude Estimates for Local Tsunami Warnings". *Journal of Geophysical Research: Solid Earth*, doi:10.1029/2022JB025555.

Golriz, D., Bock, Y., & Xu, X. (2021). "Defining the Coseismic Phase of the Crustal Deformation Cycle With Seismogeodesy". *Journal of Geophysical Research: Solid Earth*, 126(10), doi:10.1029/2021JB022002.

Klein, E., Bock, Y., Xu, X., Sandwell, D. T., **Golriz, D.**, Fang, P., & Su, L. (2019). "Transient Deformation in California from Two Decades of GPS Displacements: Implications for a Three-Dimensional Kinematic Reference Frame". *Journal of Geophysical Research: Solid Earth*, 124(11), doi:10.1029/2018JB017201

ABSTRACT OF THE DISSERTATION

Seismogeodetic Studies of the Crustal Deformation Cycle for Hazards Mitigation

by

Dorian Golriz

Doctor of Philosophy in Earth Sciences

University of California San Diego, 2023

Yehuda Bock, Chair

This dissertation presents several studies focusing on the three phases of the crustal deformation cycle. Using an optimal combination of seismic and space geodetic techniques, we investigate the coseismic phase of an earthquake that includes both shaking and permanent displacements, the postseismic phase where additional slip may occur around the affected region, and the interseismic phase over which stress builds-up at the interface between tectonic plates. Studying the crustal deformation cycle has important implications for understanding tectonic fault zone processes such as slip partitioning and strain accumulation, and to improve real-time systems for tsunami and earthquake early warnings.

We first apply a physics-based approach to identify the transition from coseismic to

postseismic deformation, and show how early postseismic is significant just minutes to hours after an earthquake. Our results show that the widely used estimates of daily coseismic offsets can lead to an overprediction of earthquake coseismic displacements. We compare the commonly used daily offsets and our rapid coseismic window methodology over several earthquakes and demonstrate that without consideration of the early postseismic stages, both coseismic and postseismic fault slip models can be biased by several meters.

We then use the coseismic time window analysis and rely on earthquake source theory to develop a rapid earthquake magnitude determination method. To test our approach, we simulate a real-time environment by replaying historical earthquakes around the Pacific basin. Our results show that we can reliably estimate earthquake magnitude over the $7.2 < M_w < 9.1$ range, minutes after rupture initiation. Incorporating long-period information from Global Navigation Satellite System (GNSS) displacements solves the problem of magnitude saturation, making these estimates useful for local tsunami warnings.

We later turn to the interseismic phase of the crustal deformation cycle by exploring more than seven years of long-term deformation along the Dead Sea Fault. For several reasons that are mostly political, GNSS station coverage in this area is not ideal with most stations on one side of the fault. For that reason we utilize the combination of GNSS station velocities and Interferometric Synthetic Aperture Radar (InSAR) imagery for a better spatial and temporal resolution representation. We detect left-lateral deformation that is in agreement with other GNSS studies and geological observations. By dividing our study area into sections, we resolve geodetic slip rates and locking depths and reveal that some segments are freely creeping in the shallow subsurface compared to others that are fully locked.

These studies present several approaches for the combination of different geophysical datasets to take advantage of their strengths while minimizing their weaknesses, to carefully study each phase of the crustal deformation cycle.

Chapter 1

Introduction

1.1 Background and Motivation

The crustal deformation cycle, also known as the earthquake cycle, is traditionally divided into three main phases: coseismic, postseismic and interseismic. In addition, the crust may experience other transient motions such as episodic tremor and slip (Rogers and Dragert, 2003), fault creep (Tymofyeyeva et al., 2019), preseismic slow slip (Mavrommatis et al., 2014), as well as magmatic and natural and anthropogenic hydrologic motions (Klein et al., 2019). In this dissertation, we investigate several aspects of crustal deformation and their physical implications using geodetic (Global Navigation Satellite Systems - GNSS, Interferometric Synthetic Aperture Radar - InSAR) and seismic (strong-motion accelerometers, broadband seismometers) observations of surface motion: (1) precise definition of the coseismic phase; (2) the transition from coseismic to early postseismic motion; (3) rapid earthquake magnitude estimation for earthquake and local tsunami warning systems; and (4) interseismic deformation of the Dead Sea Fault.

Ground shaking and permanent displacements associated with an earthquake are considered the coseismic phase. Depending on the size and characteristics of the earthquake, ground shaking can last from seconds to minutes. For example, the 2004 M_w6.0 Parkfield earthquake that occurred on the right-lateral strike-slip San Andreas Fault, had a source duration of less than 60 seconds. On the other hand, the 2011 M_w9.1 Tohoku-oki earthquake that ruptured a

portion of the Japan subduction zone had a source duration of more than 3 minutes. In some cases, earthquake rupture is exceptionally slow with respect to its seismic moment (e.g., slow, tsunami earthquakes). For example, the medium sized 2006 M_w7.7 Java, Indonesia tsunamigenic earthquake ruptured for more than 4 minutes (Ammon et al., 2006).

Many aspects of the coseismic phase are still areas of active research; detection of initial seismic waves and association with a specific event in time and space (Zhang et al., 2019), determination of earthquake source parameters such as its size (Crowell et al., 2013), stress-drop (Lior et al., 2016), slip mechanism (Melgar et al., 2012), earthquake nucleation process (Rubin and Ampuero, 2005), self-similarity (Prieto et al., 2004), and more. Earthquakes tend to differ from one another, and yet, studying one can provide important information. Observations of many small earthquakes and their sense of slip can tell us about the long-term deformation on active faults (Hatzfeld et al., 1999). Looking at ground motions as a result of several earthquakes can teach us about expected motions for a range of earthquake sizes (Atkinson and Boore, 2006). On the other hand, lack of earthquakes on some fault segments can give an indication about tectonic plate coupling and strain accumulation.

Real-time systems for tsunami and earthquake early warning rely on high-rate data to warn populations of an occurring event (Allen and Kanamori, 2003; Given et al., 2014; Kohler et al., 2020; Hirshorn et al., 2021). Despite what many people think, earthquake early warning is not an earthquake forecast or precise prediction. Instead, once a significant earthquake is detected, the goal is to issue an informative warning to people to take action for their own safety, protect critical infrastructure, and be mentally prepared before shaking. However, the effective time of warning is short for those closest to the earthquake rupture and increases with distance away from it. Although shaking severity generally decreases away from the earthquake source, local effects such as soft sediments may amplify shaking (e.g., Mexico City that was built on top of ancient lake Texcoco). Earthquake data centers analyze streams of seismic and geodetic data, usually spanning diffuse plate boundaries, in an attempt to determine earthquake features in real-time. The most important metrics are earthquake location, depth, and size (magnitude).

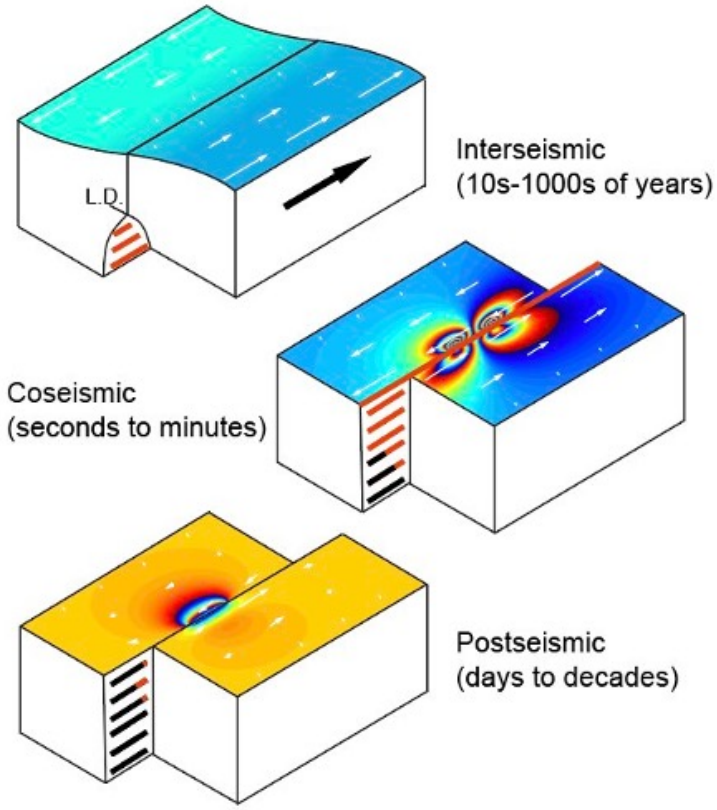

Figure 1.1. The three phases of the crustal deformation cycle illustrated by two blocks sliding past each other in a strike-slip fashion (credit: Bill Barnhart).

Based on these estimated parameters, the data center can then issue warnings to the public about expected shaking in different regions. Better methods for estimating earthquake location and magnitude in real-time, together with shaking prediction from an occurring event (Ground Motion Prediction Equations, or GMPEs) are essential for such warning systems to issue more accurate and informative warnings to populated areas (Cochran et al., 2018; Minson et al., 2019).

For tsunami warning systems, the goal is to warn and sometimes evacuate coastal populations before tsunami waves are expected to reach the shore. The first step is to characterize the earthquake with its location, size, and slip mechanism. Initial warning messages are issued based on predetermined depth and magnitude thresholds (see Chapter 3.1 for more information). These are extremely important for populations that are closer to the earthquake, with as little as a few minutes between earthquake origin time and first tsunami waves. In Chapter 3 we show that the combination of GNSS and strong-motion data ("seismogeodesy") is an important contributor to effective local tsunami warnings. Since tsunami waves travel with relatively slow velocity ($\sim$800 km/hr) compared to seismic waves, basin wide tsunami warnings are usually more informative based on teleseismic and wave heights measurements, including tide gauges and deep-ocean buoys (e.g., DART). In Chapter 1.2 and throughout the dissertation we will explain how we can benefit from different measurement types to study the coseismic phase of the crustal deformation cycle, and how we can better characterize earthquakes using their combination.

The postseismic phase of the crustal deformation cycle, starts immediately after an earthquake. It is considered as the transition period between the earthquake itself and when the fault returns to its long term, mostly steady loading rate. The postseismic phase can last for days to years (e.g., Ergintav et al., 2009) depending on the earthquake size and slip, the region's geological and rheological properties, and stress conditions along the fault. Although aftershocks can be considered part of the postseismic phase, they only account for a small percentage ($\leq$5%) of additional energy release (Zakharova et al., 2013) so that postseismic deformation is essentially aseismic (e.g., Beavan et al., 2012). The percentage of the accumulated postseismic moment

can be significant and even greater than the coseismic moment (Langbein et al., 2006). For example, after the 2004 M_w6.0 Parkfield, California earthquake (Bruhat et al., 2011; Johanson et al., 2006), the accumulated aseismic moment translated into another M_w6.0 event over five years, while the 2016 M_w6.0 Napa earthquake at a similar depth only generated a postseismic moment corresponding to an M_w5.6 event over the following four years (Klein et al., 2019).

This postseismic deformation is considered to be due to different or a combination of processes, including viscoelastic relaxation of the upper mantle (e.g., Wang et al., 2012b), afterslip on the fault plane (e.g., Freed, 2007; Ross et al., 2017) including frictional afterslip (e.g., Marone et al., 1991), and poroelastic rebound (e.g., Jónsson et al., 2003; Fialko, 2004b). Many postseismic studies assume that afterslip is the dominant process in a purely elastic fashion. Afterslip tends to decay with time, occur on the fault plane and can take place above or below the coseismic slip region. Viscoelastic relaxation is the response of viscous upper mantle to stress changes associated with the earthquake. Its relaxation time is usually longer and proportional to mantle viscosity (Barbot and Fialko, 2010). Viscoelastic relaxation has a longer wavelength signal on the surface, that is related to the depth of the viscous material. Poroelastic rebound is caused by pore fluid flow from stress changes in the crust due to the coseismic deformation. Both theory and observations suggest that poroelastic effects are mostly notable in the early stages of postseismic deformation (days to months) and in the near field of the earthquake (Peltzer et al., 1998; Fialko, 2004a; Peña et al., 2022).

The relationship between strain release during an earthquake and the spatio-temporal behavior of postseismic deformation is still a topic of interest. Identifying the transition from coseismic to postseismic deformation has important implications for understanding tectonic fault zone processes. Moment magnitude estimates that rely on time intervals beyond earthquake shaking may overestimate the actual strain release during the coseismic phase alone. It impacts our understanding of friction and its evolution in time and space (Barbot et al., 2009), the layered structure of the crust and upper mantle and its rheology (e.g., Hetland and Hager, 2006; DeVries and Meade, 2013) and the relationship between aseismic slip and the intensity and distribution

of possibly large aftershocks (Gualandi et al., 2020). Improving knowledge of these and other physical processes is essential for assessing and mitigating the effects of seismic hazard. Since the general trend of postseismic deformation is to decay exponentially or logarithmically with time after an earthquake (e.g., Shen et al., 1994), we can expect a large percentage of strain release to occur in the very early stages (Langbein et al., 2006; Ragon et al., 2019). In this dissertation we will show how we can identify the transition from coseismic to early postseismic phase using the tools described in the next section (Chapter 1.2). We will explore the importance of the early postseismic phase and how it can affect earthquake characterization and modeling.

The long-term fault slip rate between earthquakes is called the interseismic phase. During the interseismic phase of the crustal deformation cycle, stress is accumulated along the fault (Jiang and Lapusta, 2017; Jolivet et al., 2020). An earthquake occurs when the accumulated strain is suddenly released by rupture in the form of coseismic slip along the fault interface, releasing energy and generating seismic waves. Long term velocity between tectonic plates ranges from 5 mm/yr continental boundaries (e.g., Sinai versus Arabia plates) to 150 mm/yr in the East Pacific Rise spreading center (Pacific versus North America plates) (DeMets et al., 2010). This is the basic long-term process driven by global tectonic plates motion. Depending on the relative velocity between the tectonic plates and fault stress conditions, this period can last from years to decades to centuries. For areas within plates, the interseismic period (between intraplate earthquakes) tends to be longer (Williams et al., 2017; Magnani et al., 2017). One might think that earthquakes generated by constant stress loading and unloading occur at regular intervals in time or space (Im et al., 2017; Salditch et al., 2020). However, details are considerably more complex than this simple idea. Loading rates and crustal strength are not uniform in time and space, making stress conditions vary. An earthquake that occurs on an adjacent fault may change the static stress on other segments, and farther earthquakes can cause dynamic triggering (Fan and Shearer, 2016; Fan et al., 2021; Fan et al., 2022). Fluid migration can also weaken the upper crust and affect earthquake repeating times and fault slip (Bhattacharya and Viesca, 2019). Currently, these complications and the lack of short-term precursors have put accurate earthquake

predictions beyond our reach. Instead, we can study and model temporal and spatial variations of the long-term crustal deformation in confined regions. Together with geological or historical evidence, we can then assess the current stress conditions along the fault.

Although the majority ($\sim$80%) of continental plate motion is accommodated on locked faults (Bird and Kagan, 2004), slip can be accommodated on shallow creeping segments (Harris, 2017) or slow earthquakes (Beroza and Ide, 2011). Locked faults accommodate minimum to no slip at the plate boundary, but relative velocity increases elastically with distance. Creeping sections experience the opposite trend of maximum velocity differences at the fault interface that dissipate away from it. Shallow creeping sections have been observed along several segments of the San Andreas Fault in California (Lyons and Sandwell, 2003; Shirzaei and Bürgmann, 2013; Lindsey et al., 2014a), the North Anatolian Fault in Turkey (Kaneko et al., 2013), Sumatran Fault in Indonesia (Tong et al., 2018), and the Dead Sea Fault in Israel (Hamiel et al., 2016). Long-term interseismic deformation can tell us about the locking depth of the fault, its spatially varying slip rates, and crustal properties by studying creeping versus locked fault behaviors. Studying the interseismic phase of the crustal deformation cycle is also important for understanding slip partitioning and strain accumulation and redistribution along tectonic faults (Stein, 1999; Marsan, 2005) and distinguish transient motions. Together with earthquake history, these observations can then be translated into strain rates and seismic hazard maps in populated regions. In this dissertation we show how combination of geodetic methods can improve observations of long-term crustal deformation by investigating different sections along the Dead Sea Fault.

1.2 Seismology, Geodesy, and Their Combination (Seismo-geodesy)

The crustal deformation cycle includes fault slip at time scales ranging from seconds to years. Therefore, some metrics are more suitable than others for a specific type of deformation. Seismic instruments such as broadband seismometers and strong-motion accelerometers are extremely useful in measuring the dynamic component of earthquake shaking. Traditional earthquake early warning systems are based on real-time seismic data. These instruments are sensitive enough to capture the first arriving body waves and the following surface waves. P wave arrivals, at times together with S wave arrivals, are used for earthquake detection, location and early warning. However, within close distance to large earthquakes, high gain broadband seismometers tend to "clip", meaning that measuring the intensive shaking is well beyond the instrument's dynamic range. Strong-motion accelerometers are built with lower gain and therefore do not experience waveform "clipping" during large amplitude shaking. However, integrating accelerations from strong-motion instruments to estimate velocity or displacement introduces integration ("baseline") errors (Boore et al., 2002). Waveform recovery requires filtering which results in the loss of long period information. Empirical relationships between ground motion intensity and earthquake magnitude (Ground Motion Prediction Equations, or GMPEs) are constantly being developed and improved using new measurements of earthquake Peak Ground Velocity (PGV) and Peak Ground Acceleration (PGA). Although greatly used, GMPEs are in some ways limited. Application of one model across regions often yields unreliable results, and modeling local site and path effects can be challenging. Additionally, estimating the size of an earthquake based on seismic data alone can often result in magnitude saturation (underestimation). For example, during the 2011 M_w9.1 Tohoku-oki earthquake, strict reliance on seismic records by the Japan Meteorological Agency (JMA) led to a magnitude estimate of M_w7.3 when issuing the first warning to the public and M_w8.2 a few minutes later (Hoshiba and Ozaki, 2014). For comparison, a magnitude M_w9.0 is ten times bigger than a magnitude

M_w8.0 earthquake, and ∼32 times stronger in terms of energy release. Additional magnitude determination methods using seismic instruments include P wave-based metrics (i.e., M_{wp}) and W-phase inversion (see Chapter 3.1 for more details). Other than P wave picking, earthquake association and location, and magnitude estimation, seismic instruments can be used for other applications. These include detection of microseismicity (Nadeau et al., 2004), utilizing repeating earthquakes as subsurface creepmeters (Turner et al., 2013), and calculation of earthquake focal mechanism using first-motion polarity and S/P amplitude ratios (Hardebeck and Shearer, 2002; Hardebeck and Shearer, 2003). Since long term and postseismic deformation is mostly aseismic, other measuring techniques are often used instead of, or together with, seismic instrumentation.

Continuous Global Navigation Satellite Systems (GNSS) networks provide long-term daily displacement time series with millimeter-level precision that record the surface expression of the different phases of the crustal deformation cycle, including transients (Figure 1.1). Generally, separate fault slip inversions are carried out for coseismic, postseismic, interseismic and transient slip along with other geodetic data (GNSS, InSAR), seismic data and geologic slip rates (e.g., Bürgmann et al., 2013; Bock and Melgar, 2016; Zeng and Shen, 2017). Historically, the basic GNSS "observables" used in coseismic fault slip inversions have been offsets between pre- and post-earthquake positions estimated from daily displacement time series. Frequently, offsets are calculated by differencing several days of displacements prior to and after an earthquake (e.g., Lorito et al., 2011; Ding et al., 2015), which may include a significant amount of postseismic motion. GNSS instruments also measure dynamic displacements, albeit at lower precision compared to seismic instruments, as well as the static component (Nikolaidis et al., 2001; Larson, 2009; Langbein and Bock, 2004; Genrich and Bock, 2006; Larson, 2009). It has been shown that scaling relationships that are based on GNSS ground motions do not suffer from magnitude saturation (Crowell et al., 2013; Melgar et al., 2015a). Indeed, several earthquake early warning systems incorporate real-time GNSS positioning in their earthquake characterization analysis. The combination of GNSS with strong-motion data (Bock et al., 2011), also known as "seismogeodesy", yields both broadband velocity and displacement waveforms that do not

clip and are sensitive to the entire spectrum of ground motions from the Nyquist frequency of the accelerometer to the static offset of the GNSS displacement. Seismogeodetic waveforms have reduced noise levels and are therefore suitable for earthquake early warning systems (Geng et al., 2013; Goldberg and Bock, 2017). The advantages of seismogeodesy were demonstrated in rapid response to the 2011 M_w9.1 Tohoku-oki (Melgar et al., 2013b) and 2014 M_w6.0 Napa (Melgar et al., 2015b) earthquakes, and through a combination of GNSS with even low cost Micro-Electro Mechanical System (MEMS) accelerometers (Saunders et al., 2016).

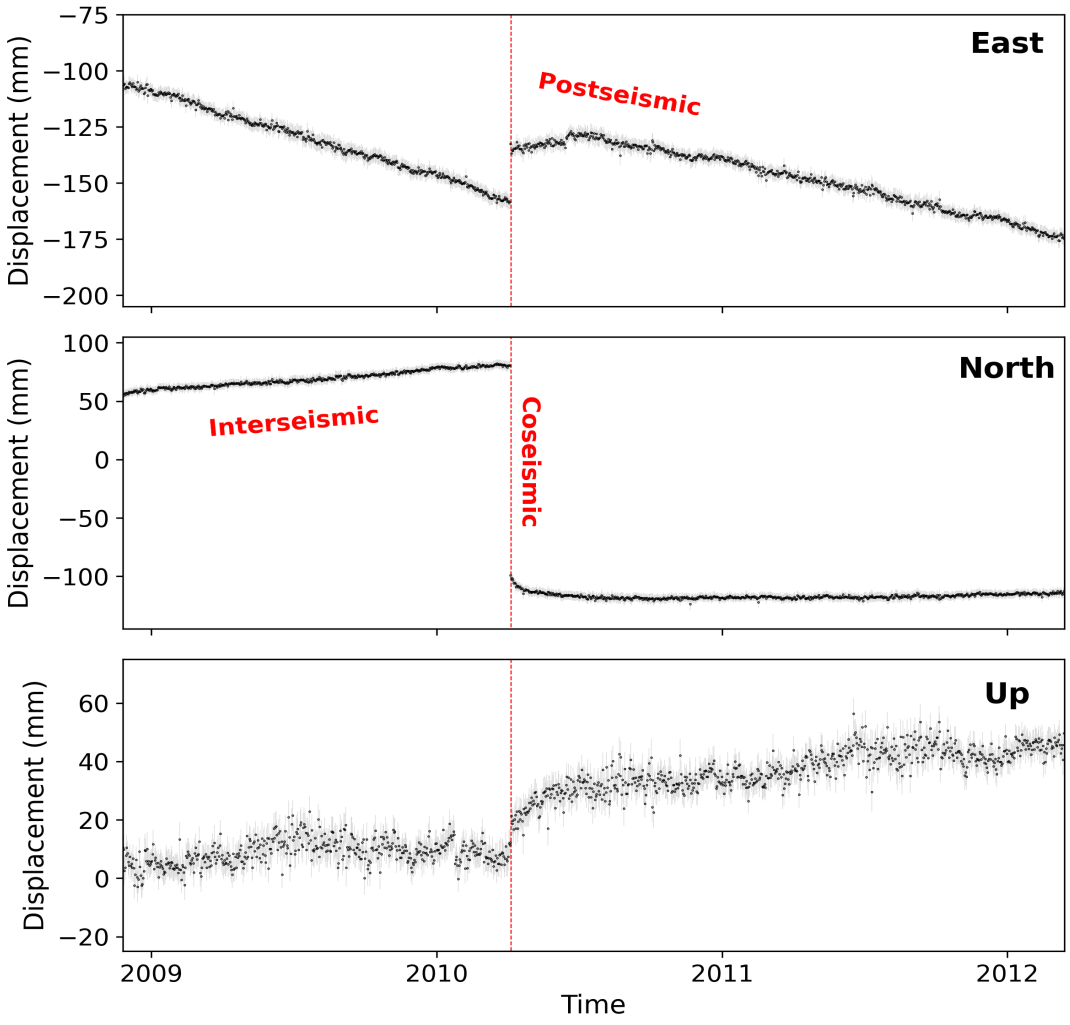

Figure 1.2. Example of daily GNSS displacement time series (station P494, southern California) exhibiting all phases of the crustal deformation cycle. The 2010 M7.2 El Mayor-Cucapah earthquake is denoted by red vertical line.

Synthetic Aperture Radar (SAR) imagery is produced when a target on the ground is illuminated with electromagnetic waves and reflects back the informative signal. Two SAR images of the same area, acquired at different times, can indicate ground shift towards or away from the orbiting radar platform. This geodetic technique uses the phase difference between the two images, producing an interferogram. Interferometric Synthetic Aperture Radar (InSAR) is an effective way of making high-density surface displacement measurements. The number of studies utilizing InSAR has grown dramatically in the past decade mostly due to a growing number of satellites, spatial coverage, data quality, and open-source processing software (e.g., GMTSAR by Sandwell et al., 2011). Similar to GNSS, InSAR is capable of measuring all phases of the crustal deformation cycle. It has been used for earthquake coseismic slip (Sandwell et al., 2000; Fialko et al., 2005; Tong et al., 2010; Lindsey et al., 2015), postseismic modeling (Jacobs et al., 2002; Barbot et al., 2009), and long term interseismic deformation (Lindsey et al., 2014b; Weiss et al., 2020; Xu et al., 2021; Ou et al., 2022). Other SAR applications include disaster mapping such as landslides (Sun et al., 2015; Rosi et al., 2018), sinkholes (Baer et al., 2018; Nof et al., 2019), fires (Liu et al., 2014), monitoring fault creep (Wei et al., 2009; Kaneko et al., 2013), volcanic deformation (Myer et al., 2008; Lau et al., 2018), and hydrological effects (Xu et al., 2017). Klein et al. (2019) showed that by correcting InSAR Line-Of-Sight (LOS) displacements with GNSS positioning, one can significantly reduce errors due to ionosphere, troposphere, tides, and improve phase unwrapping. In addition, GNSS positions provide 3D displacements with respect to a global reference frame that can be used to tie interferograms to the same reference frame (Xu et al., 2021). Compared to daily or high-rate GNSS, InSAR has a much lower temporal sampling rate (6-12 days repeat times for Sentinel-1, for example). However, GNSS station coverage is usually sparse (20-30km average in California) compared to InSAR spatial coverage with a resolution of tens of meters or even higher for commercial satellites. By combining both geodetic data types we can benefit from the higher sampling rate of GNSS and better spatial coverage of InSAR in tectonically active regions.

1.3 Interrelationships Between Chapters and Research Questions

In this dissertation, we use seismic and space geodetic techniques to study the different phases of the crustal deformation cycle, including the transition from one to the other. In Chapter 1, we present background and show the importance of studying the different phases of the crustal deformation cycle. We introduce the data types used in these studies and their combination, and layout the research questions and relationships between the chapters. In Chapter 2, we distinguish between the coseismic phase of an earthquake and its very early postseismic phase, using both collocated and interleaved seismic and GNSS stations. The research questions are: how significant is early postseismic deformation in the first hours following the earthquake? Are these different within magnitudes and slip mechanisms? How does under-sampling translate into fault slip models? We explore several earthquake examples of different magnitudes and slip mechanisms and show that the early stages of the postseismic deformation are crucial for physically-meaningful static slip inversions. Therefore, traditional methods of daily GNSS positioning can bias magnitude and slip models if not accounting for this early postseismic phase of an earthquake. Chapter 3 focuses on a new methodology for earthquake magnitude estimation using seismogeodesy, in particular for local tsunami warnings to populations that close to the earthquake rupture. The research questions are: Can we estimate the magnitude of medium to great earthquakes based on far-field theoretical equations? How fast and accurate are these estimates compared to other GNSS-based methods? Are these estimates useful for tsunami and earthquake early warning systems? In Chapter 4 we examine the long term interseismic deformation along the Dead Sea Fault using a combination of GNSS positioning and satellite imagery. The research questions are: can we detect interseismic deformation using InSAR Line-Of-Sight displacements in tectonic regions with relatively small slip rates? What is the improvement after combining GNSS with InSAR? How do different Dead Sea Fault segments behave (locked versus shallow creep)? What is the strain distribution along the fault segments?

In Chapter 5 we present a summary of these studies and ideas for future research. Throughout the dissertation, we focus on all three phases of the crustal deformation cycle, with a combination of seismic, GNSS, and InSAR measurements. While seismic instruments provide the most accurate measurement of the dynamic coseismic motion, GNSS and InSAR are favorable for mostly aseismic postseismic, long term interseismic crustal deformation and transients. We investigate each of the phases in the context of improving current methods for tsunami and earthquake early warnings by extracting earthquake source parameters in a more accurate fashion, and looking at long term velocity for strain rate analysis and seismic hazard assessment in actively tectonic regions.

Chapter 2

Transition from Coseismic to Early Postseismic Deformation Revealed by Seismogeodesy

2.1 Background

With the advent of high-rate GNSS tracking ($\leq$1s) compared to 15-30s sampling used for daily positioning of large-scale plate boundary networks, station positions can be estimated at the receivers' sampling rates with about centimeter-level precision in the horizontal components and several centimeters in the vertical component (Genrich and Bock, 2006). Therefore, the transition from coseismic to postseismic deformation can be determined with increased temporal resolution (Langbein et al., 2006). Recent studies have also utilized P wave picks from regional seismic stations to determine the onset of the coseismic phase at GNSS stations (Goldberg et al., 2018; Melgar and Hayes, 2019). Melgar et al. (2013b) used high-rate GNSS to define the coseismic time window from the start of anomalous displacements to when they drop in magnitude to a certain percentage of peak variance. In a similar fashion, Liu et al. (2014) identified the earthquake's dynamic motion using variance change in GNSS displacement time series. Twardzik et al. (2019) investigated the appropriate window of data to define the onset of postseismic motion by applying statistical detection tests of the GNSS precision. In this chapter we present a new physics-based methodology to define and identify the coseismic phase and its

transition to early postseismic deformation applicable to interleaved seismic and GNSS regional networks. We apply a seismogeodetic approach that utilizes seismic velocities integrated from strong-motion accelerations to bracket the time window, either through collocation of geodetic and seismic instruments or by the interpolation of the coseismic time window to the GNSS network. Once the coseismic window is defined, we quantify the effect of lumping coseismic and postseismic motions as a function of the amount and duration of data used to estimate coseismic slip and seismic moment.

2.2 Identifying the Coseismic Time Window with Seismic Data

High-rate GNSS displacement waveforms can be used to estimate coseismic offsets but are not precise enough to capture the arrival of P waves. Therefore, a seismic trigger is required to determine the onset of the coseismic phase. Ideally, this can be obtained by collocation (within $\sim$3–4km) of strong motion accelerometers and GNSS instruments (Emore et al., 2007; Goldberg and Bock, 2017). A seismogeodetic combination of GNSS and accelerometer data (Bock et al., 2011) allows P wave detection from seismic velocities, while improving the precision of the displacement waveforms during seismic motion (Bock et al., 2004; Saunders et al., 2016). Although the collocation of seismic and GNSS stations is advantageous, our methodology to identify the transition from coseismic to postseismic deformation does not require it. Rather, we adopt a looser seismogeodetic approach that uses acceleration or velocity waveforms observed by nearby seismic stations to tag both the start and end times of coseismic motion. The coseismic time window is then transferred to the GNSS stations by linear barycentric interpolation and the static coseismic offsets are estimated from the high-rate GNSS displacements.

Table 2.1. Earthquakes used in this study.

Name / Region	M_w[1]	Fault Mechanism	Origin Time (UTC)[2]	Longitude (° E)	Latitude (° N)	Depth (km)
Parkfield, California	6.0	Strike-slip	2004-09-28 17:15:24	-120.366	35.818	8.1
El Mayor, Mexico	7.2	Strike-slip	2010-04-04 22:40:42	-115.295	32.286	10.0
Miyagi, Japan	7.3	Reverse	2011-03-09 02:45:12	143.280	38.329	8.3
Tohoku-oki, Japan	9.1	Reverse	2011-03-11 05:46:24	142.861	38.104	29.0
Fukushima, Japan	6.6	Normal	2011-04-11 08:16:12	140.673	36.946	6.4
Napa, California	6.0	Strike-slip	2014-08-24 10:20:44	-122.312	38.215	11.1
Kumamoto, Japan	7.0	Strike-slip	2016-04-15 16:25:05	130.763	32.755	12.5
Ridgecrest, California	6.4	Strike-slip	2019-07-04 17:33:49	-117.506	35.705	10.7
Ridgecrest, California	7.1	Strike-slip	2019-07-06 03:19:53	-117.599	35.770	8.0
Simeonof, Alaska	7.8	Reverse	2020-07-22 06:12:44	-158.522	55.030	28.0

[1] Magnitudes are from the United States Geological Survey (USGS) catalog

[2] Earthquake origin time and hypocenter location are from the NIED and USGS for Japan and Western US earthquakes, respectively

We demonstrate our approach by applying it to a series of earthquakes over a range of magnitudes and focal mechanisms in California, Mexico, Alaska, and Japan (Table 2.1). Strong-motion accelerograms and broadband seismograms (for P wave picks only) were obtained from the IRIS archive for California and Alaska, and K-net and KiK-net data from Japan's National Research Institute for Earth Science and Disaster Resilience (NIED) archive (Okada et al., 2004). We collected high-rate (1Hz) GNSS data from continuous networks in California and Alaska (Murray et al., 2019) and from Japan's GEONET (Sagiya et al., 2000; Sagiya, 2004). GNSS displacements were estimated using the method of precise point positioning (PPP) (e.g., Ge et al., 2008; Geng et al., 2012), without ambiguity resolution, with the exception of the 2004 M_w6.0 Parkfield earthquake that was processed using relative positioning (Langbein and Bock, 2004). With the PPP approach, no regional reference station is required and "absolute" positions are generated with respect to a global reference frame (Zumberge et al., 1997).

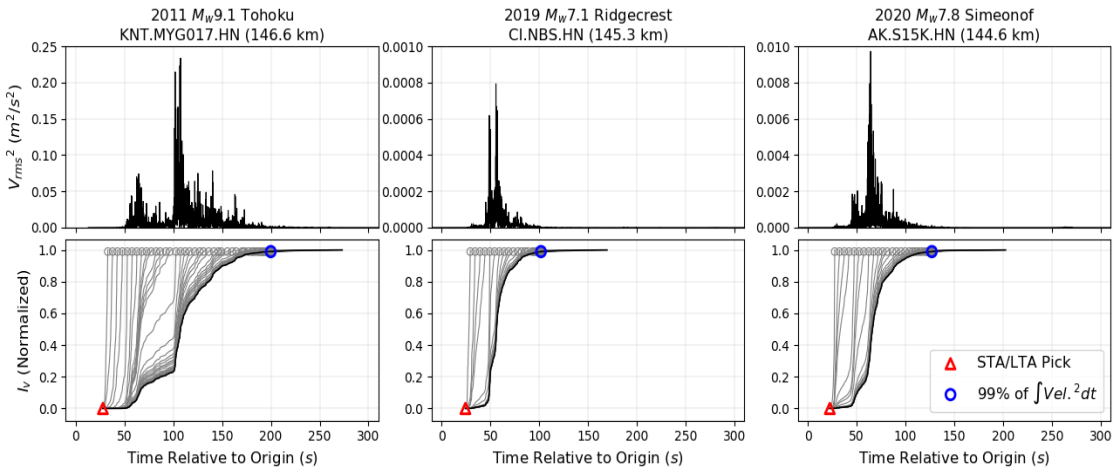

Figure 2.1. Bracketing the timing of coseismic motions at seismic stations. Three-component velocity squared (top panels) and normalized I_v (equation 2.1, bottom panels) recorded from the 2011 M_w9.1 Tohoku-oki (left), 2019 M_w7.1 Ridgecrest (middle), and 2020 M_w7.8 Simeonof (right) earthquakes. The corresponding times of STA/LTA picks and 99% of the normalized I_v are shown by the red triangles and blue circles, respectively. Grey curves show the normalized integration at each 5-seconds step, together with its 99% point by a grey circle. Black curve shows the final normalized integration after convergence, together with its 99% point by a blue circle.

We define the start of the coseismic time window T_P as the first P wave arrival using a short-time-average through long-time-average trigger (STA/LTA) algorithm (Allen, 1982) for the continuously recorded California and Alaska seismic data. Since Japan's strong-motion data are triggered, we use the recorded start time for those waveforms. To define the end of the coseismic phase T_{End}, we introduce the following measure:

$$I_v = \int_{T_P}^{T_{End}} v^2 dt \tag{2.1}$$

where v is the three-component velocity. We apply a 1Hz Butterworth highpass filter for each velocity component to minimize long period noise introduced by the integration. By calculating I_v we are summing power-per-sample across time, which is a measure of total energy of the signal with units of J/Kg integrated over time. From Parseval's theorem, this is equivalent to summing the spectral power across frequency. We calculate the normalized I_v and its 99% point iteratively from the P wave arrival time T_P to T_{End} within a 5s moving window. The final 99% point is set when it converges and does not increase by more than 1s for at least 10 iterations.

Figure 2.1 shows a few examples, where we mark the coseismic end time when 99% of the total energy has been recorded at a station. By doing so, we estimate the progression of the rupture process through the network of sensors. The near-field stations experience severe shaking, while more distant stations are not yet affected by the earthquake. By the time that far-field stations are at peak displacement, an early postseismic motion might already be observed at the near-fault stations. Furthermore, the duration of the coseismic window tends to increase with hypocentral distance.

We compare our energy measure with one based on accelerations, which does not require integration to velocity. Similar to Equation 2.1, we define

$$I_a = \int_{T_P}^{T_{End}} a^2 dt \tag{2.2}$$

where a is the three-component acceleration. For consistency, we apply here the same highpass

filter used for the velocity records. Figure 2.2 shows both measures for the 2019 M_w7.1 Ridgecrest earthquake. We find that the 99% times are more clustered over the range of hypocentral distances for I_v compared to I_a, implying that I_v is somewhat better suited to our application. We speculate that acceleration, and hence I_a, is more affected by coda waves. Therefore, we bracket the time span of the coseismic phase from the STA/LTA velocity picks determined at all seismic stations until 99% of energy release determined by I_v. In determining the onset time at as many seismic stations as possible, we can also include broadband seismometer (velocity) data that often produce only truncated waveforms in the vicinity of a large event. In order to exclude false P wave picks (e.g., S wave and surface waves), we merge two velocity models: CRUST1.0 (Laske et al., 2013) with higher temporal resolution for the shallower part, and IASP91 (Kennet, 1991) for the deeper part of the crust. For each earthquake region, we exclude stations with picks that are outside of a $\pm$33% cone of the averaged P wave velocity over the layers above the hypocenter (red dashed lines in Figure 2.2).

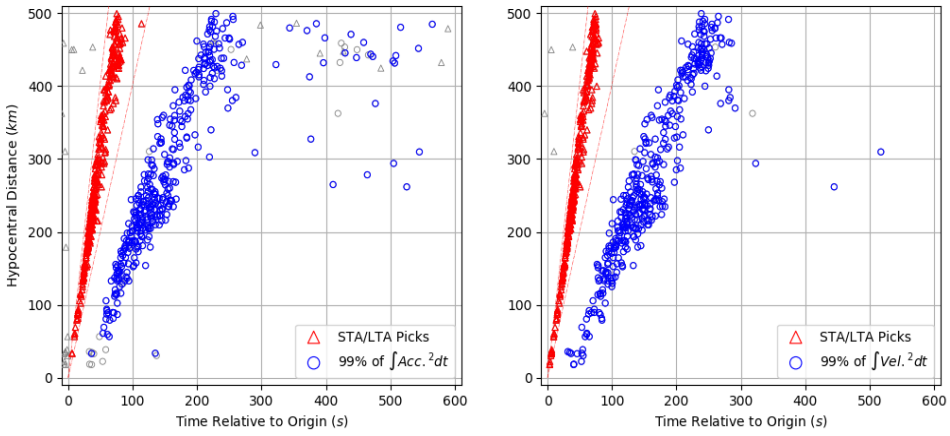

Figure 2.2. Comparison of the coseismic time windows when calculated from acceleration and velocity waveforms. STA/LTA picks (red) and 99% (blue) thresholds for I_a (left, equation 2.2) and I_v (right, Equation 2.1) for all seismic stations within 500km of the 2019 M_w7.1 Ridgecrest earthquake. Seismic picks that are outside of the $\pm$33% of the regional P wave velocity (red dashed lines) are excluded and denoted in grey color, together with their corresponding 99% points. The 99% threshold at I_v is more clustered and pronounced than I_a, and therefore we choose that as our preferred way to estimate the end time of the coseismic window.

2.3 Estimating Coseismic Offsets with High-Rate GNSS Data

Current practice is to assume a single coseismic window for a particular earthquake, chosen according to the resolution of the GNSS displacement data. However, when using the seismic data to bracket the coseismic phase coupled with the availability of high-rate GNSS displacements, this assumption is no longer valid. Of course, for greater hypocentral distances, the first P wave arrive later in time and, thus, the start time of the coseismic window is delayed (Figures 2.3 and 2.4). Furthermore, the duration of the coseismic period is longer at farther distances for several possible reasons. The separation of the different seismic phases, such as surface waves, becomes more pronounced. There are local effects that contribute to extended periods of ground shaking caused by amplifications and more reflections (e.g., soft basin sediments). Additionally, large events over greater areas have a specific rupture direction resulting in a displacement pulse shape that depends on the observer's azimuth relative to the fault and its geometry. Hence, the width of the coseismic time window is expected to vary from station to station.

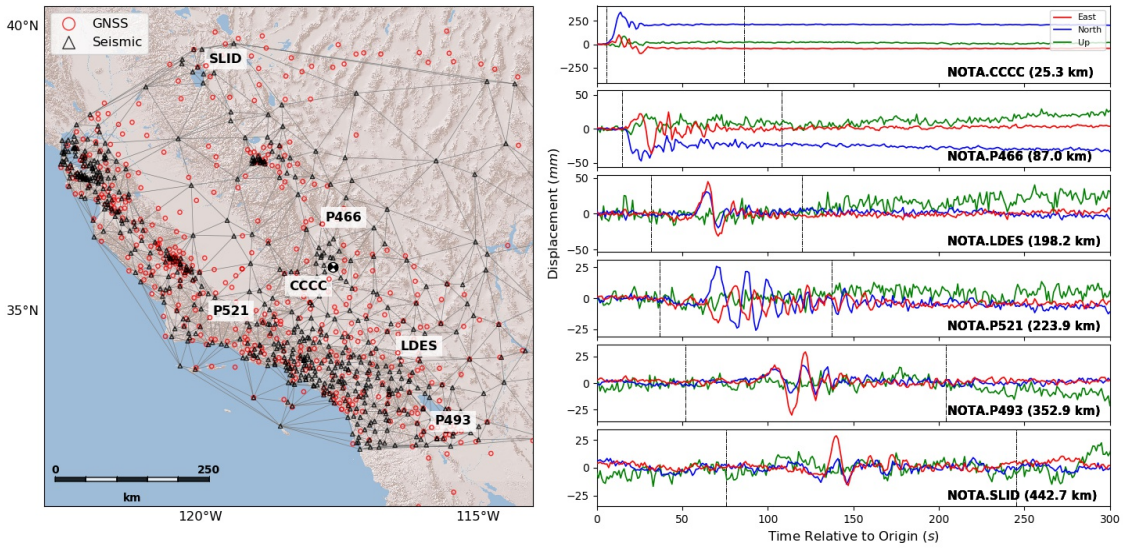

Figure 2.3. Displacement time series from the 2019 M_w7.1 Ridgecrest earthquake at six Network of the Americas (NOTA) GNSS stations at hypocentral distances from ∼25 to ∼443km. Vertical dashed lines denote the start and end times of the coseismic phase, interpolated from the locations of the surrounding seismic stations. The left panel shows a map of the study area with the seismic stations triangulated and GNSS stations (red dots).

After estimating the coseismic start and end times from the seismic velocities, we transfer the time window to the regional GNSS stations by triangulating the seismic station time tags and performing a linear barycentric interpolation (Figures 2.3 and 2.4). GNSS stations that are outside any triangle are treated by a simple second-degree polynomial interpolation of the 99% scatter points (Figure 2.2, right panel) for the entire region of interest. We find that only a small fraction of stations requires this type of interpolation, mostly at greater hypocentral distances.

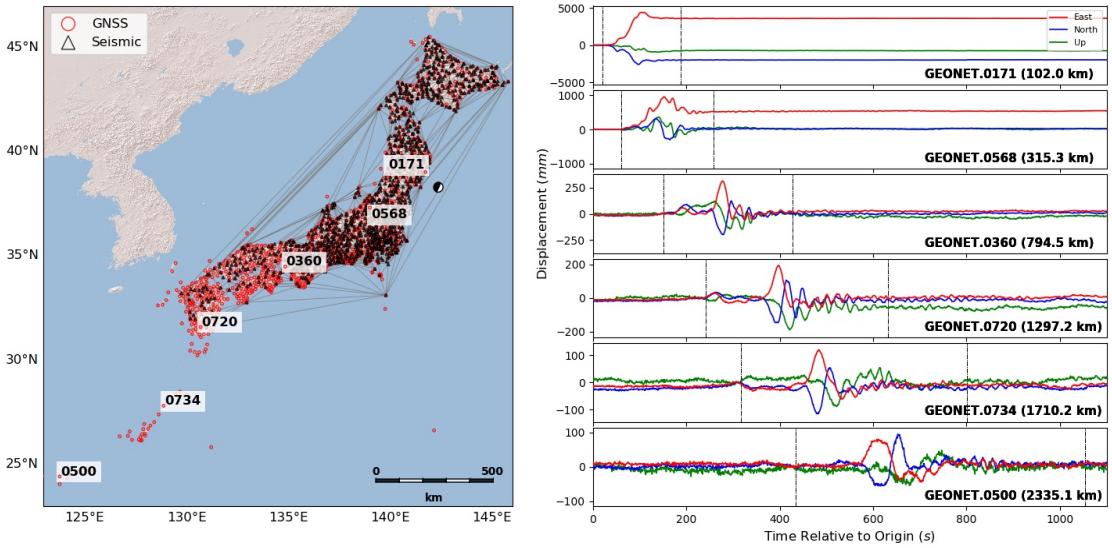

Figure 2.4. Displacement time series from the 2011 M_w9.1 Tohoku-oki earthquake at six GEONET stations at hypocentral distances from ∼102 to ∼2335km. Vertical dashed lines denote the start and end times of the coseismic window, interpolated from the surrounding seismic stations. The left panel shows a map of the study area with the seismic stations triangulated and GNSS stations.

The seismic data are more sensitive to dynamic motion than the GNSS data. Therefore, at longer epicentral distances the P wave may be resolvable while the static offset is negligible. In order to choose stations that have significant static offsets, we use two criteria. Our first criterion is based on the magnitude of the horizontal static displacements, computed as

$$d_{horizontal} = \sqrt{{d_{East}}^2 + {d_{North}}^2} \tag{2.3}$$

where d_{East} and d_{North} are east and north components. Our second criterion is based on the signal-to-noise ratio (SNR) for the horizontal components,

$$
\begin{aligned}
SNR &= \frac{d_{rms}^{signal}}{d_{rms}^{noise}} \\
d_{rms} &= \sqrt{\frac{1}{n}\sum_{i=1}^{n} {d_i}^2}
\end{aligned}
\tag{2.4}
$$

where d_{rms}^{signal} is the root-mean-square (rms) of the total (static and dynamic) horizontal displacements within the coseismic time window, d_{rms}^{noise} is the rms of displacements 10s prior to the onset of coseismic motion and n is the number of samples in the waveform.

The static coseismic offsets for each station are computed by differencing the 1Hz positions at the end of the coseismic window from those at the start. We use a 10s average to minimize the effects of dynamic motion (Melgar et al., 2012; Crowell et al., 2016 - although these studies used other criteria for defining the coseismic window). The displacement noise before and after the coseismic time window is dominated by multipath which has a significantly longer period than the size of the window (Genrich and Bock, 2006), while the noise is reduced within the window itself (Bock et al., 2004). Since we are interested in short-term variations in displacement at both ends of the window, rather than the positions themselves, it is preferable to minimize the chosen size of the data window in calculating the coseismic offset. The assumption is that the displacements are less correlated over the short window compared to a longer window where multipath begins to dominate.

Our first criterion for choosing stations with significant horizontal coseismic offsets for further analysis is a total horizontal offset of $\geq$5mm (Equation 2.3). Our second criterion is a SNR of $\geq$3 (Equation 2.4). The right panels in Figures 2.3 and 2.4 for the 2019 M_w7.1 Ridgecrest and 2011 M_w9.1 Tohoku-oki earthquakes, respectively, show as examples six displacement time series. The horizontal uncertainties of high-rate GNSS displacements are well established from PPP kinematic analyses of long time series by multiple analysis centers to be at about 1–2cm, with a root-mean-square of about 1.3cm (e.g., Kouba et al., 2017). However, our experience

with multiple earthquakes observed with high-rate data indicates that an uncertainty of 5mm is a reasonable cutoff and it allows us to better sample far-field displacements that improve the resolution of fault slip models at depth. We demonstrate this later when inverting for a slip model of the 2019 M_w7.1 Ridgecrest, 2016 M_w7.1 Kumamoto, 2011 M_w6.6 Fukushima and 2011 M_w9.1 Tohoku-oki earthquakes. Once a station is identified to have a significant coseismic offset, we calculate the precision of a single 1Hz displacement by computing the variance of the 10s window of displacements prior to the start of the coseismic window. We assign the offset uncertainty (one sigma) by doubling the variance and taking its square root. We only use data before the start of the coseismic window since its end is determined from the seismic velocities (Equation 2.1) and may still contain additional dynamic motion.

2.4 Comparison of Static Offsets with Traditional Daily GNSS Positioning

We compare static coseismic offsets estimated by our seismogeodetic method (hereafter called "rapid") with those based on daily displacement time series (hereafter called "daily") for earthquakes with a range of magnitudes and slip mechanisms (see Table 2.1 for the list of earthquakes). The differences in magnitude (horizontal or vertical) between the daily and rapid offset are referred to as "differences." We use daily displacement time series for stations in California and Alaska published by the NASA MEaSUREs project (Bock and Melgar, 2016) and the Geospatial Information Authority of Japan (GSI) daily displacements for stations in Japan (Sagiya, 2004). Daily static offsets are estimated by differencing up to 10-day best-fit positions before (linear) and after (exponential) an earthquake, depending on the number of days without another significant event. For instance, we only use a 2-day average after the M_w9.1 Tohoku-oki earthquake, $\sim$55hr later. We estimate the uncertainties by doubling the variance and taking its square root in the same manner as the rapid offsets, with up to 10-day window prior to the day of the earthquake.

Averaging daily positions before and after an earthquake is typical for estimating coseismic offsets as input to fault slip inversions. Pollitz et al. (2011) estimated coseismic offsets for the 2010 M_w8.8 Maule, Chile event using a linear regression of up to 3 years of pre-earthquake daily positions and one week of daily post earthquake positions, without consideration of postseismic motion. In their study of coseismic deformation and afterslip from the 2015 M_w8.3 Illapel, Chile earthquake, Shrivastava et al. (2016) used daily displacement time series averaged over 30 days prior to and 43 days after the event - the time evolution of postseismic deformation was modeled (through principal component analysis), therefore effectively, their coseismic offsets have a temporal resolution of a day or more. Other studies used 4-day averages before and after the day of the event for the 2012 M_w7.8 Haida Gwaii, British Columbia earthquake (Nykolaishen et al., 2015) and at least 3 days for the 2013 M_w6.6 Lushan, China earthquake (Huang et al., 2019).

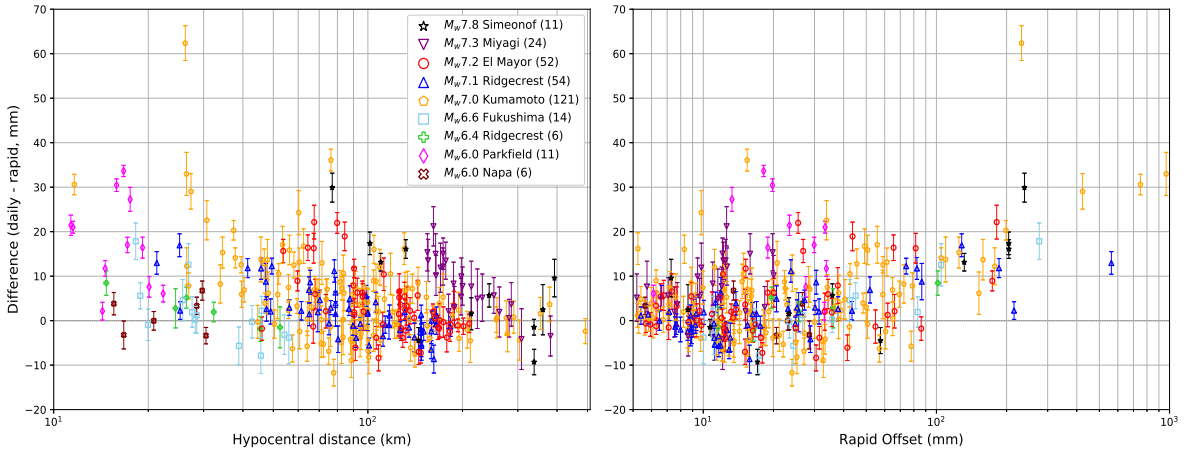

Figure 2.5. Semi-log comparison of the horizontal static offset differences between daily (24-hour) and rapid (1Hz) coseismic displacements for different earthquakes in California, Alaska, Mexico and Japan (Table 2.1). Left panel shows the differences with hypocentral distance, while the right panel shows the differences with the rapid offset. Error bars are $\pm 1\sigma$. The number of affected stations is denoted in parentheses after the earthquake names.

With the greater availability of high-rate (1–10Hz) GNSS displacements, several studies have used a shorter coseismic window (e.g., Langbein et al., 2006; Ragon et al., 2019; Twardzik et al., 2019).

The comparisons of the rapid and daily coseismic offsets are shown in Figure 2.5 for nine of the earthquakes (Table 2.1) as a function of hypocentral distance and the rapid offset. The great 2011 M_w9.1 Tohoku-oki, Japan earthquake is discussed later. In order to isolate the aseismic motions for each event, we exclude the effect of significant aftershocks that occurred on the same day (Table 2.2). To calculate the one-sigma error bars in Figure 2.5 (and Figure 2.6), we apply error propagation to the rapid and daily offsets uncertainties. Supposing that GNSS displacements for each component are normally distributed, we can assume that one-sigma error is equivalent to $\sim$68% confidence level. The differences are considered significant if their error bars are fully above (or below) the zero line. The uncertainties are on the order of 2–12mm for

Table 2.2. Aftershocks causing significant coseismic offsets that were estimated and subtracted from the 1Hz displacement time series of the day of the mainshock. Earthquake origin time and hypocenter location are from National Research Institute for Earth Science and Disaster Resilience (NIED). Magnitudes are from USGS catalog.

Name / Region	M_w	Fault *Mechanism*	Origin Time (UTC)	Affected *Mainshock*	Time after mainshock (hh:mm:ss)
Iwate, Japan	7.4	Thrust	2011-03-11 06:08:53	M_w9.1 Tohoku-oki	00:22:29
Ibaraki Japan	7.9	Thrust	2011-03-11 06:15:34	M_w9.1 Tohoku-oki	00:29:10
North Honshu, Japan	7.7	Normal	2011-03-11 06:25:44	M_w9.1 Tohoku-oki	00:39:20
South Niigata, Japan	6.2	Thrust	2011-03-11 18:59:15	M_w9.1 Tohoku-oki	13:12:52
Kumamoto, Japan	5.7	Normal	2016-04-15 16:45:55	M_w7.0 Kumamoto	00:20:50
Kumamoto, Japan	5.4	Strike-slip	2016-04-15 18:03:10	M_w7.0 Kumamoto	01:38:05

all earthquakes. The significant differences between the daily and rapid offsets are positive for the most part with the exception of a few negative differences.

In order to validate the magnitudes and uncertainties of our daily offsets, we compared them with those estimated by the NASA MEaSUREs project for the California, Mexico, and Alaska earthquakes (Figure 2.6). The project performs a parametric daily displacement time series analysis based on its entire data holdings, estimating coseismic offsets and postseismic parameters for a series of earthquakes over a nearly 30-year period. Our daily coseismic offsets are mostly smaller (up to $\sim$17mm), especially for the horizontal components. This is consistent with our premise that fitting schemes that rely on longer data spans can bias coseismic offset estimates. The MEaSUREs analysis relies on much longer time series than our 10 days and makes the common assumption that a single decay term with either a single exponential or logarithmic function, which may be insufficient to characterize the complexities and evolution of postseismic deformation (Jiang et al., 2021). Furthermore, the overestimate of the MEaSUREs analysis implies that the common assumption of a single postseismic decay term per station is insufficient. However, as expected, the bottom panels of Figure 2.6 shows that our uncertainties

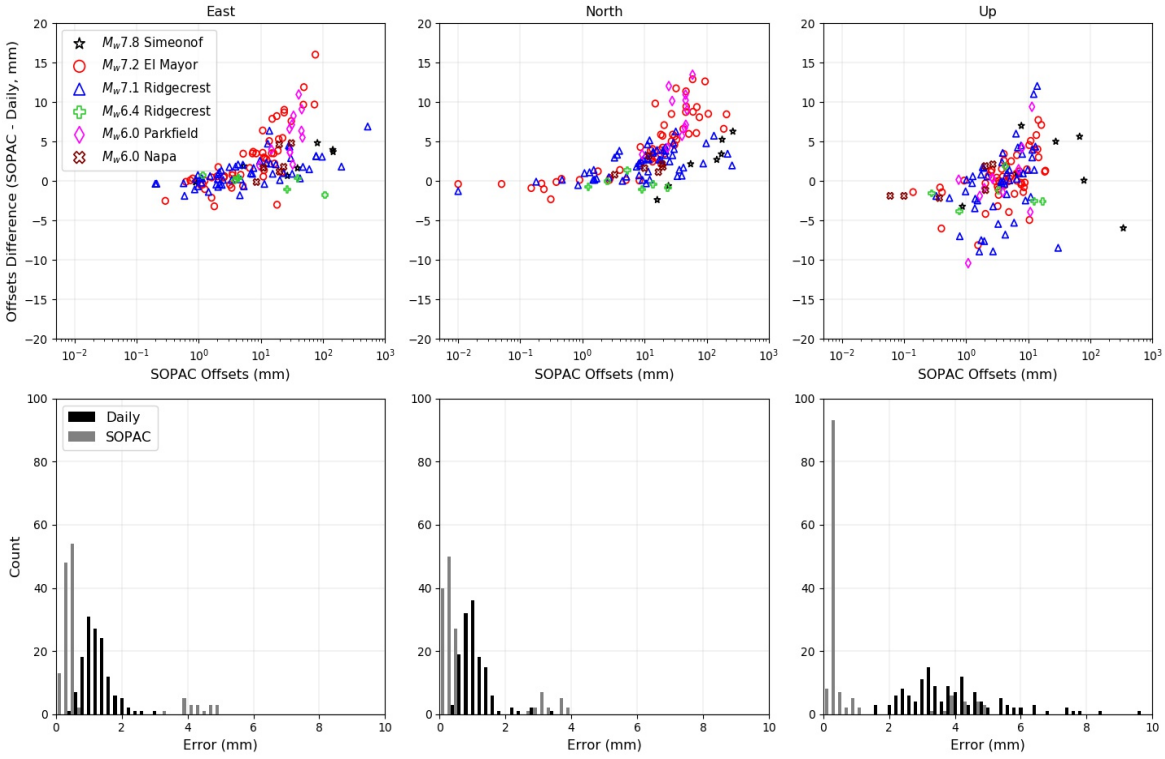

Figure 2.6. Comparison between our daily and SOPAC coseismic offsets for six events. Upper panels show the absolute difference, bottom panels show the uncertainties. Left, middle and right panels show East, North and Up components, respectively.

are more conservative as they tend to be larger, with the exception of the M_w6.4 and M_w7.1 Ridgecrest events. These events occur one-day apart and a coseismic offset is estimated for each one so that the parametric MEaSUREs model uncertainties are formally larger.

2.4.1 Comparison with Previous Studies

2004 M_w6.0 Parkfield Earthquake

The Parkfield region in central California connects the northern creeping section and southern locked section of the San Andreas fault and has experienced seven medium-sized earthquakes since 1857 (Bakun et al., 2005), six of which occurred at near-regular time intervals. Due

to this recurring behavior, this area was well instrumented with a number of different geophysical sensors, including a real-time high-rate (1Hz) 14-station GNSS network. Nevertheless, several studies of the 2004 event have only used daily GNSS displacement time series to bracket the coseismic window, while acknowledging that their offsets may contain some postseismic motion (e.g., Johanson et al., 2006; Barbot et al., 2009). Langbein et al. (2006) did use the 1Hz GNSS data sampled at 1 minute and assumed a 100s coseismic window and found that the offsets were roughly 75% of those derived from the daily solutions. Jiang et al. (2021) used the same high-rate data to continuously image evolving afterslip over minutes-to-days postseismic timespans using a 90s division between the coseismic and postseismic phases, taking into account the dynamic ground displacements and the additional time required for the passage of seismic waves at all the stations. Postseismic slip after 24 hours was $\sim$0.2m on average, about 50% smaller than the coseismic slip. They estimated a coseismic moment of $\sim 1.7 \times 10^{18} Nm$, equivalent to a moment magnitude of 6.09 with a cumulative postseismic moment of 7%, 34%, and 100% at 34 minutes, 24 hours, and 15.4 days, respectively.

All eleven stations used in our analysis of the Parkfield event exhibit significant differences between the rapid and daily coseismic offsets in the range of 2-33mm. The three stations (MIDA, LAND, and POMM) that are closest to the fault are most significant (Figure 2.7, left panels). Since all affected stations are less than two fault lengths away ("near-field"), distance to the fault instead of hypocentral distance might be more suitable in the left panel of Figure 2.5 for this event. The mostly even distribution of near-field stations in the Parkfield network results in nearly equivalent coseismic windows of $\sim$30-40 seconds but shorter than those of Langbein et al. (2006) and Jiang et al. (2021). In Figure 2.7, we show that the difference in surface displacements between daily and rapid solutions is in the same direction as the coseismic motion for stations on the east side of the fault; on the west side the postseismic vectors are slightly rotated counterclockwise.

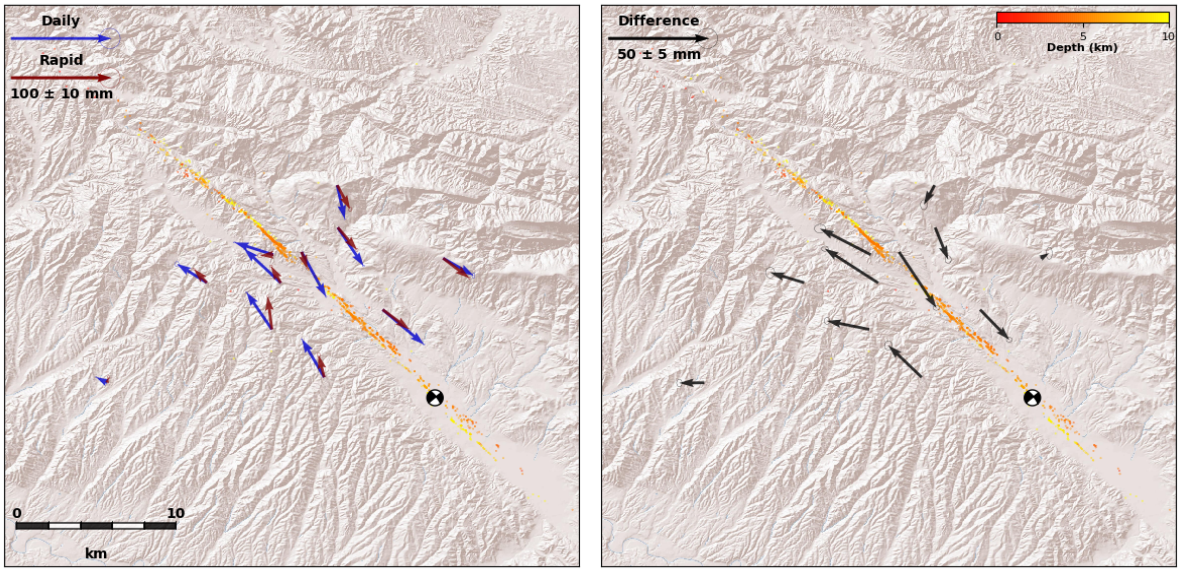

Figure 2.7. Horizontal static offsets comparison between daily (24-hour) and rapid (1Hz) displacements for the 2004 M_w6.0 Parkfield earthquake. Left panel shows the offsets from both methods. Right panel shows their differences. The 10-days of aftershocks (Waldhauser and Schaff, 2008) are color coded by hypocentral depth to highlight the rupture dimension.

2011 M_w7.2 El Mayor-Cucapah Earthquake

Wei et al. (2011) estimated coseismic offsets of up to 30cm for the 2010 M_w7.2 El Mayor-Cucapah, Mexico earthquake using two days of daily observations before and two days after the event from 23 continuous GNSS stations in southern California, 73km or greater and northwest from the epicenter. While their horizontal surface coseismic offsets of up to 20cm are in agreement with our daily estimates, our maximum rapid offset is 10% smaller and shows 18cm (Figure 2.8). Rollins et al. (2015) used coseismic offsets by Wei et al. (2011) to distinguish between models of coseismic and postseismic slip. Our results indicate rotations of the postseismic vectors consistent with their model. Gonzalez-Ortega et al. (2014) derived a postseismic fault slip model using a combination of InSAR and GNSS measurements, including data from the same set of continuous GNSS stations and field surveys closer to the rupture in northern Baja California conducted one day to one week after the event. Their analysis of the GNSS data shows postseismic displacements and a gradual decay in postseismic velocities with characteristic time scales of 66 ± 9 days and 20 ± 3 days, assuming exponential and logarithmic decay, respectively. Since the fastest evolution in postseismic motion occurs in the early period, we suggest that using our shorter coseismic time window (less than 2 minutes) may provide additional constraints on the characteristics of the postseismic decay and hence an improved understanding of crustal rheology and earthquake processes (Zhang et al., 2021). Differing from our results and those of Rollins et al. (2015), Gonzalez-Ortega et al. (2014) find that the postseismic displacements are in the same general direction as the coseismic displacements.

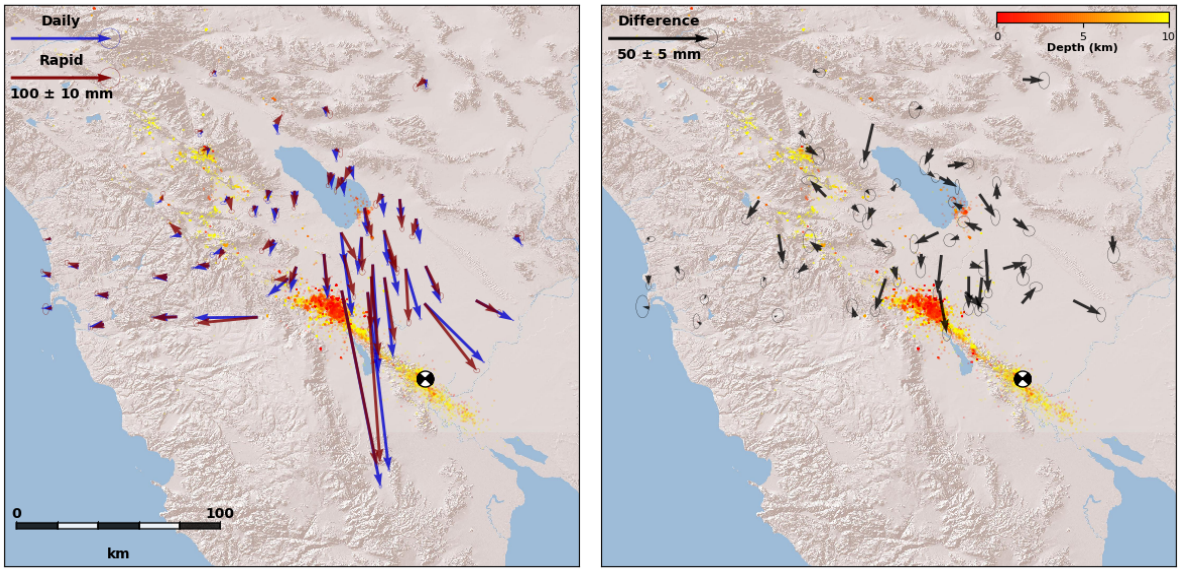

Figure 2.8. Horizontal static offsets comparison between daily (24-hour) and rapid (1Hz) displacements for the 2011 M_w7.2 El Mayor-Cucapah earthquake. Left panel shows the offsets from both methods. Right panel shows their differences. The 10-days of aftershocks (Ross et al., 2019) are color coded by hypocentral depth to highlight the rupture dimension.

2011 M_w7.3 Miyagi Earthquake

The M_w7.3 Miyagi thrust event is considered a foreshock to the great M_w9.1 Tohoku-oki mainshock occurring about 50 hours later (e.g., Miyazaki et al., 2011). For our purposes, we can consider them as distinct events. The GNSS stations are evenly distributed across the arcuate coastal geometry with the horizontal displacement vectors pointing towards the epicenter (Figure 2.9). The closest coastal stations are $\sim$150km from the epicenter with differences of $\sim$22mm or less and an apparent logarithmic decay with hypocentral distance (Figure 2.5, left panel). Shao et al. (2011) estimated horizontal coseismic offsets of more than 3cm by averaging one week before and one day after the event, in agreement with our daily estimates. However, our rapid coseismic offsets (within 1-2 minutes after the event) are only on the order of 0.5-2cm. In addition, our daily horizontal surface motions are rotated away, both clockwise and anticlockwise, from the epicentral direction (Figure 2.9). Although our results are generally consistent with Shao et al. (2011), their coseismic displacements appear to contain a significant element of postseismic motion in magnitude as well as direction, implying a more complex slip distribution. Miyazaki et al. (2011) estimated 1-2cm of coseismic offsets followed by primarily eastward transient motion of up to 1cm in the 50 hours before the Tohoku-oki mainshock using 30-minute GNSS displacement time series. These coseismic offsets are closer to our rapid estimates due to the higher sampling rate compared to 24-hour solutions, and the additional 1cm of transient motion is consistent with the 3cm of total offsets by the daily method. To overcome the limitation that slip models of thrust events are usually constrained by coastal geodetic observations only, Ohta et al. (2012) used 3-hour GNSS displacement time series as well as nine ocean bottom pressure sensors near the foreshock area to model coseismic and postseismic motions. Their horizontal postseismic offsets are less than 2cm, which is consistent with our differences (Figure 2.5).

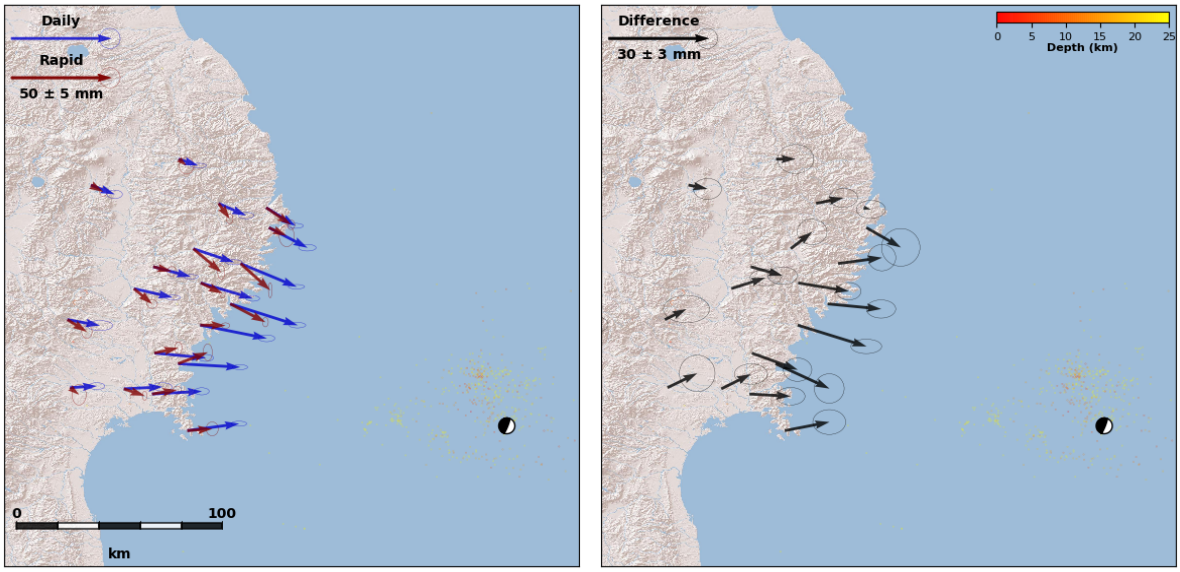

Figure 2.9. Horizontal static offsets comparison between daily (24-hour) and rapid (1Hz) displacements for the 2011 M_w7.3 Miyagi earthquake. Left panel shows the offsets from both methods. Right panel shows their differences. Aftershocks (by JMA - Japan Meteorological Agency, until the 2011 M_w9.1 Tohoku-oki origin time) are color coded by hypocentral depth to highlight the rupture dimension.

2014 M_w6.0 Napa Earthquake

Melgar et al. (2015b) used real-time GNSS displacements for static slip inversion, and compared that with retrospective analysis of both GNSS and strong-motion data. For their rapid approach, Melgar et al. (2015b) used static offsets derived by a the time when the displacement waveform variance drops to 25% of the maximum variance. In this case their coseismic time window is within 50s of earthquake origin time. In comparison with daily GNSS offsets by the Nevada Geodetic Laboratory they found that daily offsets are generally larger, as expected. According to our criteria of Equation 2.4, only 6 stations with significant offsets were taken for further analysis and comparison with daily displacements. Figure 2.10 shows the comparison between our rapid and daily offsets. There is a clear counterclockwise rotation of the vectors west of the epicenter, in agreement with Melgar et al. (2015b). However, this example of the 2014 M_w6.0 Napa Earthquake shows very small differences in magnitude between daily and rapid offsets (red crosses on Figure 2.5). That is in agreement with Klein et al. (2019) who showed that postseismic deformation over the first few weeks has small amplitudes. Lienkaemper et al. (2016) compared the patterns of postseismic slip between the 2004 M_w6.0 Parkfield and 2014 M_w6.0 Napa earthquakes. In disagreement with their expectations, postseismic deformation following the 2014 M_w6.0 Napa earthquake was shorter than one year. They also concluded that creeping (Parkfield) and locked (Napa) faults differ in their postseismic deformation behavior, with locked faults generally experiencing shorter duration.

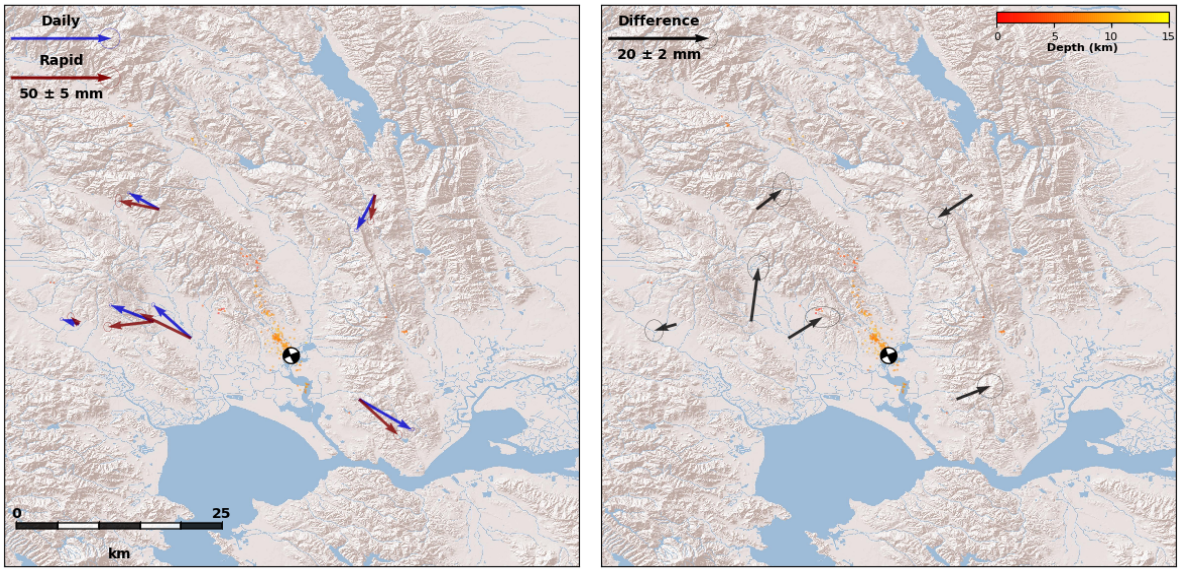

Figure 2.10. Horizontal static offsets comparison between daily (24-hour) and rapid (1Hz) displacements for the 2014 M_w6.0 Napa earthquake. Left panel shows the offsets from both methods. Right panel shows their differences. 10-days aftershocks from Waldhauser and Schaff (2008) are color coded by hypocentral depth.

2019 M_w6.4 Ridgecrest Earthquake

The 2019 M_w6.4 Ridgecrest earthquake is considered a foreshock of the M_w7.2 event that occurred less than 2 days later and discussed in Chapter 2.4. Because of the short time span between the two events ($\sim$34 hours), several studies incorporated satellite interferograms (InSAR) that span both events for simultaneous kinematic modeling of these earthquakes (Goldberg et al., 2020; Pollitz et al., 2020; Feng et al., 2020). Published coseismic slip models of this earthquake sequence show large variations, as reported by Wang and Bürgmann (2020). Figure 2.11 shows the comparison between our rapid and daily static offsets for 6 stations that stands within our criteria. Both methods show vectors that are generally in the same direction with the exception of one station north of the epicenter. Daily offsets are generally larger, as shown in Figure 2.5 as well. The differences between the two methods (right panel of Figure 2.11) are in good agreement with the earthquake focal mechanism, suggesting an early afterslip occurring in the first day of the event.

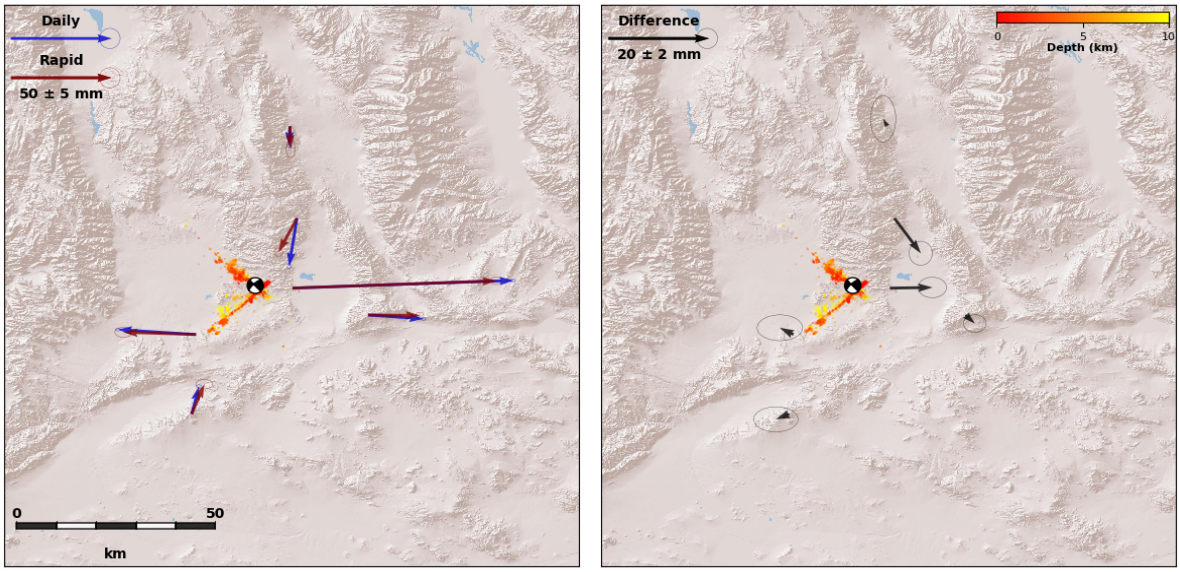

Figure 2.11. Horizontal static offsets comparison between daily (24-hour) and rapid (1Hz) displacements for the 2019 M_w6.4 Ridgecrest earthquake. Left panel shows the offsets from both methods. Right panel shows their differences. Aftershocks until the 2019 M_w7.1 Ridgecrest origin time ($\sim$1 day) from Shelly (2020) are color coded by hypocentral depth.

2020 M_w7.8 Simeonof Earthquake

On July 2020, a large M_w7.8 earthquake ruptured on the plate boundary between the Pacific and North American plates along the Alaska Peninsula. The earthquake occurred in the region between the two large earthquakes of 1938 M_w8.2 and 1946 M_w8.6, also known as the Shumagin gap. Crowell and Melgar (2020) and Xiao et al. (2021) used a combination of seismic and geodetic data to solve for static slip inversion for this earthquake. Both models result in a remaining slip deficit at the shallower portion of the region, suggesting a tsunamigenic risk in the Shumagin gap. These observations are in agreement with Liu et al. (2020), although concluding that the risk is minimal and a magnitude larger than the 2020 M_w7.8 earthquake is unlikely. Figure 2.12 shows our comparison between rapid and daily offsets. Both methods seem to agree well on offsets direction, with daily offsets that are up to 3cm larger than the rapid (Figure 2.5). These observations are also in agreement with Crowell and Melgar (2020) and Xiao et al. (2021). GNSS stations closer to the epicenter show differences in agreement with the earthquake focal mechanism, compared to the furthest station to the West. Early postseimic analysis of 10 days after the earthquake by Crowell and Melgar (2020) shows offsets that are in the same direction as the coseismic GNSS displacements, in agreement with our results.

2.4.2 Comparative 3D Analysis with 10-minute and Daily Coseismic Windows for the 2011 M_w9.1 Tohoku-oki Earthquake

We present a separate comparison for the 2011 M_w9.1 Tohoku-oki megathrust event as it naturally produces very large coseismic offsets in both horizontal and vertical directions, hence with significantly greater signal to noise ratio than the other earthquakes. In addition, we consider a single 10-minute coseismic window compared to the rapid window of $\sim$2 minutes for the nearest stations to $\sim$6 minutes for the most distant stations. Again, for the daily window we subtract the static offsets related to significant aftershocks that occurred within the day of the event. In this case, we do this for four large aftershocks: the M_w7.4 Iwate, M_w7.9 Ibaraki, M_w7.7 N. Honshu, and M_w6.2 Niigata (Table 2.2). Our high-rate GNSS analysis reveal sudden

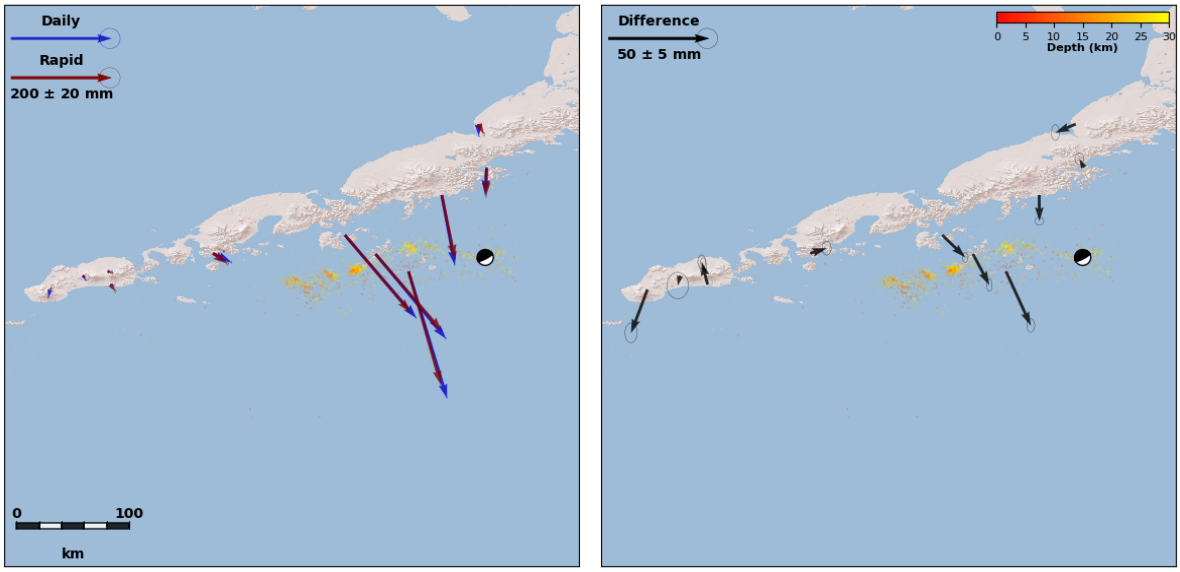

Figure 2.12. Horizontal static offsets comparison between daily (24-hour) and rapid (1Hz) displacements for the 2020 M_w7.8 Simeonof earthquake. Left panel shows the offsets from both methods. Right panel shows their differences. 10-days aftershocks from the USGS catalog are color coded by hypocentral depth.

movements in hundreds of GEONET stations, roughly 800 seconds after earthquake origin time. Xu et al. (2019) discuss whether these sudden jumps are processing artifacts or physical signals. We find after visual inspection that static offsets from 85 stations are affected by these movements and exclude them from further analysis. The differences in magnitude between the rapid, 10-minute and daily coseismic offsets are shown in Figure 2.13. The horizontal components are treated according to Equation 2.3, while the vertical offset differences are plotted as is since they are expected to exhibit both uplift and subsidence during the postseismic phase (Ozawa et al., 2011). For the horizontal components (Figure 2.13, top panels), we see no clear trend in the differences at 10 minutes, although most of them are above the zero line with a median value of $\sim$1cm. The daily differences approximate a logarithmic increase of the differences with larger rapid offsets. When plotted against rapid offsets (Figures 2.5 and 2.13), the difference when using daily offsets seems to be on the order of 10-20% of the rapid offsets. That of course, could vary with different earthquakes depending on the exact origin time (events that occurs at the beginning of the day generally would have more time to accumulate postseismic deformation until the next daily averaged position) and afterslip spatial distribution (as we are looking at hypocentral distance). In the vertical components (lower plots of Figure 2.13), we notice two features: First, it seems like the majority of stations in our 10-minute comparison experience subsidence (negative y-axis values), while we see mostly uplift for our daily comparison (positive y-axis values). Second, stations that experienced subsidence in the rapid phase have experienced mostly uplift later (2^{nd} quadrant of bottom panels), and stations that experienced uplift in the rapid phase experienced mostly subsidence later (4^{th} quadrant of bottom panels).

2.5 Implications for Fault Slip Models

We invert for fault slip of the 2019 M_w7.1 Ridgecrest, 2016 M_w7.1 Kumamoto, and 2011 M_w6.6 Fukushima earthquakes using the coseismic offsets estimated by both the rapid and daily methods. For the 2011 M_w9.1 Tohoku-oki earthquake, we also perform an inversion using a

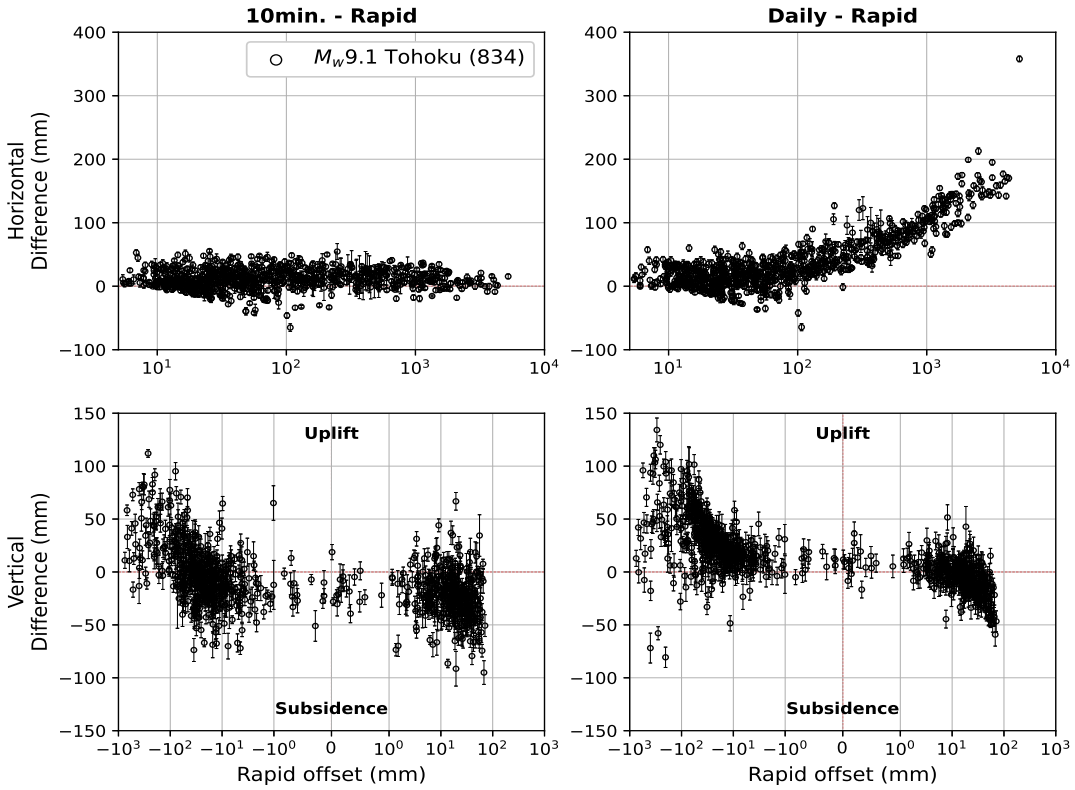

Figure 2.13. Semi-log comparison of the horizontal (upper) and vertical (lower) static offset differences between 10-minute and rapid windows (left), and between daily and rapid windows (right) for the 2011 M_w9.1 Tohoku-oki earthquake. Error bars are $\pm 1\sigma$.

10-minute window. Figures 2.16, 2.18, 2.20, and 2.22 show the direction of the fault slip together with its total magnitude, individually on each subfault.

We use the Okada (1985) elastic half-space formulation to construct the inverse problem, following the approach described in Xu et al. (2016), with the GNSS coseismic offsets as the only input. The model patch size is designed to increase with depth to mitigate the ill conditioning of the Green's functions. While we vary the dataset used as input (rapid and daily), we use the same identical fault geometry for each model. For each earthquake, we chose the smoothness constraint by inspection of the smoothness-misfit curve, identically for all data inputs. Fault surface traces follow the apparent decorrelated surface rupture identified in the InSAR phase-gradient maps for the 2019 Ridgecrest event (Xu et al., 2020a; Xu et al., 2020b). Fault geometries for the 2016 Kumamoto and 2011 Tohoku-oki events are based on previous studies by Milliner et al. (2020) and Minson et al. (2014b), respectively. The fault geometries for the 2011 Fukushima earthquake are taken from Kobayashi et al. (2012). In our modeling results we present the total slip, defined as

$$U_{Total} = \sqrt{{U_{ss}}^2 + {U_{ds}}^2} \tag{2.5}$$

where U_{ss} and U_{ds} are the strike-slip and dip-slip components of slip for each patch, respectively. When comparing the postseismic moment accumulated during a given period of time, we account for the origin time at the day of the earthquake until the middle of the next day. The reason for this is that the first daily position after the earthquake is averaged around 12:00 UTC on the following day.

2011 M_w9.1 Tohoku-oki Earthquake

The 2011 M_w9.1 Tohoku-oki megathrust earthquake ruptured a very wide (hundreds of kilometers) segment of the Japan Trench, causing tremendous damage due to severe shaking and the generated tsunami (e.g., Mori et al., 2011; Simons et al., 2011). We used a weighted

average of the horizontal and vertical surface motions to create a 50x50 km grid to capture the predominant features of motion and compare the offsets based on the rapid, 10-minute and daily coseismic windows (Figure 2.14). The earthquake generated large horizontal and vertical offsets with surface horizontal motions pointing towards the epicenter, and areas of both subsidence and uplift. We calculate a few additional centimeters of horizontal motion towards southern Honshu after 10 minutes and up to $\sim$20cm of widely distributed motion mostly along the coastal region with a 24-hour window (Figures 2.13 and 2.14), thus quantifying the contribution of early postseismic motions.

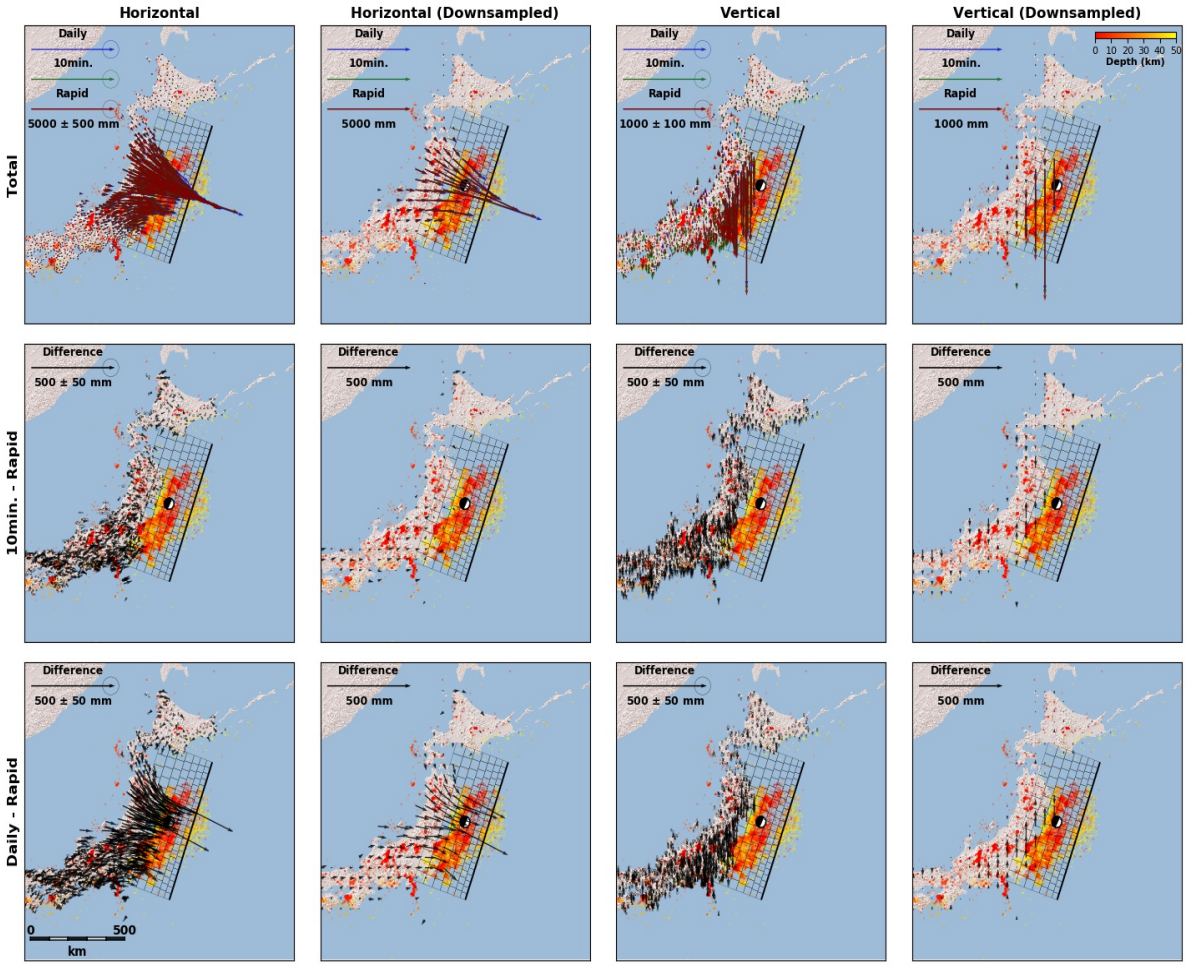

Figure 2.14. Horizontal (left two sets of panels) and vertical (right two sets of panels) static offsets comparison between daily (24-hour), 10-minute, and seismogeodetic displacements for the 2011 M_w9.1 Tohoku-oki earthquake. Top panels show the offsets from all three methods, middle panels show the differences with the 10-minute window and rapid offsets, and bottom panels show the differences between daily and rapid. First 10-days aftershocks (by JMA - Japan Meteorological Agency) are color coded by hypocentral depth to highlight the rupture dimension, thick black lines denote the model surface trace. We have eliminated the stations with insignificant horizontal offsets using the same criteria as for the earlier earthquakes. Since many stations were affected and the GEONET is so dense, the patterns are better discerned using a 50x50km grid of weighted averages for the daily and 10-minute differences in both horizontal (second column of panels) and vertical (fourth column of panels) components.

Ito et al. (2011) used the same geodetic network together with seafloor stations to study both coseismic and early postseismic deformation. They calculated the coseismic offsets from 6 minutes before to 9 minutes after origin time, and the early postseismic period for the following 8 hours. In agreement with our observations with a 10-minute window, most of the surface deformation during the first few hours occurs southwest of the epicenter. However, while the maximum horizontal motion according to their analysis reaches ∼30cm over 8 hours, we see up to ∼5cm of additional motion after 10 minutes and up to ∼20cm after 24 hours. When comparing these numbers, we need to take into consideration that their early postseismic window of 8 hours includes several large aftershocks such as the M_w7.9 Ibaraki earthquake. In our analysis, we estimated the aftershock's corresponding coseismic offsets and subtracted them from the 24-hour solutions. For the vertical component we notice a different behavior after 10 minutes where the closer stations are generally uplifting up to ∼10cm while the farther stations are subsiding up to ∼10cm compared to the rapid offsets. The differences after 24 hours indicate mostly uplift of up to ∼14cm. Ito et al. (2011) suggests mostly subsidence for the stations around southern Honshu. Another study by Ozawa et al. (2011) reveals a similar behavior from GNSS displacements in the following two weeks after the event, where most of the coastal stations experience uplift. They estimated a ∼10cm uplift along the coast and a few centimeters of subsidence in farther inland stations, both of which are comparable with our results (Figure 2.13, bottom right panel).

For this earthquake, we inverted for fault slip using the rapid coseismic window (2-6 minutes), a single 10-minute window for all stations and a 24-hour window. Figures 2.15 and 2.16 shows a simplified model (single fault plane with a constant dipping angle) using the displacements calculated for each coseismic window as input, together with their differences. Since we are using a simplified model, our objective is limited to a comparative analysis of the three coseismic widows to assess the contributions of early postseismic deformation, rather than a comparison with previously published coseismic and postseismic slip models. All three models indicate a peak slip of more than 20m very close to the hypocenter, roughly 20-30km deep. The most notable difference between the models is the shallow region from the surface down to

20km depth. Our preferred model for the constant 10-minute window indicates up to $\sim$2.5m of extra slip located around the shallow part and extends to the south. Our preferred model for the daily (using 24-hour positioning) window indicates up to $\sim$5m of extra slip located around a broader area of the shallow fault. Using the resulted moment magnitudes for each model (Figure 2.15, top panels) we assess early postseismic moment of M_w8.06 ($\sim$4% of the coseismic moment) accumulated during the first 4-8 minutes and M_w8.38 ($\sim$12% of the coseismic moment) accumulated during $\sim$18 hours, using a shear modulus of 58GPa.

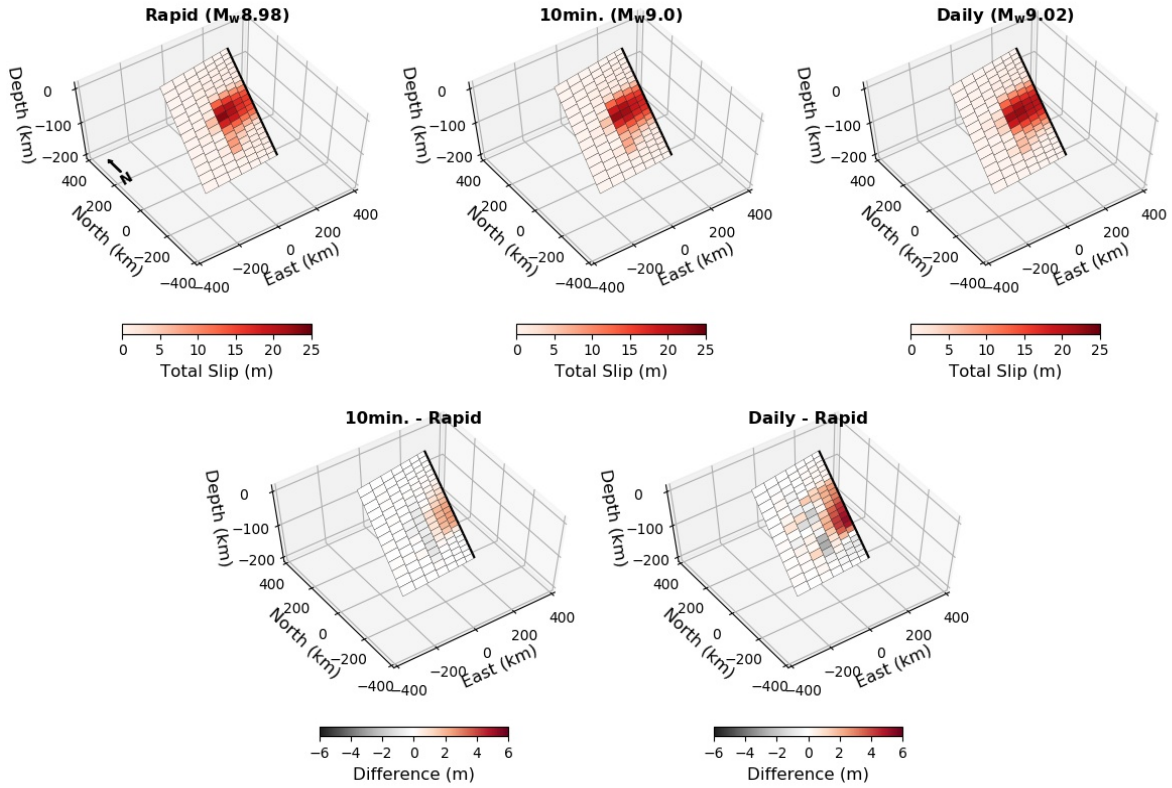

Figure 2.15. Fault slip models for the 2011 M_w9.1 Tohoku-oki earthquake using rapid (top left), 10-minute (top middle) and daily (top right) offsets as input. Bottom panels show the differences between the models. The resulted moment magnitudes assuming a shear modulus of 58*GPa* are shown at the title.

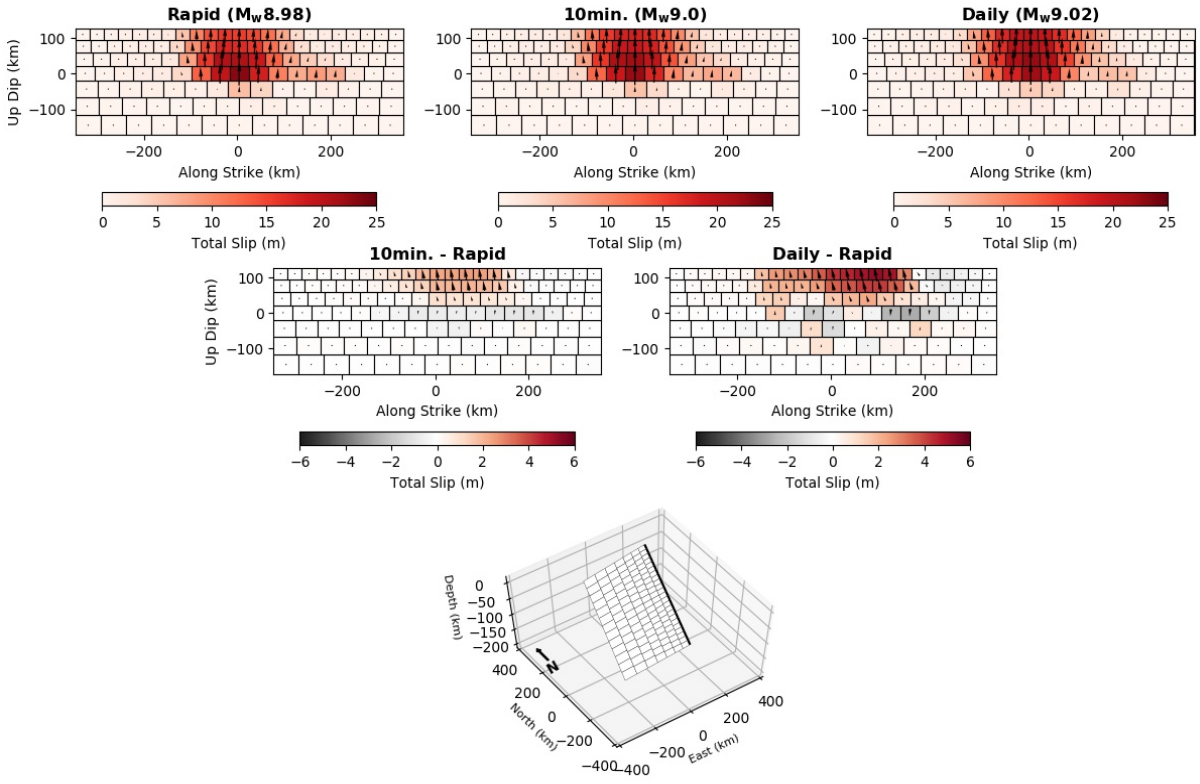

Figure 2.16. Fault slip models for the 2011 M_w9.1 Tohoku-oki earthquake using rapid offsets (left), 10-minute offsets (middle), and daily offsets (right). Middle panels show the differences between the models. The resulted moment magnitude assuming a shear modulus of 58 GPa is shown at the title. Bottom panel shows the fault model geometry.

2011 M_w6.6 Fukushima Earthquake

The Fukushima (M_w6.6, 10km depth) event was a normal earthquake that occurred inland and was surrounded by a network of stations that produced up to ∼18mm difference between our daily and rapid coseismic offsets. However, about 4-5 of the stations, at distances of ∼40km and greater, appear to have observed motions consistent with contraction (negative differences). This earthquake, in the Fukushima-Hamadori area (Mizoguchi et al., 2012; Fukushima et al., 2013; Kobayashi et al., 2012; Toda and Tsutsumi, 2013) occurred one month after the M_w9.1 Tohoku-oki earthquake, in a region of high seismic activity that started a few days after the March 11 event. This event provides an opportunity to investigate an inland normal earthquake that involved several faults, reflecting the somewhat wide range of differences between the rapid and daily coseismic offsets (Figure 2.5). We invert for fault slip on three dipping faults that were mapped using InSAR discontinuities (Kobayashi et al., 2012). Our two slip models (Figures 2.17 and 2.18) show considerable slip along the westernmost Shionohira fault that extends down dip towards the south, with a maximum slip of 2.2 and 2.4 meters, respectively. Most of the slip on the middle Itozawa fault is located at the southern end and extends to down to 2-5km depth. The resulting slip on the easternmost Yunotake fault reaches a maximum of 1.9 and 2.2m for both models, with a shallow dislocation extending to ∼5km down dip towards the northwest.

The total coseismic moment for our preferred models is equivalent to M_w6.53 and M_w6.57 for the rapid and daily datasets, respectively, assuming a shear modulus of 30GPa. This corresponds to a postseismic moment equivalent to M_w5.95 (∼13% of the coseismic moment), accumulated during the first ∼30 hours. Kobayashi et al. (2012) and Fukushima et al. (2013) used InSAR observations from April 18, a week after the event, to explore its coseismic deformation. Vertical displacement from their images seems to agree with the main features of our models, with little to no slip occurring at the shallow part of the middle (Itozawa) fault and significant dislocation taking place at the other two, mainly at the middle section of the Shionohira fault and the northwestern section of the Yunotake fault. Fukushima et al. (2013) used a similar fault

geometry where the Itozawa fault extends at depth with varying dip angle. Their resulting moment magnitude for the Shionohira-Itozawa faults is M_w6.64 assuming a 20GPa shear modulus, and M_w6.76 for the Yunotake fault assuming 30GPa. In order to directly compare with our results, we convert these values to a total of M_w6.96 by assuming a shear modulus of 30GPa for both faults. Using the exact fault geometry as ours, the coseismic model by Kobayashi et al. (2012) results in a total moment magnitude of M_w6.73 assuming the same shear modulus. It is likely that their larger estimates result from a longer InSAR data span of 7 days and a more complete mapping near the fault rupture, compared to our data span of minutes and 24-hours for the rapid and daily models, respectively. Rapid field surveys conducted after the Fukushima earthquake indicated 2m of vertical displacement along the Shionohira fault and 0.9m of displacement along the Yunotake fault (Mizoguchi et al., 2012; Toda and Tsutsumi, 2013). These values are comparable with our daily model's shallow slip for these two faults.

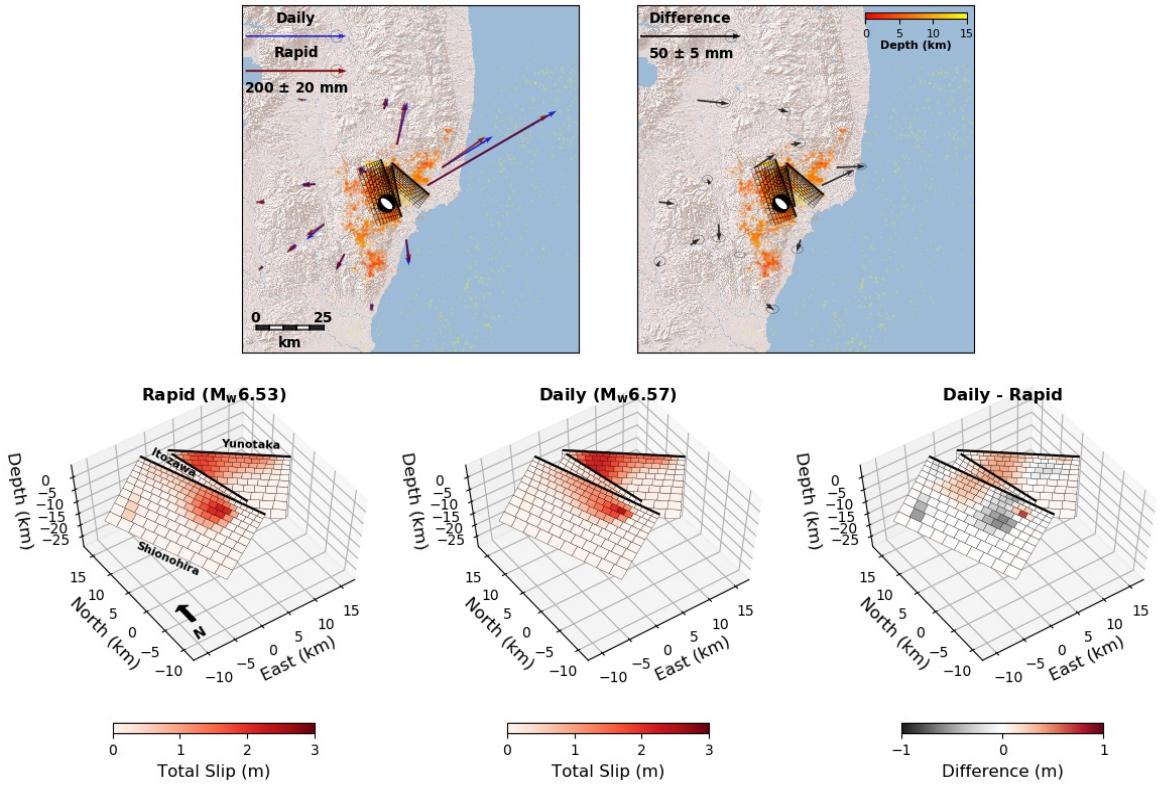

Figure 2.17. Top: Horizontal static offsets comparison between daily (24-hour) and rapid (1Hz) displacements for the 2011 M_w6.6 Fukushima earthquake. Left panel shows the offsets from both methods; right panel shows their difference. The 10-days of aftershocks (by JMA - Japan Meteorological Agency) are color coded by hypocentral depth to highlight the rupture dimension, thick black lines denote the model surface trace. Bottom: Fault slip models using rapid offsets (left), daily offsets (middle), and their differences (right). The resulted moment magnitude assuming a shear modulus of 30*GPa* is shown at the title.

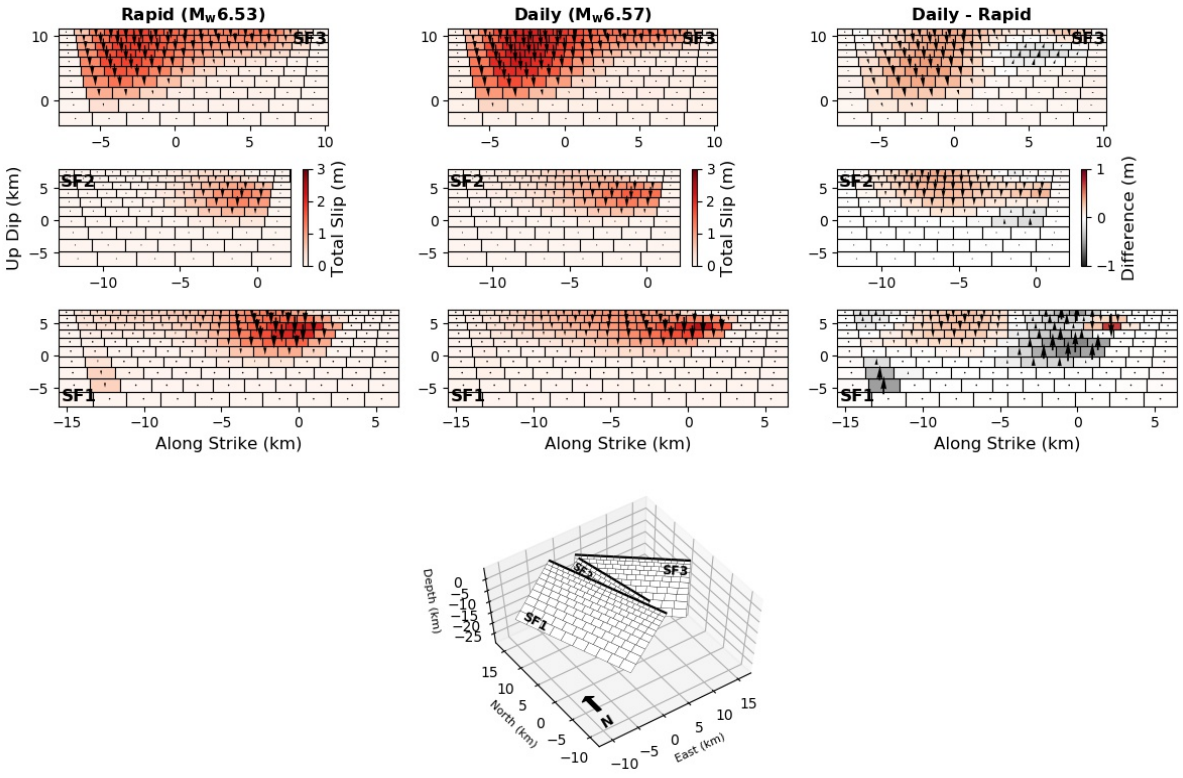

Figure 2.18. Fault slip models for the 2011 M_w6.6 Fukushima earthquake using rapid offsets (left), daily offsets (middle), and their differences (right). The resulted moment magnitude assuming a shear modulus of 30GPa is shown at the title. Bottom panel shows the fault model geometry.

2016 M_w7.1 Kumamoto Earthquake

The inland 2016 M_w7.1 Kumamoto earthquake ruptured multiple fault traces with a predominantly right-lateral strike-slip mechanism and damaged a wide area in the central part of Kyushu Island. The resulting displacements were observed with excellent GNSS station coverage (Shirahama et al., 2016; Kawamoto et al., 2016a). Figures 2.19 and 2.20 shows our rapid and daily slip models for this earthquake. The coseismic vectors have differences as large as $\sim$15cm near the epicenter (outside of the scale in Figure 2.5) to $\sim$1cm at distances greater than 50km. For both models, slip is concentrated at the northern part of the Hinagu fault (the smaller subfault to the southwest) and the middle segment of the longer Futugawa fault with a maximum total slip of 5.8 and 6.2m for the rapid and daily models, respectively. The resulted moment magnitudes are M_w7.02 and M_w7.07, respectively, assuming a shear modulus of 30GPa. This corresponds to a postseismic moment over the early postseismic phase (of $\sim$20 hours) of M_w6.57, or $\sim$20% of the coseismic moment. The most noticeable postseismic features are (1) more than 1m of additional slip at the shallow part of the Hinagu fault, and (2) more than 1m of additional slip at the northeastern segment of the Futugawa fault. It is worth pointing out that there are also some patches were the rapid model has more slip (up to 0.8m) than the daily model, mostly around the center of Futugawa fault. However, since most of the model patches shows a positive difference (daily is larger than rapid), in agreement with the mostly positive static offset differences (Figure 2.5), we are convinced that these signals are related to early postseismic deformation. Both seismicity and slip are minimal below the Aso caldera at the northern part of the Futugawa fault. Other studies suggest that higher crustal temperatures due to the presence of a magma chamber is responsible for the lack of slip at depth in that region (Lin et al., 2016; Yagi et al., 2016). When comparing these models to Milliner et al. (2020), we see similar features on the Futugawa fault with maximum slip around 6-8km depth, terminated near the Aso caldera. However, our coseismic slip is more localized at the Hinagu fault, taking place at the northeastern segment. Their coseismic analysis is based on one-hour averaged GNSS positions before and

after origin time, which results in a total magnitude of M_w7.06, a comparable value that falls between our rapid and daily magnitudes. Hao et al. (2017) used both regional strong motion and teleseismic broadband waveforms to investigate the coseismic rupture, with a slip distribution that is similar to our results. To solve for the postseismic slip, Milliner et al. (2020) used a spatiotemporal filtering technique on 5-minute GNSS time series. Their model for afterslip after one day shows substantial slip around two regions of the Hinagu fault; the north segment, and below 5km depth at the south segment. That matches the difference between our daily and rapid models. However, their postseismic moment after the first day is equivalent to M_w6.1 or 4% of their coseismic moment, which is significantly lower than our results.

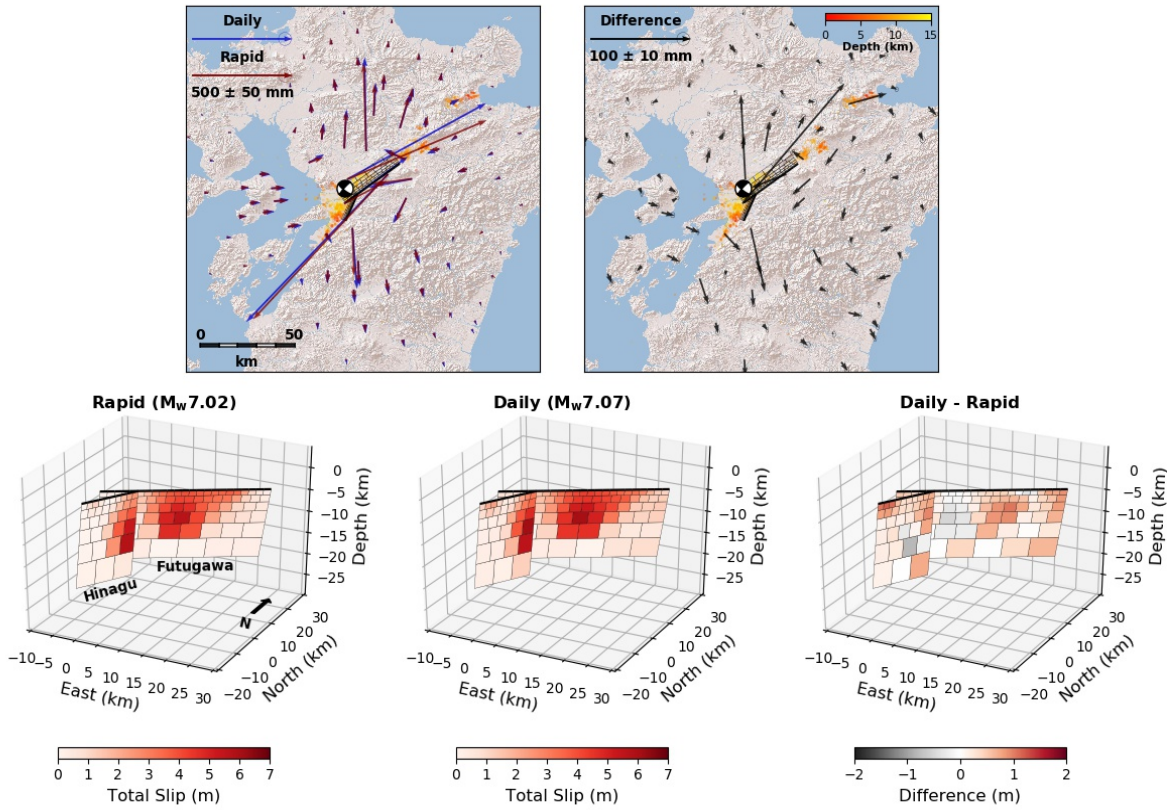

Figure 2.19. Top: Horizontal static offsets comparison between daily (24-hour) and rapid (1Hz) displacements for the 2016 M_w7.1 Kumamoto earthquake. Left panel shows the offsets from both methods; right panel shows their difference. The 10-days of aftershocks (Yue et al., 2017) are color coded by hypocentral depth to highlight the rupture dimension, thick black lines denote the model surface trace. Bottom: Fault slip models using rapid offsets (left), daily offsets (middle), and their differences (right). The resulted moment magnitude assuming a shear modulus of 30GPa is shown at the title.

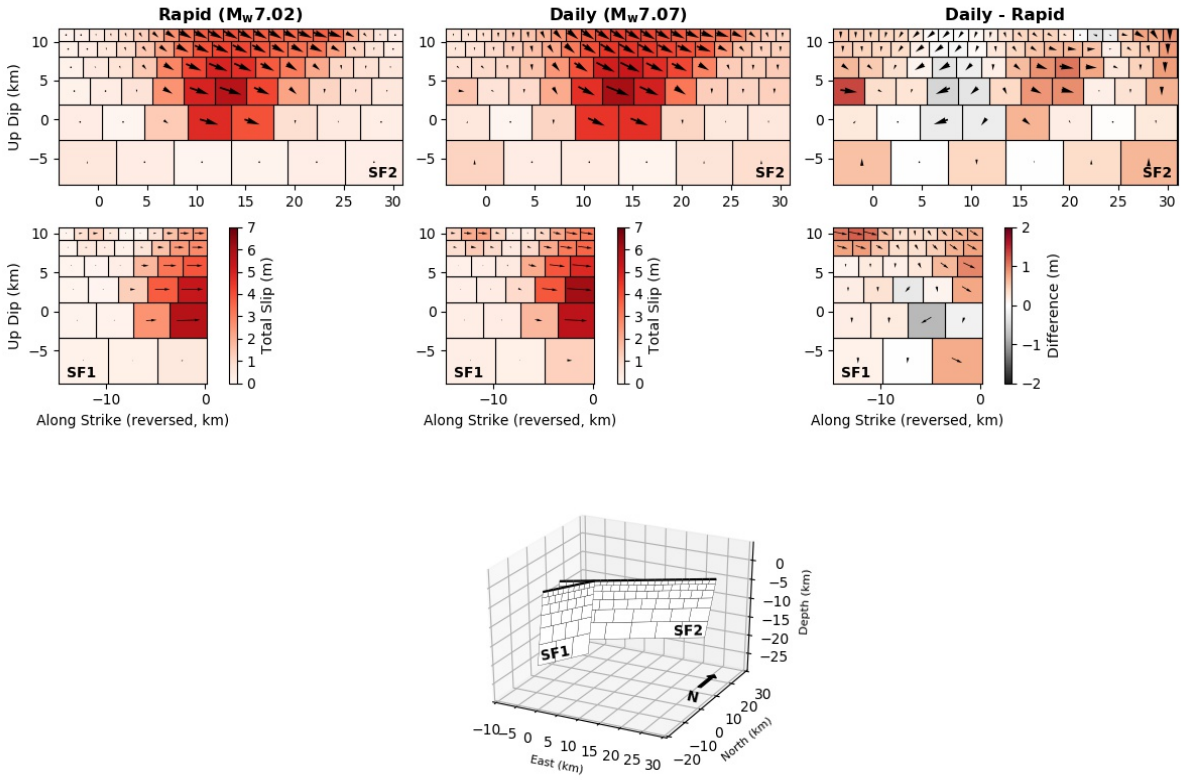

Figure 2.20. Fault slip models for the 2016 M_w7.1 Kumamoto earthquake using rapid offsets (left), daily offsets (middle), and their differences (right). The resulted moment magnitude assuming a shear modulus of 30*GPa* is shown at the title. Bottom panel shows the fault model geometry.

2019 M_w7.1 Ridgecrest Earthquake

The 2019 Ridgecrest earthquake sequence started with an M_w6.4 foreshock followed by an M_w7.1 mainshock, ∼34 hours later. We did not include the M_w6.4 event in our models since only 5 stations met our criteria for a significant coseismic offset (the results are shown in Figure 2.11). The horizontal offsets for the M_w7.1 Ridgecrest event (Figures 2.21 and 2.22) had significant differences between the rapid and daily coseismic windows of up to ∼17mm. The slip inversions for the mainshock are shown at the bottom panels of Figure 2.21 and in Figure 2.22. We find that in both rapid and daily models most of the slip occurs along the northern segment close to the hypocenter where maximum slip exceeds 3.5m and 5m for rapid and daily models, respectively. The southern segment has an additional area of localized slip that reaches ∼3m. We attribute the difference in the models (Figure 2.21, bottom right panel) to early postseismic deformation taking place during the first few hours after the event. Most of these differences (of more than 1.5m) appear to be in the shallow part of the northern segment. Recent postseismic studies that rely on InSAR (Wang and Bürgmann, 2020) and campaign GNSS (Brooks et al., 2020) suggest an asymmetric distribution of afterslip that occurs mostly in the northern segment of the fault. Wang and Bürgmann (2020) found a maximum of 5cm of displacement in the line of sight over ∼1-2 months following the event. This maximum is centered northwest of the earthquake epicenter, in agreement with the location of maximum difference between our models (Figure 2.21). Looking at the closest stations with ∼1.5cm of difference between our two methods (P595 and P594, Figure 2.5), we can roughly assess the magnitude of the postseismic deformation of the first day to be about 30% of their coseismic deformation. Assuming a shear modulus of 30GPa, the resulting moment magnitudes are M_w7.02 and M_w7.03 for the rapid and daily solutions, respectively, and the additional seismic moment released in the early postseismic period (of ∼33 hours) is equivalent to M_w6.23 (or 6.5% of the coseismic moment). Both models show very little to no slip at the M_w6.4 foreshock segment (the southwest striking fault). The USGS was able to survey closer to the epicentral region than other efforts (Brooks et al., 2020).

Along with no indication of surface rupture, they find no evidence that the M_w6.4 rupture plane was reactivated during the M_w7.1. On the other hand, Ponti et al. (2020) suggests some local reactivation at the intersections between the two faults.

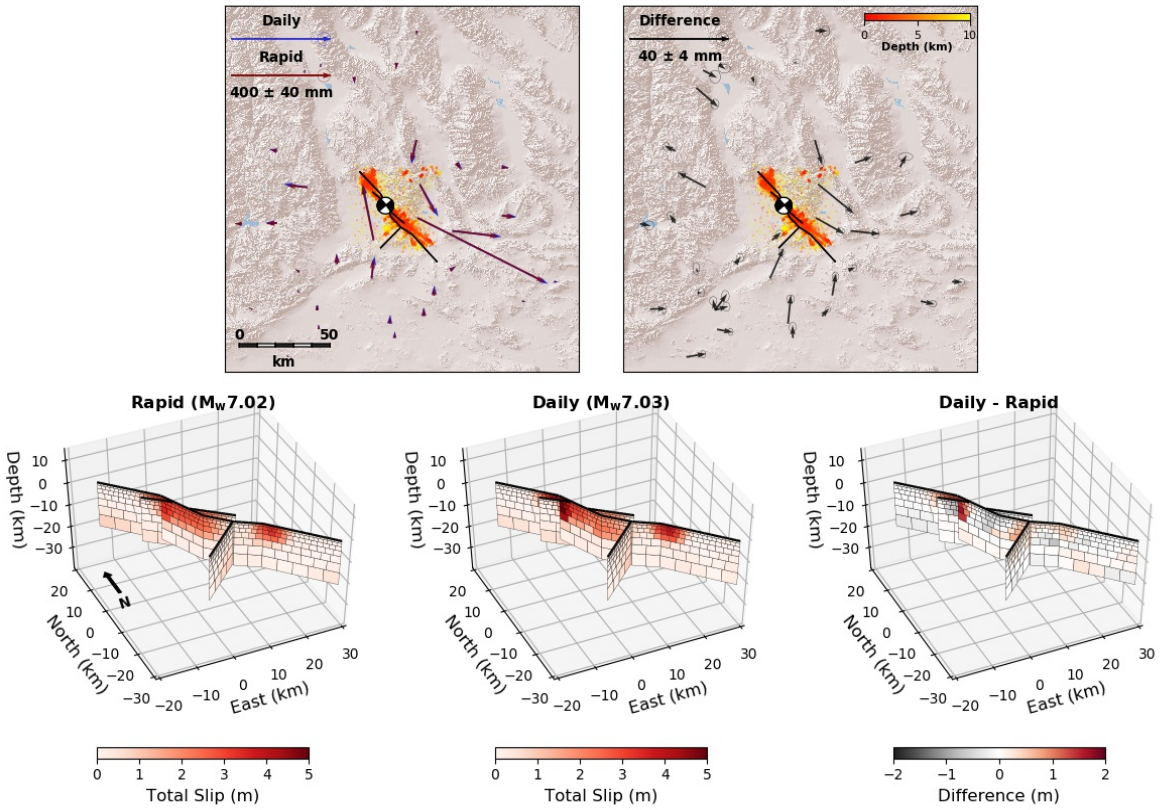

Figure 2.21. Top: Horizontal static offsets comparison between daily (24-hour) and rapid (1 Hz) displacements for the 2019 M_w7.1 Ridgecrest earthquake. Left panel shows the offsets from both methods; right panel shows their differences. The 10-days of aftershocks (Shelly, 2020) are color coded by hypocentral depth to highlight the rupture dimension, thick black lines denote the model surface trace. Bottom: Fault slip models using rapid offsets (left), daily offsets (middle), and their differences (right). The resulted moment magnitude assuming a shear modulus of 30GPa is shown at the title.

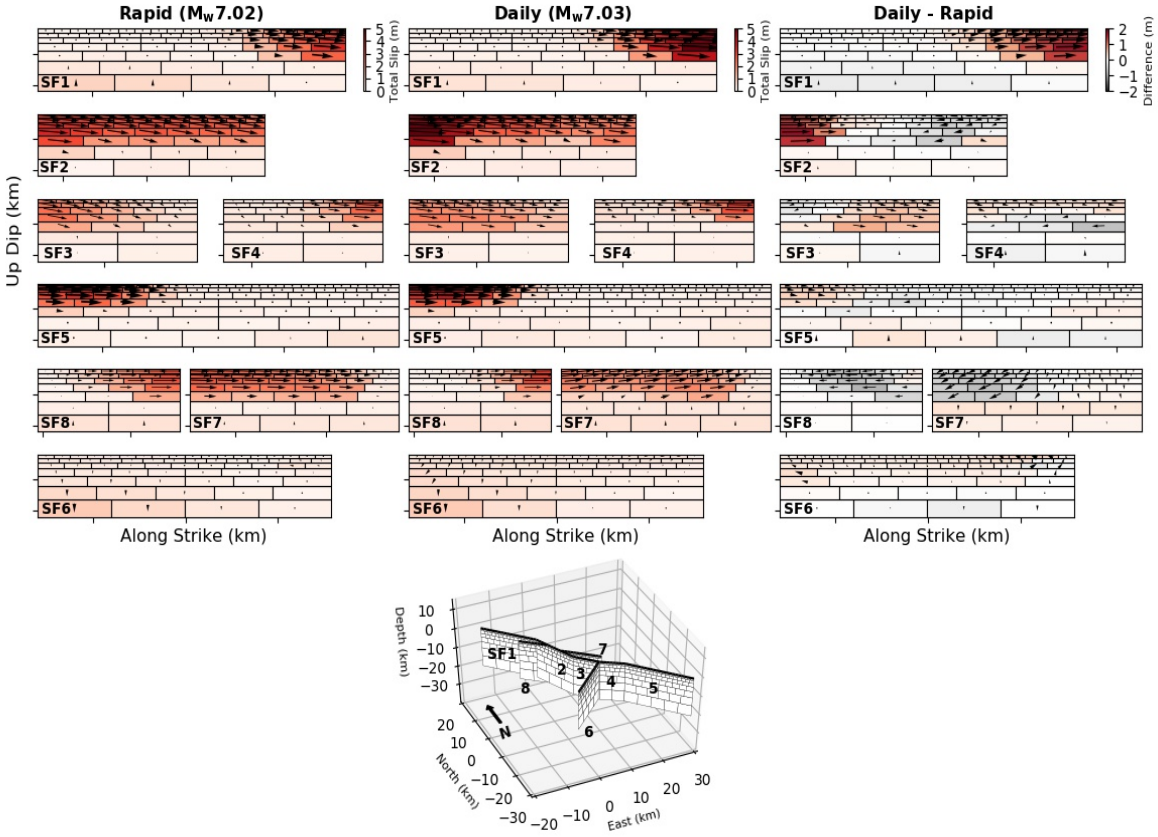

Figure 2.22. Fault slip models for the 2019 M_w7.1 Ridgecrest earthquake using rapid offsets (left), daily offsets (middle), and their differences (right). The resulted moment magnitude assuming a shear modulus of 30*GPa* is shown at the title. Bottom panel shows the fault model geometry.

2.6 Discussion and Conclusions

We have identified the transition points from the coseismic phase to the postseismic phase for ten earthquakes (Table 2.1) using seismic velocities integrated from strong motion accelerations that define the coseismic window and rapid static coseismic offsets from high-rate GNSS displacements at the transition point. Our overall results indicate significant differences between the daily and rapid estimates of permanent coseismic offsets, which we attribute to some combination of early postseismic processes (e.g., afterslip, viscoelastic relaxation). It follows that the choice of the apparent coseismic window can result in significant mix between coseismic slip associated with seismic rupture and postseismic fault slip. In the following sections, we first compare the rapid coseismic offsets from our seismogeodetic approach to previous studies of the 2004 M_w6.0 Parkfield, 2010 M_w7.2 El Mayor-Cucapah, and 2011 M_w7.3 Miyagi earthquakes. Then, we generate two sets of fault slip models each for the 2019 M_w7.1 Ridgecrest, 2016 M_w7.1 Kumamoto, 2011 M_w6.6 Fukushima and 2011 M_w9.1 Tohoku-oki earthquakes using the rapid and daily coseismic offsets as input. Considering its great magnitude and significant vertical deformation, we also invert for slip using a 10-minute coseismic window for the 2011 M_w9.1 Tohoku-oki earthquake. Our intention is not to present improved coseismic models for these events compared to previous studies, but rather to determine what effect lumping together coseismic and postseismic deformation has on coseismic slip inversions. Comparing these models also serves as an assessment of the spatial distribution of early postseismic slip, as well as a measure of coseismic and early postseismic moment.

While all earthquakes in Table 2.1 demonstrate significant differences between the daily and rapid coseismic offsets, the 2014 M_w6.0 Napa, 2019 M_w6.4 Ridgecrest, and 2020 M_w7.8 Simeonof events do not have enough stations with offsets to characterize them or compare to previous studies. Figure 2.23 shows the average slip with depth for each of our models for the four different earthquakes. It is clear that the coseismic slip models that are based on the 24-hour GNSS solutions (daily method) experience more slip than models that are based on

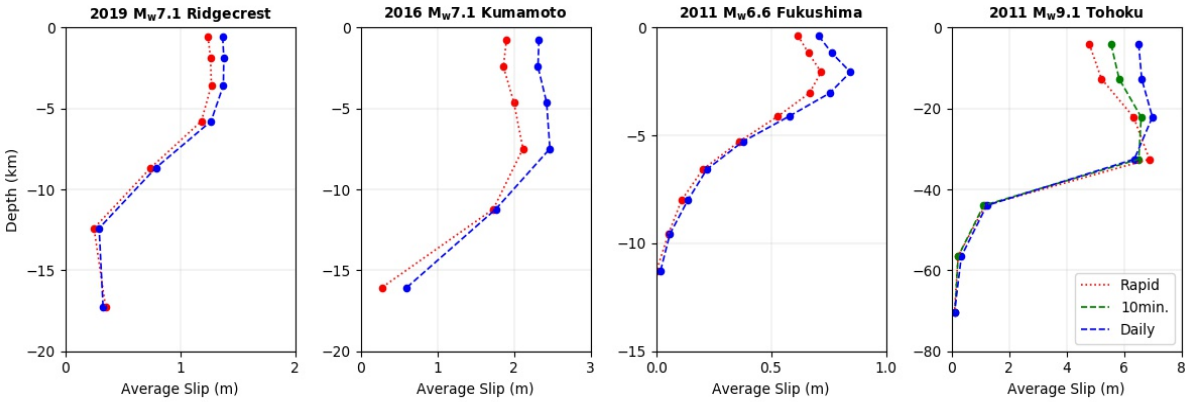

Figure 2.23. Averaged slip as a function of depth for the earthquakes modeled in this study. Red lines are for the rapid models, green line for the 10-minute model (only for the 2011 M_w9.1 Tohoku-oki earthquake), and blue lines for the daily models.

high-rate GNSS solutions (rapid method). These results are consistent with the additional surface deformation when considering longer time windows as part of the coseismic phase. For the 2011 M_w9.1 Tohoku-oki event, we also notice a clear shift from $\sim$5 meters of average slip in the shallower portion of the fault, to $\sim$5.5 and $\sim$6.5 meters using the 10-minute and daily windows, respectively.

Acknowledgements

Chapter 2, in full, is a reformatted version of material as it appears in Journal of Geophysical Research - Solid Earth: Golriz, D., Bock, Y., Xu, X. (2021). "Defining the Coseismic Phase of the Crustal Deformation Cycle With Seismogeodesy". Journal of Geophysical Research: Solid Earth, 126(10), doi:10.1029/2021JB022002. The dissertation author was the primary investigator and author of this material.

Chapter 3

Real-time Seismogeodetic Earthquake Magnitude Estimates for Local Tsunami Warnings

3.1 Background

Tsunamis are a devastating natural, high-fatality hazard (Bryant, 2008). Because most tsunamis are generated by earthquakes, the first indication of a potentially life-threatening tsunami is the earthquake itself. Effective tsunami warning systems must therefore detect, locate, and estimate the magnitude of the causative earthquake to infer tsunamigenic potential, and warn coastal populations as soon as possible after initiation of fault rupture. Rapid characterization of the earthquake focal mechanism also aids in inferring tsunamigenic potential (Melgar and Bock, 2015; Melgar et al., 2016). Most tsunamis originate from Earth's subduction zones due to thrust faulting although earthquakes with other source mechanisms have also generated tsunamis (Elbanna et al., 2021; Scott, 2021). For example, the 2012 M_w8.6 predominantly strike-slip intraplate event off Sumatra, Indonesia (Satriano et al., 2012), generated a tsunami that was recorded at sea-level stations as far as 4800km from the epicenter and by ocean bottom pressure sensors (i.e., DART buoys) in the Indian Ocean (Wang et al., 2012a). Similarly, the 2009 M_w8.1 Samoa earthquake was a normal faulting, outer-rise type event that produced a sizeable tsunami with 189 fatalities (Okal et al., 2010).

Current warning systems are well-developed for basin-wide and regional tsunamis. For earthquakes over M_w8.0, they rely mainly on long period ($>\sim$300 seconds) seismic data recorded by broadband seismometers at distances greater than $\sim$500km from the epicenter. However, for large tsunamigenic events, broadband velocity data may go off-scale ("clip") if measured too close to the seismic rupture. Therefore, tsunami warnings to the coastal communities located closest to the earthquake rupture may not be issued in a sufficiently timely manner. Another serious challenge for tsunami warning is the identification of tsunami earthquakes that release very little high-frequency energy that can be felt by humans (Kanamori, 1972; Tanioka et al., 1997; Polet and Kanamori, 2000). In this case, the predicted amplitudes of the tsunami waves generated may be underestimated.

A prototypical example of the over-reliance on seismic data is the 2011 M_w9.1 Tohoku-oki, Japan earthquake and tsunami that devastated the northeast coast of Honshu. The Japan Meteorological Agency (JMA) determined a magnitude M_w7.9 and issued a tsunami warning within 3 minutes of rupture initiation. This underestimate may have resulted in a delay of coastal evacuation (Hoshiba and Ozaki, 2014). Improved seismic methods have been developed to increase timeliness and accuracy, in particular the inversion of the W-phase (Kanamori, 1993) to obtain the W-phase Centroid Moment Tensor (WCMT) (Kanamori and Rivera, 2008) and corresponding moment magnitude, M_w. The WCMT and M_w can be available within 5-20 minutes of earthquake origin time, thus making it more suitable for local tsunami warning (Rivera and Kanamori, 2009). Another issue with insufficiently broadband seismic data is magnitude saturation for earthquakes greater than $\sim M_w$8.0, which can result in significant magnitude underestimates (Kanamori, 1977), as occurred in the JMA response to the 2011 M_w9.1 Tohoku-oki event (Hoshiba and Ozaki, 2014). In the vicinity of large earthquakes, ground motions can exceed the dynamic range of broadband seismometers and result in a clipped record. Therefore, seismic networks also include strong-motion accelerometers that do not clip. However, for earthquake source parameter determination methods requiring surface displacement information, acceleration waveforms must be doubly integrated, often causing drifts in displacement as a

result of "baseline" errors (Graizer, 1979; Iwan et al., 1985; Boore, 2001; Boore et al., 2002; Smyth and Wu, 2007; Melgar et al., 2013a). To improve local tsunami warnings, other sensors are deployed. For example, ocean-bottom pressure sensors, near-shore GNSS-mounted buoys, autonomous wave gliders, and seafloor GNSS-acoustic instruments (Kido et al., 2011; Hoshiba and Ozaki, 2014; Sato et al., 2013; Yokota et al., 2018).

Real-time GNSS networks can measure precise ($\sim$1cm single epoch) high-rate (1-10Hz) displacements including dynamic and static (permanent) coseismic offsets, while not experiencing clipping or magnitude saturation (e.g., Bock et al., 2000; Larson et al., 2003; Bock et al., 2004; Genrich and Bock, 2006; Wright et al., 2012). Empirical scaling relationships using peak-ground-displacements (PGD) measured from high-rate GNSS data (Crowell et al., 2013; Melgar et al., 2015a; Ruhl et al., 2019) have been successfully used to rapidly estimate magnitude in earthquake early warning contexts (Crowell et al., 2018; Hodgkinson et al., 2020; Mattioli et al., 2020; Melbourne et al., 2021). Retrospective studies of several tsunamigenic events in Japan and Chile have demonstrated the utility of these scaling relationships for tsunami warning systems and models of coastal inundation (Blewitt et al., 2006; Ohta et al., 2012; Melgar et al., 2016). Several earthquake early warning systems have already incorporated GNSS displacement data into their magnitude determination algorithms. These include GlarmS (Grapenthin et al., 2014) and BEFORES (Minson et al., 2014a) in the Western U.S., G-FAST in the Western U.S. and Chile (Crowell et al., 2018; Barrientos et al., 2018), and REGARD in Japan (Kawamoto et al., 2016b). In addition to rapid magnitude estimation, studies have demonstrated that GNSS displacements can provide rapid centroid moment tensor solutions (Käufl et al., 2014; Melgar et al., 2012; O'Toole et al., 2013) and finite fault slip models (e.g., Miyazaki et al., 2004; Langbein et al., 2005; Melgar et al., 2013b Miyazaki et al., 2004; Langbein et al., 2005; Melgar et al., 2013b).

GNSS displacements, however, are not as precise as integrated seismic velocities or double-integrated accelerations and cannot detect P waves. Thus, GNSS networks require a seismic trigger for detection and hypocenter location. Combining GNSS and collocated

strong-motion data (Nikolaidis et al., 2001; Smyth and Wu, 2007; Emore et al., 2007; Bock et al., 2011) yields unclipped broadband velocity and displacement (seismogeodetic) waveforms that are sensitive to the entire spectrum of ground motions from the Nyquist frequency of the accelerometer data (typically 50-100Hz) to the static coseismic offset, while minimizing baseline errors.

Here we use seismogeodetic networks consisting of collocated GNSS receivers and strong-motion accelerometers to improve local tsunami warnings through rapid estimation of earthquake magnitude. The separation distance between GNSS and strong motion instruments can be as much as 15km as long as the time offset between sensors in considered (Emore et al., 2007). However, we set a maximum separation distance of 5km (Bock et al., 2011; Saunders et al., 2016), and more than 90% of the sensors in this study are within 4km. Ideally, to optimize the combination of the two data types, the instruments should be collocated (also for logistical simplicity). For example, an inexpensive Micro-Electro Mechanical System (MEMS) accelerometer directly attached to the GNSS monument has been deployed at multiple stations in California; the system has been successfully demonstrated in the near field of several M_w4 earthquakes (Saunders et al., 2016; Goldberg and Bock, 2017). We designed a Kalman filter to optimally combine the GNSS displacements and strong motion accelerations (Smyth and Wu, 2007; Bock et al., 2011) to estimate seismogeodetic velocities and displacements. The seismogeodetic velocities are used to detect P wave onset times and estimate the coseismic time window (Chapter 2) over a network of near- to far-field collocated GNSS and accelerometer stations. Using the vertical component of seismogeodetic displacement as an approximate source time function (Kikuchi and Ishida, 1993; Tsuboi et al., 1995), we rapidly estimate the seismic moment and M_w. Our method is based on theory (Aki and Richards, 2002), unlike empirical magnitude scaling relationships such as PGD. Using the seismogeodetic data from nine earthquakes in the $7.2 < M_w < 9.1$ range, we estimate the seismogeodetic moment magnitude, M_{wg}, within 2-3 minutes of earthquake origin time with an accuracy of 0.18 magnitude units for 8 thrust faulting events and 0.32 magnitude units for a single normal faulting event.

3.1.1 Current Methods at Tsunami Warning Center

This study is motivated by our goal of developing an operational seismogeodetic-based warning system for local tsunamis. Although applicable to any tsunami warning center (TWC), we use our work with the National Oceanic and Atmospheric Administration (NOAA)/National Weather Service (NWS)/Pacific Tsunami Warning Center (PTWC), to illustrate our methodology. Rapid magnitude estimation based on seismic data is one component of the current tsunami warning system at PTWC, which performs real-time data reception, earthquake detection, location, and W-phase inversion. It is instructive to describe the current PTWC system at as an example of a real-world operation that can then be useful to other tsunami warning efforts, as well as for earthquake early warning. The PTWC system operates partially within an Earthworm environment (ISTI - Instrumental Software Technologies Inc., Earthworm Central). Automated earthquake picking, association, magnitude estimation and paging (Allen, 1978; Allen, 1982; Evans and Allen, 1983; Johnson et al., 1995; Johnson et al., 1997; Withers et al., 1998) notifies duty scientists of a potential tsunami within 2-5 minutes of the beginning of any earthquake greater than $\sim M_w 5.5$, worldwide. In the Hawaiian Islands, Puerto Rico, and the Virgin Islands, the PTWC duty scientists are paged for earthquakes greater than $\sim M_w 3.5$ within 10-20 seconds of earthquake origin time (Hirshorn, 2007; Hirshorn et al., 2021).

PTWC duty scientists assess the tsunamigenic potential of an earthquake using a variety of magnitude estimation techniques, based on different periods contained in the earthquake source spectrum (Hirshorn et al., 2009; Hirshorn et al., 2021), recorded in regional to teleseismic broadband data. The most accurate estimate of M_w comes from the inversion of the W-phase (Kanamori, 1993) to obtain the WCMT (Kanamori and Rivera, 2008) within $\sim$25 minutes of earthquake origin time. Kanamori and Rivera (2008) showed that the W-phase is useful for regional tsunami warnings by improving the timeliness from approximately 25 to 5 minutes after earthquake origin time. Regional implementations are operating in Japan, Mexico, Australia, Taiwan, China, and Chile. In Chile, the W-Phase method has been running automatically in real-

time for the Centro Sismológico Nacional (CSN) since 2011 for regional distances, providing a WCMT and M_w within 5-6 minutes of earthquake origin time (Riquelme et al., 2016; Riquelme et al., 2018). Although not yet implemented in real-time operations, PTWC is testing a regional WCMT modification, which will report M_w and the moment tensor within $\sim$15 minutes. See Hirshorn et al. (2009) and Hirshorn et al., 2021 for a review of PTWC source characterization methods.

The broadband P wave moment magnitude, M_{wp} (Tsuboi et al., 1995; Tsuboi et al., 1999; Whitmore et al., 2002) provides PTWC with initial estimate of M_w. The M_{wp} method relies on the first P waves, typically providing accurate estimates of M_w within about 2-5 minutes of rupture initiation. However, M_{wp} estimates of M_w have three important caveats. First, for very large ($M_w > 8.0$) earthquakes, M_{wp} may saturate when based on data from seismic sensors with insufficient long period (e.g., $<$ 350 seconds) sensitivity. Second, for complex earthquakes with several source time function peaks that are well separated in time, M_{wp} may underestimate M_w. Third, and perhaps the most challenging for a tsunami warning system, is the identification of "tsunami" or "slow" earthquakes (Kanamori, 1972). M_{wp} may underestimate the magnitude of these events because of their relatively slow moment release over a longer rupture time. The seismogeodetic magnitude estimate described here (M_{wg}) can potentially address these caveats, enabling PTWC to issue local tsunami warnings with accurate magnitude estimates and within 2-3 minutes of earthquake origin time.

PTWC issues its first tsunami threat message for any shallow ($<$ 100km) undersea or nearshore earthquake in or near the vicinity of the Pacific basin with a magnitude greater than M_w7.0. If the magnitude is in the 7.1-7.5 range, the message will indicate a possible tsunami threat to coasts located within 300km of the epicenter. If the magnitude is in the 7.6 to 7.8 range, a message will indicate a possible tsunami threat to coasts located within 1000 km of the epicenter. And finally, if the magnitude is greater than M_w7.9, the message will indicate a possible tsunami threat to coasts located within a 3-hour tsunami travel time from the earthquake's epicenter. Different warning criteria have been established for Hawaii ($M_w > 6.9$), Guam, the Virgin Islands,

and Puerto Rico ($M_w > 7.1$). The criteria for Samoa depend on location and magnitude.

3.2 Theory of Seismogeodetic Magnitude M_{wg}

Aki and Richards (2002) expressed the earthquake displacement field $u(\overrightarrow{x},t)$ generated by a double-couple point source in a homogeneous elastic medium as a sum of near (N), intermediate (IP and IS), and far (FP and FS) field P and S wave terms,

$$\begin{aligned} u(\overrightarrow{x},t) = & \frac{A^N}{4\pi\rho r^4}\int_{r/\alpha}^{r/\beta} \tau M_0(t-\tau)\, d\tau \\ & + \frac{A^{IP}}{4\pi\rho\alpha^2 r^2} M_0(t-\frac{r}{\alpha}) + \frac{A^{IS}}{4\pi\rho\beta^2 r^2} M_0(t-\frac{r}{\beta}) \\ & + \frac{A^{FP}}{4\pi\rho\alpha^3 r} \dot{M}_0(t-\frac{r}{\alpha}) + \frac{A^{FS}}{4\pi\rho\beta^3 r} \dot{M}_0(t-\frac{r}{\beta}) \end{aligned} \tag{3.1}$$

where r is the distance between source and receiver, t is time, the A^i terms represent the radiation patterns, and ρ, α, and β are the density, P wave, and S wave velocities, respectively. $M_0(t)$ is the time history of the seismic moment, and its derivative, $\dot{M}_0(t)$, is the moment rate.

Since the P wave is most pronounced in the vertical direction, we follow Kikuchi and Ishida (1993) and Tsuboi et al. (1995) and use the vertical component of seismogeodetic displacement (as justified in Chapter 3.3), $u_z(\overrightarrow{x},t)$, limited to the far-field P wave term, as an approximate moment rate function

$$u_z(\overrightarrow{x},t) = \frac{A^{FP}}{4\pi\rho\alpha^3 r}\dot{M}_0(t-\frac{r}{\alpha}) \tag{3.2}$$

where A^{FP} represents the radiation pattern generated by a double-couple source.

We estimate the seismic moment by integrating $u_z(\overrightarrow{x},t)$ in Equation 3.3. Because the real Earth is heterogenous, $u_z(\overrightarrow{x},t)$ contains path (attenuation and geometrical spreading) and receiver (free surface response at the station) effects. We apply approximations to account for these effects following Tsuboi et al. (1995), and assume values of 0.8 for anelastic attenuation,

$1.2r$ for geometrical spreading, and 1.5 for the free surface effect at the receiver. We integrate $u_z(\overrightarrow{x},t)$ to obtain the moment history, $M_0(t)$, at each station by

$$M_0(t) = \frac{4\pi\rho\alpha^3 r}{A^{FP}} \int u_z(\overrightarrow{x},t)\, dt \tag{3.3}$$

Since we are using seismogeodetic displacement, instead of seismic velocity, we avoid doubly integrating velocities to estimate $M_0(t)$, thereby reducing baseline errors (Melgar et al., 2013a). Assuming that the maximum absolute value of the moment function in Equation 3.3 recorded at each station is the actual seismic moment of the earthquake, M_0, we follow Tsuboi et al. (1995) by estimating

$$M_0 \cong 4\pi\rho\alpha^3 r \quad Max\left|\int u_z(\overrightarrow{x},t)\, dt\right| \tag{3.4}$$

Tsuboi et al. (1995) showed that a combination of multiple records will give a good estimate of M_0 without correcting for A^{FP}, assuming a reasonable azimuthal coverage. Therefore, in this study we do not correct for this term. For the other parameters in Equation 3.6, we choose representative values for the uppermost mantle of $\rho = 3400\frac{Kg}{m^3}$ and $\alpha = 7900\frac{m}{s}$ (Tsuboi et al., 1995). As indicated earlier, we determine the coseismic time window for the integration in Equation 3.6 at each station individually using the seismogeodetic velocity (Chapter 2.2, Equation 2.1). Following Kanamori (1977) relationship between the seismic moment (M_0) and moment magnitude (M_w), we compute the seismogeodetic moment magnitude at each station by

$$M_{wg} = \frac{2}{3}(\log_{10} M_0 - 9.1) \tag{3.5}$$

which we refer to as M_{wg} to distinguish it from a magnitude estimate derived solely from seismic data.

3.1 shows an example of a vertical seismogeodetic displacement time series and the derived moment function for collocated seismic and GNSS stations recorded during the 2011

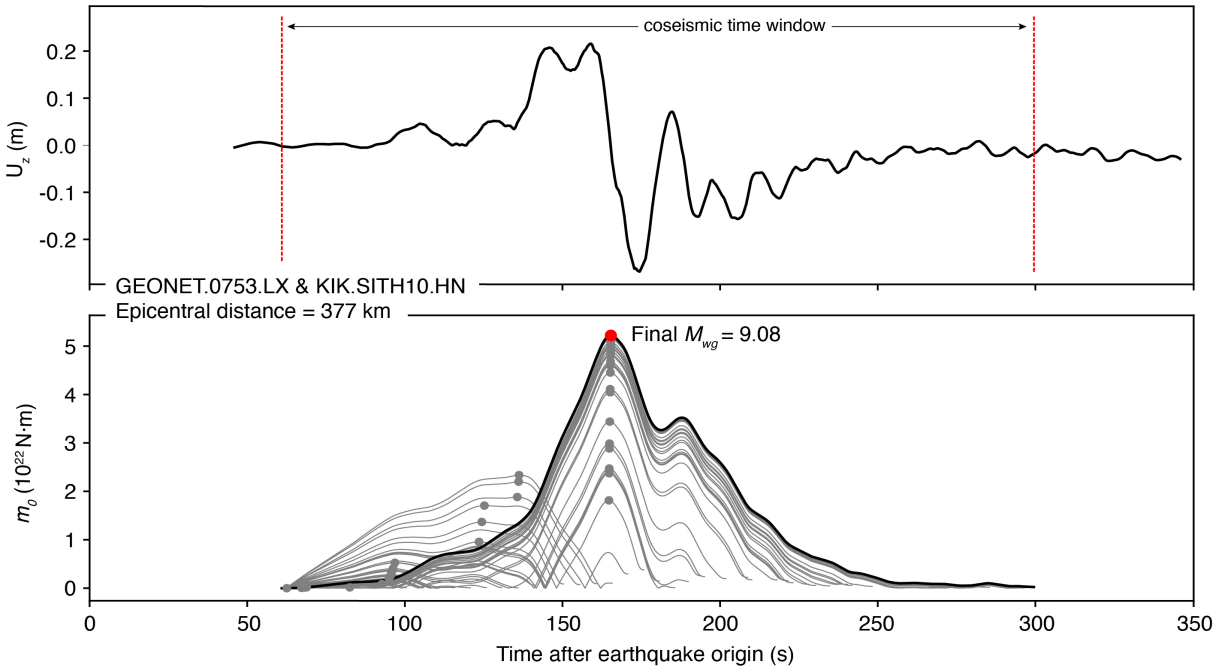

Figure 3.1. Example of vertical seismogeodetic displacement (top), and the derived moment function within the evolving coseismic window (bottom) for a collocated station during the 2011 M_w9.1 Tohoku-oki, Japan earthquake. The final coseismic time window is denoted by the vertical lines (top), and its derived final moment function in black (bottom) with the maximum value as a red point. The reported final seismogeodetic moment magnitude estimate for this station is based on Equations 3.6 and 3.5.

M_w9.1 Tohoku-oki, Japan earthquake. The final coseismic time window (top panel) is denoted by the vertical lines. The time of detected peaks in the moment function (bottom panel, grey and red circles) together with the end time of the coseismic window indicate that we can derive/calculate a reliable magnitude estimate within ∼180 seconds (before the end of the rupture) and a more accurate final estimate within ∼300 seconds after origin time. Our estimates of the seismic moment are based directly on the maximum value of integrated displacement. Thus, regression against other source parameters such as peak-ground-displacement (PGD) versus distance (Crowell et al., 2013), empirically-based on the historical record, is not required.

3.3 Real-time Simulations of M_{wg} for Historical Earthquakes

We gathered collocated GNSS and accelerometer data recorded during nine earthquakes in the magnitude range $7.2 < M_w < 9.1$ that occurred in the Pacific basin offshore Mexico, Chile, Japan, Alaska, and Hawaii (Table 3.1). Strong-motion and GNSS data for Chile were obtained from the Centro Sismológico Nacional (CSN) (Barrientos et al., 2018; Baez et al., 2018). Data for Japan were obtained from the K-net and KiK-net seismic networks (Aoi et al., 2011) operated by the National Research Institute for Earth Science and Disaster Resilience (NIED), and the GEONET GNSS network (Sagiya et al., 2000; Sagiya, 2004). Seismic and GNSS data for Mexico were obtained from both TLALOCNet and the Servicio Sismológico Nacional (SSN) (Cabral-Cano et al., 2018). Alaska and Hawaii accelerograms were obtained from the IRIS archive and GNSS data from continuous networks in North America (Murray et al., 2019).

For the purpose of demonstration, we post-processed GNSS phase and pseudorange data, epoch by epoch, to estimate displacements using precise point positioning (PPP) without ambiguity resolution (Ge et al., 2008; Geng et al., 2012). For the purpose of demonstration, we used the International GNSS Service (IGS) final orbits and Bernese satellite clock estimates (Bernese GNSS Software). Similarly precise results can be obtained in real time using in-receiver or server-based PPP processing. The system that we are testing with PTWC uses server-based PPP solutions streamed by UNAVCO's Geodetic Facility for the Advancement of Geoscience (GAGE) facility from more than 1000 Network of the Americas (NOTA) stations (Hodgkinson et al., 2020; Mattioli et al., 2020; Dittmann et al., 2022). The GNSS and accelerometer data were then combined using a seismogeodetic Kalman filter with an acceleration multiplier of 10, as described by Bock et al. (2011) and Saunders et al. (2016), resulting in 100-200Hz displacement and velocity waveforms (Figure 3.2).

For calculating earthquake magnitude before the onset of postseismic deformation, it is important to compute the coseismic time window on a station-by-station basis. We adopt

Table 3.1. Earthquakes used in this study.

Name / Region	M_w[1]	Fault Mechanism	Origin Time (UTC)[2]	Longitude (° E)	Latitude (° N)	Depth (km)
Tokachi-oki, Japan	8.3	Reverse	2003-09-25 19:50:07	144.079	41.780	42.0
Maule, Chile	8.8	Reverse	2010-02-27 06:34:11	-72.898	-36.122	22.9
Tohoku-oki, Japan	9.1	Reverse	2011-03-11 05:46:24	142.861	38.104	29.0
Iquique, Chile	8.1	Reverse	2014-04-01 23:46:47	-70.769	-19.610	25.0
Illapel, Chile	8.3	Reverse	2015-09-16 22:54:32	-71.674	-31.573	22.4
Chiapas, Mexico	8.2	Normal	2017-09-08 04:49:19	-93.899	15.022	47.4
Kilauea, Hawaii	6.9[3]	Reverse	2018-05-04 22:32:54	-155.000	19.318	5.8
Simeonof, Alaska	7.8	Reverse	2020-07-22 06:12:44	-158.522	55.030	28.0
Chignic, Alaska	8.2	Reverse	2021-07-29 06:15:49	-157.888	55.364	35.0

[1] Magnitudes are from the Global Centroid Moment Tensor (GCMT) catalog.

[2] Earthquake origin time and hypocenter location are from the National Research Institute for Earth Science and Disaster Resilience (NIED) for Japan, and from the United States Geological Survey (USGS) for Chile, Mexico, Hawaii, and Alaska earthquakes.

[3] Comprehensive analysis by Bai et al. (2018) and Lay et al. (2018) resulted in a magnitude of M_w7.2 for this earthquake.

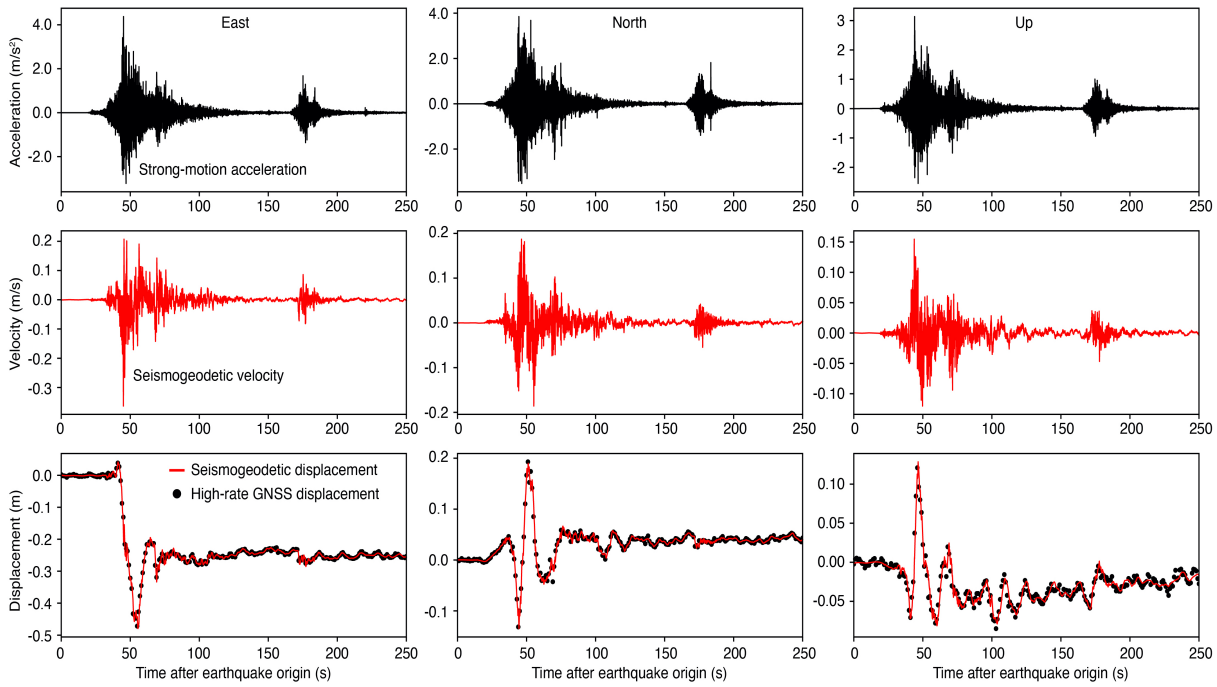

Figure 3.2. Example of broadband seismogeodetic velocities and displacements recorded during the 2014 M_w8.2 Iquique, Chile earthquake at sites located $\sim$104km from the hypocenter. The Kalman filter input of strong-motion acceleration (station T08A, top) and high-rate (1Hz) GNSS displacement (station IQQE, bottom) are in black, while the output of unclipped broadband velocity (middle) and broadband displacement (bottom) are in red.

the formulation described in Chapter 2.2; using the seismogeodetic velocity (rather than GNSS displacements which are insensitive to P wave arrivals) to determine the coseismic time window. We used an STA/LTA picker (Allen, 1982) to determine the first P wave arrival as the start of the window, and estimate the end time by integrating the normalized velocity squared within a 5-second moving window in time until its 99% point reaches convergence. This process is performed individually for each station, thereby estimating the progression of the rupture process through the network of sensors. The coseismic window length will vary with epicentral distance, and possibly due to path and site effects. Other source parameters, such as peak-ground-displacements and static offsets can then be estimated from the displacement waveforms. In this study, we use the coseismic time window to integrate the vertical component of the seismogeodetic displacements.

We use vertical displacement $u_z(\overrightarrow{x},t)$ from nine dip-slip earthquakes (8 thrust faulting and 1 normal faulting) in the $7.2 < M_w < 9.1$ range to estimate seismic moment and seismogeodetic moment magnitude, M_{wg}, for each earthquake. Once the P wave is detected, we calculate the magnitude at 5-second intervals, for each station in parallel using Equations 3.6 and 3.5. The final magnitude for a given station is reported at the end time of its coseismic window. In Figure 3.3, we present the magnitude estimate evolution over time after rupture initiation for each earthquake, with individual station estimates shown as grey curves and the event medians (more robust than means) every 10-seconds shown as red scatter points with error bars estimated as ± 1 interquartile-range (IQR) of all station estimates. The IQR is defined as the range of the middle 50% of the data, the difference between the 75^{th} and 25^{th} percentiles. When a data sample is drawn from a normal distribution, its mean very nearly equals its median and its standard deviation equals about three quarters of the IQR.

The estimated M_{wg} magnitudes are within ± 0.15 magnitude units of the GCMT M_w values (Dziewonski et al., 1981; Ekström et al., 2012) and within their IQR uncertainties for the 7 shallow thrust events of $M_w > 7.8$. We estimate $M_{wg}8.52$ compared to the GCMT of $M_w8.2$ for the 2017 Chiapas event. Note that this is the only event with a normal fault mechanism

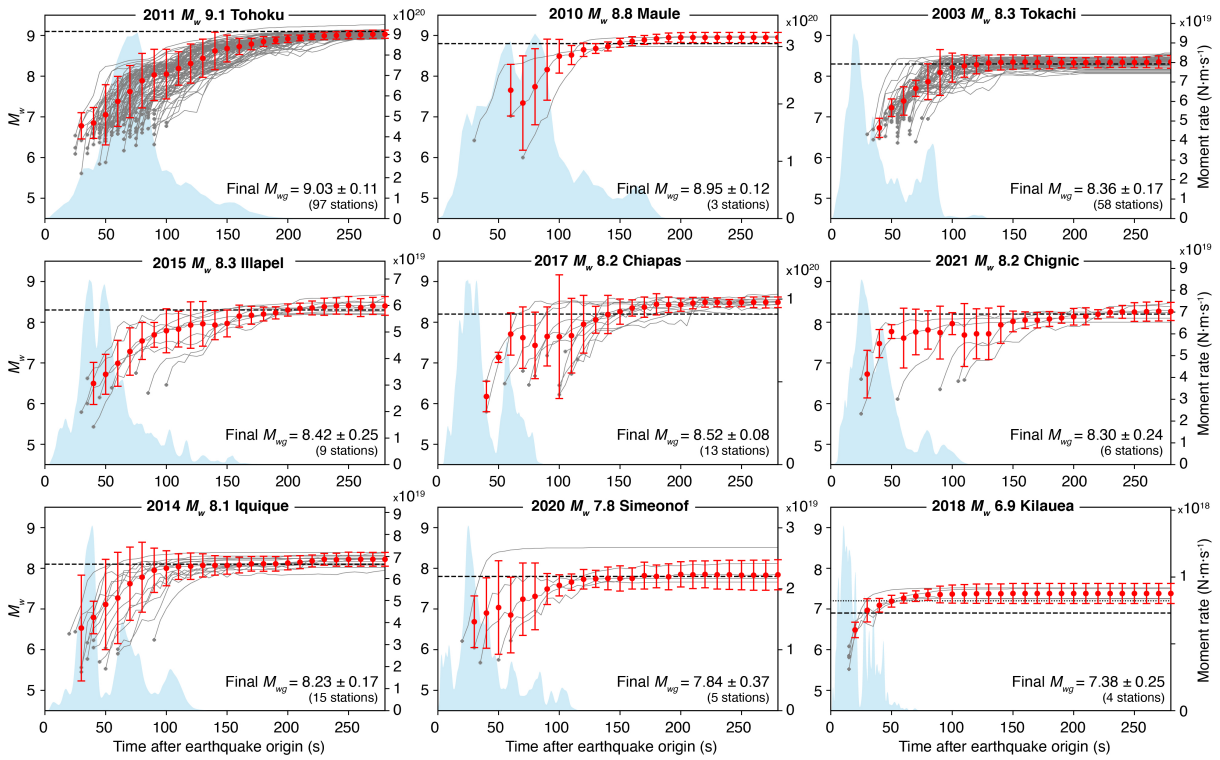

Figure 3.3. Time evolution of our magnitude estimates for nine earthquakes used in this study. Grey curves denote individual stations, red points are event medians with ± 1 interquartile-range (IQR). Moment rate functions from the USGS are in light blue. The GCMT magnitudes are denoted by black dashed horizontal lines. For the 2018 Kilauea event, we also include a black dotted line indicating the M_w7.2 estimate of Bai et al. (2018) and Lay et al. (2018).

while all the others are thrust events. The closest station ($\sim$70km) recording during the 2020 M_w7.8 Simeonof earthquake overestimates the magnitude with M_{wg}8.51 and is clearly an outlier. This station lies in close proximity to the trench and experienced $\sim$33cm of coseismic uplift. Therefore, our far-field assumption (Equation 3.2) may not be valid in this case or the discrepancy may be due to directivity or site effects. Nevertheless, the event median of M_{wg}7.84 matches the final published magnitude. Our estimate of M_{wg}7.38 for the 2018 Kilauea, Hawaii earthquake is significantly larger than the GCMT value of M_w6.9. However, because of the inverse relationship between dip and seismic moment for shallow earthquakes, the magnitude of the 2018 Kilauea event is likely closer to M_w7.2 (Bai et al., 2018; Liu et al., 2018; Lay et al., 2018), in closer agreement with our results. In addition, the low rupture velocity ($\sim 1\frac{km}{s}$), long rupture duration ($\sim$40s), and low moment-scaled radiated energy, imply frictional properties similar to those in the shallow portions of subduction zones where tsunami earthquakes occur (Liu et al., 2018). If that is the case here, our results (albeit from a sample of a single event) suggest that we can get an accurate magnitude estimate for tsunami earthquakes.

To justify our use of only the far field vertical P wave component (FP) of the earthquake displacement field $u(\overrightarrow{x},t)$, we follow Madariaga et al. (2019) and express the near-field (first) term (N) of Equation 3.1 in a slightly different form,

$$\frac{A^N}{4\pi\rho\beta^2 r^2}\int_{\beta/\alpha}^{1}\tau M_0(\frac{\beta t}{r}-\tau)\,d\tau \tag{3.6}$$

and show that the near-field displacement term falls off as r^{-2}. Since the intermediate-field displacement terms also fall off as r^{-2}, the near- and intermediate-field (NF and IF) terms are not separable by studying their radiation; they combine to produce a coseismic static offset which attenuates at r^{-2} compared to the r^{-1} decay of the (dynamic) far-field terms (Nikolaidis et al., 2001; Madariaga et al., 2019). By estimating the permanent coseismic displacement offset ($NF+IF$ terms) and subtracting it from the vertical peak-ground-displacement ($NF+IF+FF$ terms), we determine the displacement due to the (dynamic) far-field (FF) term only. For the

largest earthquake in our dataset (2011 M_w9.1 Tohoku-oki), the far-field terms dominate the vertical component of displacement beyond $r \sim$175km epicentral distance (Figure 3.4) which, for this bilaterally rupturing event, corresponds to $\frac{1}{2}$ of its rupture length of $\sim$350km (Ye et al., 2016; Hayes, 2017). This result justifies the use of the far-field P wave term of Equation 3.1. Also, for steeper incident rays at the receiving sites, the longitudinal (radial) energy, mostly P with very little vertically polarized S waves, would dominate on the vertical components (with very little, if any, horizontally polarized S waves). This justifies using the P wave term recorded by the vertical component.

Because we integrate the vertical component of displacement over the entire coseismic window, we are able to measure the largest moment release even if it occurs after an earlier but smaller peak. This provides accurate M_{wg} estimates for complex earthquakes as well as for tsunami earthquakes where peak moment release may occur late enough in the rupture process to indicate a long rupture duration. Therefore, the time of the maximum peak as well as its amplitude should allow identification of tsunami earthquakes.

We neglected the radiation pattern term A^{FP} term in Equation 3.6 based on Tsuboi et al. (1995), who showed that a combination of multiple records will give a good estimate of M_0, assuming a reasonable azimuthal coverage. We assumed a value of 1 for the A^{FP} term in Equations 3.2 and 3.3. Assuming an extreme case of A^{FP} that is equal to 0.1, this term will lead to a $\frac{2}{3}$ (0.67) of a magnitude unit difference in our M_{wg} estimate for a particular station resulting in an increased magnitude. However, we do not expect this term to vary significantly from 1 within on-shore stations during a thrust faulting event. In fact, Tsuboi et al. (1995) showed that the averaged radiation pattern over the entire focal sphere is $\overline{A^{FP}} \cong \sqrt{\frac{4}{15}}$, which is, based on Equations 3.3 and 3.5, equivalent to 0.2 magnitude units. Due to the nature of subduction zones and the land-based GNSS and seismic instrumentation, most earthquakes in our data set are associated with azimuthal gaps larger than 180 degrees (Goldberg and Bock, 2017). This is particularly of concern for the Kilauea, Iquique, and Chiapas earthquakes. Therefore, we explore the effect of the spatial distribution of the stations on the estimated magnitude (Figure 3.5) and

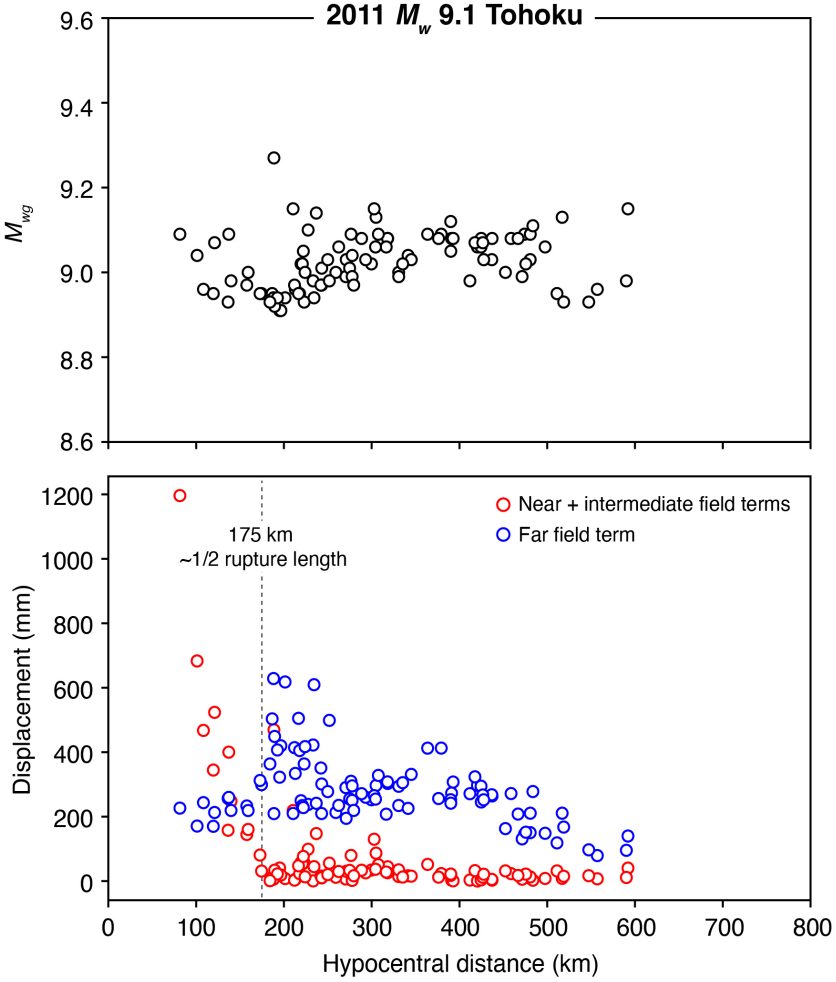

Figure 3.4. Distinguishing the contribution of far-field vertical displacements in Equation 3.1 for the 2011 M_w9.1 Tohoku-oki earthquake. Top: records of estimated M_{wg} per station as a function of epicentral distance. Bottom: absolute value of permanent vertical coseismic offsets (near- and intermediate-field terms) as red points, and the difference between vertical peak displacements and static offsets (far-field term) as blue points, as a function of epicentral distance. Note that the FF P waves dominate the vertical component of displacement beyond $\sim$175km epicentral distance.

find that M_{wg} provides precise and accurate magnitude estimates for tsunamigenic earthquakes even with poor azimuthal or sparse station coverage (e.g., the 3 stations for the 2010 M_w8.8 Maule earthquake).

3.4 Discussion and Comparison with other GNSS-based Methods

We compare our M_{wg} approach with two additional magnitude determination methods that rely on high-rate GNSS displacements; the empirical PGD scaling law (M_{pgd}), and W-phase inversion from regional GNSS (M_{ww}). For the M_{pgd} calculation and regression, we use all available GNSS stations (instead of collocated only) and follow the procedure described in Ruhl et al. (2019). We set a minimum PGD value of 3cm, a maximum hypocentral distance of 1000km, and signal-to-noise ratio (SNR) of 3 and above for a station to be included in the regression. The PGD versus hypocentral distance regressions are shown in Figure 3.6.

The GNSS-derived W-phase results of M_{ww} are taken from Riquelme et al. (2016) and only available for the 2010 M_w8.8 Maule, 2011 M_w9.1 Tohoku, 2014 M_w8.1 Iquique, and 2015 M_w8.3 Illapel earthquakes. We compare final results of the three methods in Table 3.2, and a timeline for the first 5 minutes after earthquake origin time in Figure 3.7. The uncertainty for M_{wg} is defined as ± 1 IQR, similar to error bars on Figure 3.3, while the uncertainty for M_{pgd} is defined as the root mean square error of the linear regression. No M_{ww} uncertainty was reported by Riquelme et al. (2016). Six of the nine events are earthquakes used by Ruhl et al. (2019) in their PGD regressions. The M_{pgd} magnitudes for two of the "new" earthquakes (i.e., not included in the published analysis), 2020 M_w7.8 Simeonof and 2021 M_w8.2 Chignic, are underestimated compared to the GCMT and M_{wg} magnitudes, which match within the uncertainties of M_{wg}. For the 2018 Kilauea earthquake, M_{pgd} (6.67 ± 0.15) is closer to M_w6.9 while M_{wg} (7.38 ± 0.25) is significantly overestimated. However, as indicated earlier, our results are consistent with the analysis by Bai et al. (2018) and Lay et al. (2018) who estimate

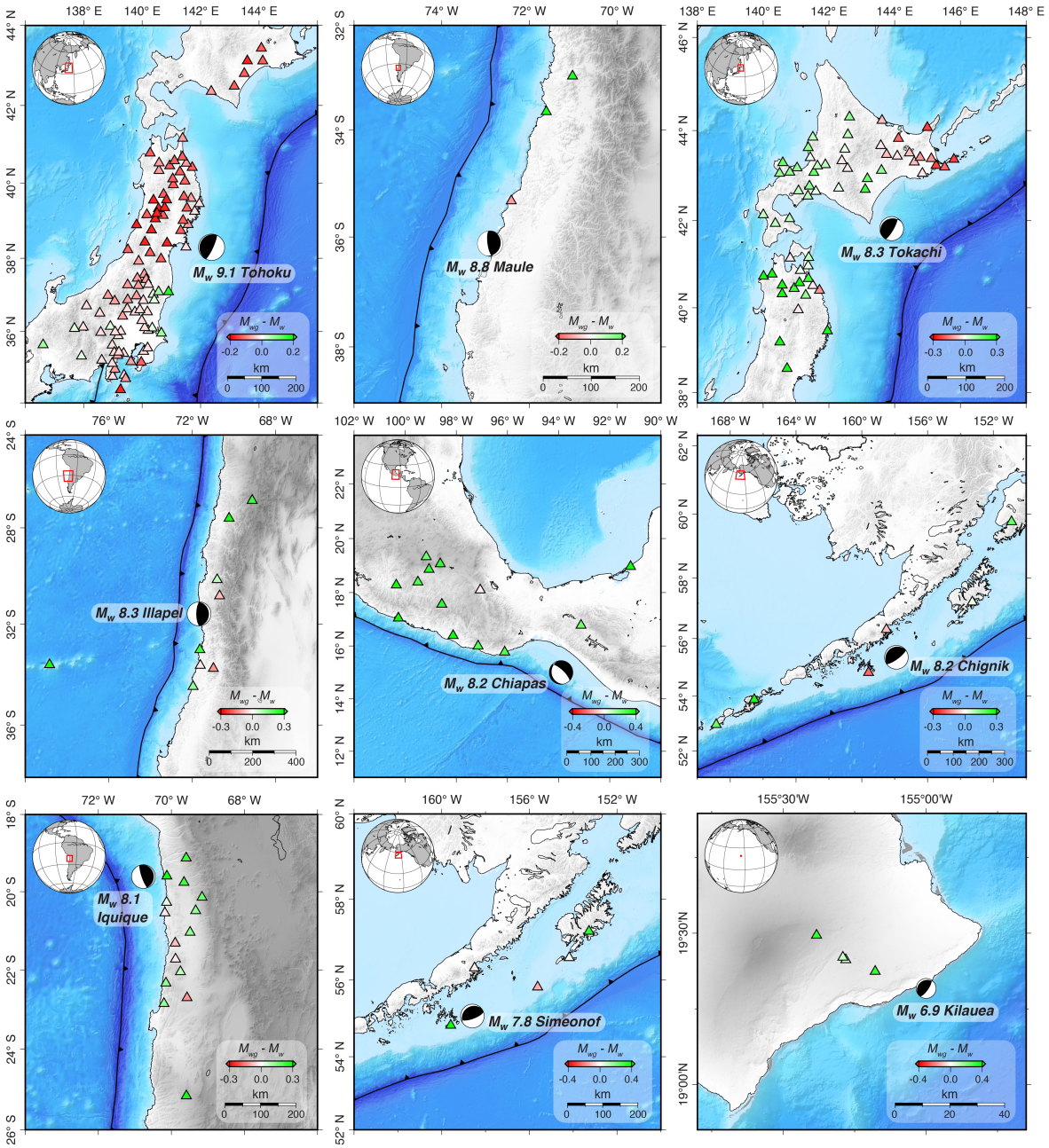

Figure 3.5. Spatial distribution of station by station M_{wg} estimates for all earthquakes included in our study. Green colors indicate overestimates, while red colors indicate underestimates.

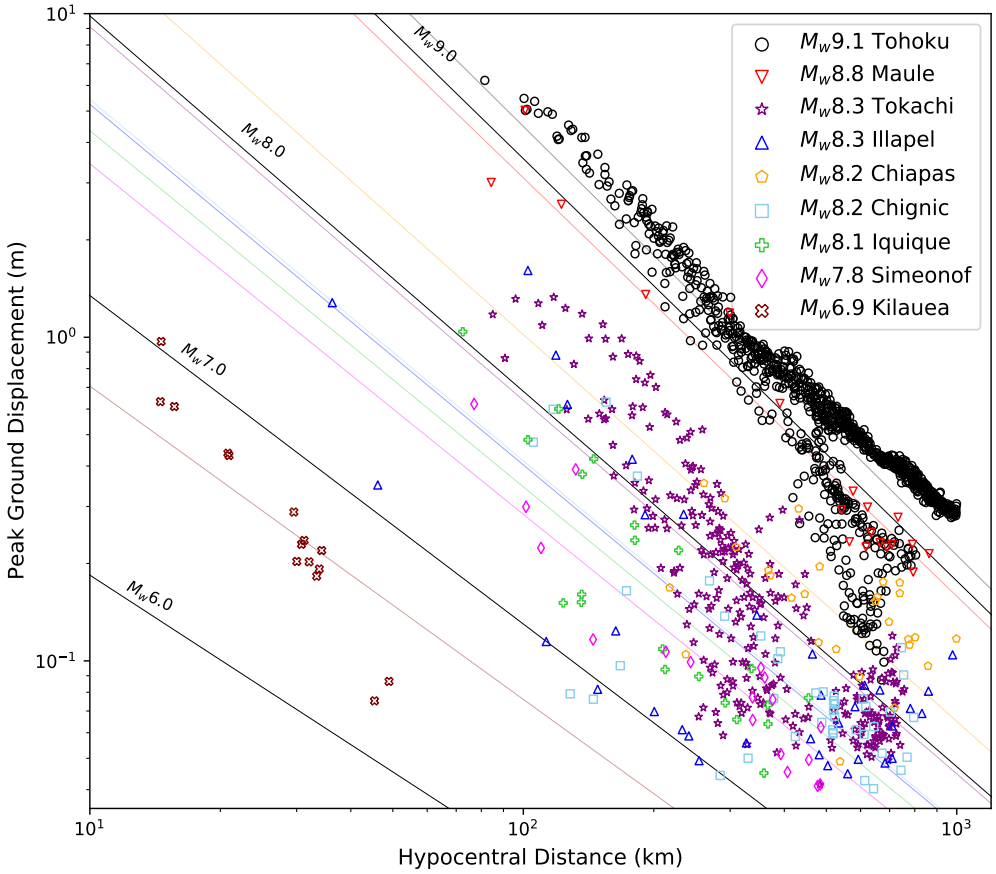

Figure 3.6. Peak-ground-displacement (PGD) versus hypocentral distance for each earthquake in our dataset. The final estimates and regression errors are reported in the main text (Table 3.2). Results are obtained using all available high-rate ($\geq$1Hz) GNSS stations, following the criteria and coefficients of Ruhl et al. (2019).

a magnitude of M_w7.2 for the 2018 Kilauea event. Furthermore, using the Ruhl et al. (2019) regression coefficients results in a significant underestimate of the 2014 M_w8.1 Iquique and 2015 M_w8.3 Illapel earthquake magnitudes (Table 3.2). The M_{wg} estimates are more accurate than M_{pgd} except for the single normal event in our data set, the 2017 Chiapas earthquake, where M_{wg} is a significant overestimate. Therefore, even though PGD-based magnitude estimates are timelier (Figure 3.7) and despite our study being limited to nine earthquakes, our theory-based seismogeodetic M_{wg} results are accurate and valuable estimates of M_w. Although beyond the scope of this study, we speculate that the empirically-based PGD method insufficiently accounts for the full range of source, site and/or path effects. GNSS-derived W-phase final (within 4-5 minutes) results of M_{ww} are comparable to our M_{wg} estimates for the four earthquakes reported by Riquelme et al. (2016). W-phase inversion is stable within 4-5 minutes after rupture initiation for most cases. Using the M_{wg} approach, initial estimates of M_w7+ are available within 1 minute and could be beneficial for early tsunami threat messages. It is important to note that M_{ww} inversion includes earthquake focal mechanism, which is a key component for the assessment of tsunamigenic potential.

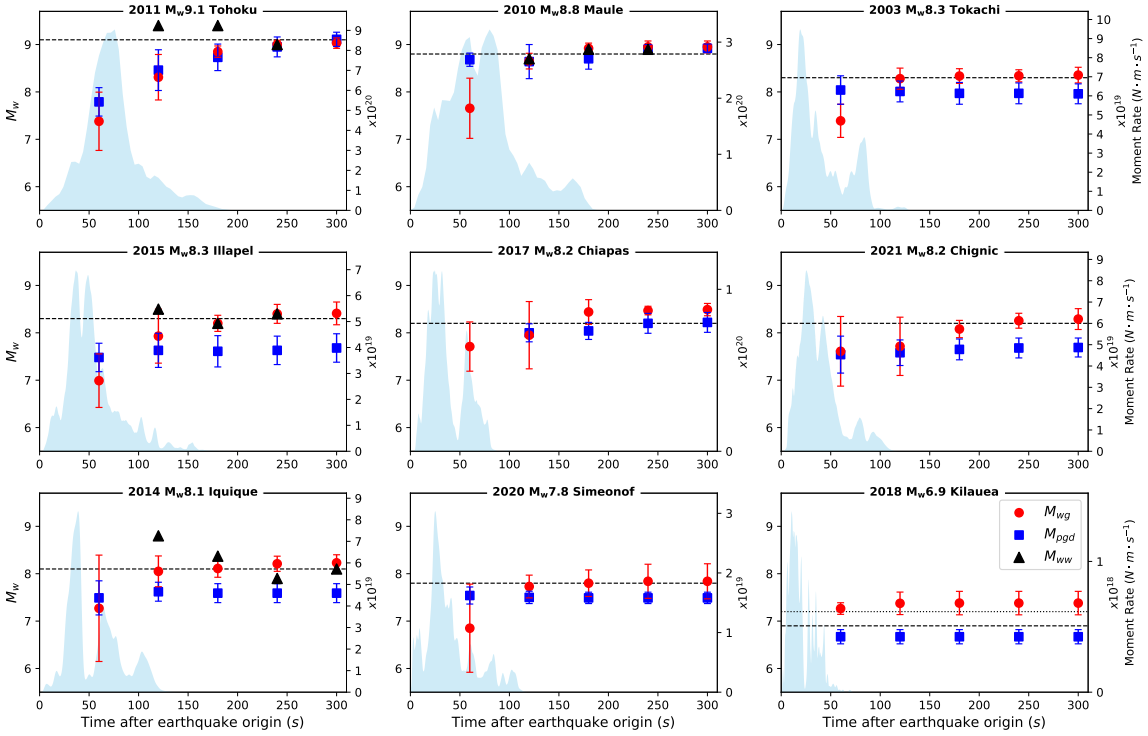

Figure 3.7. Timeline comparison between GNSS-based M_w estimates, for the first 5 minutes after earthquake origin time. Red points are seismogeodetic event medians M_{wg} (this study) with one IQR error bars, blue squares are peak ground displacement M_{pgd} (following Ruhl et al., 2019) with one root-mean-square error bars, and black triangles are GNSS W-phase M_{ww} (taken from Riquelme et al., 2016). GCMT magnitudes are denoted by black dashed horizontal lines. For the 2018 Kilauea event, we also include a black dotted line indicating the M_w7.2 estimate of Bai et al. (2018) and Lay et al. (2018). The comparison with M_{ww} is limited to the four earthquakes found in Riquelme et al. (2016), with no available error bars, that overlap with our earthquake data set.

Table 3.2. Comparison between GNSS-based M_w estimates. M_{wg} (this study), M_{pgd} (following Ruhl et al., 2019) and M_{ww} (taken from Riquelme et al., 2016).

Name / Region	M_w	Estimate M_{wg}	#Stations M_{wg}	Estimate M_{pgd}	#Stations M_{pgd}	Estimate M_{ww}	#Stations M_{ww}
Tokachi-oki, Japan	8.3	8.36 ± 0.17	58	7.96 ± 0.20	307	-	-
Maule, Chile	8.8	8.95 ± 0.12	3	8.92 ± 0.09	19	8.90	12
Tohoku-oki, Japan	9.1	9.03 ± 0.11	97	9.14 ± 0.15	916	9.00	375
Iquique, Chile	8.1	8.23 ± 0.17	15	7.59 ± 0.20	21	8.10	9
Illapel, Chile	8.3	8.42 ± 0.25	9	7.68 ± 0.30	35	8.40	15
Chiapas, Mexico	8.2	8.52 ± 0.08	13	8.24 ± 0.21	27	-	-
Kilauea, Hawaii	6.9*	7.38 ± 0.25	4	6.68 ± 0.15	15	-	-
Simeonof, Alaska	7.8	7.84 ± 0.37	5	7.47 ± 0.12	18	-	-
Chignic, Alaska	8.2	8.30 ± 0.24	6	7.70 ± 0.21	43	-	-

* Comprehensive analysis by Bai et al. (2018) and Lay et al. (2018) resulted in a magnitude of M_w7.2 for this earthquake.

Acknowledgements

Chapter 3, in full, is a reformatted version of material as it appears in Journal of Geophysical Research - Solid Earth: Golriz, D., Hirshorn, B., Bock, Y., Weinstein, S., Weiss, J. R. (2022). "Real-Time Seismogeodetic Earthquake Magnitude Estimates for Local Tsunami Warnings". Journal of Geophysical Research: Solid Earth, doi:10.1029/2022JB025555. The dissertation author was the primary investigator and author of this material.

Chapter 4

Interseismic Deformation Along the Dead Sea Fault Region Revealed by InSAR and GNSS Measurements

4.1 The Dead Sea Fault – Tectonic Setting

The Dead Sea Fault (DSF) is a north-south transform plate boundary between the Sinai subplate and the Arabian plate. Its length exceeds 1000km, from the Red Sea spreading center in the south to the Zagros-Taurus convergence zone in the north. The relative left lateral motion across the DSF has been estimated using geodetic data to be 3-7mm/year, with varying slip rates on different segments of the fault. Generally, long term geological estimates are larger than seismic and geodetic slip rates and are up to 10 mm/year (Wdowinski et al., 2004). It has been suggested that several segments of the DSF experience shallow creep, such as the Sedom and Amazyahu faults at the southern edge of the Dead Sea (Hamiel and Piatibratova, 2019) and the northern section of the Jordan Valley, just south of the Sea of Galilee (Hamiel et al., 2016). Other sections are found to be locked; the Arava Valley with a locking depth of $\sim$20km (Hamiel et al., 2018a), the Jericho Valley with a locking depth of $\sim$6km (Hamiel et al., 2018b), and the Jordan Gorge section with a locking depth of $\sim$10km (Hamiel et al., 2016). These varying slip rates and locking depths along the DSF system raise the question of seismic hazard for the cities that lie in the vicinity of the fault such as Jerusalem and Amman, with populations of over 5 million

people (Figure 4.1).

The strong earthquake potential of the Dead Sea Fault is documented by paleoseismicity (Marco et al., 1996), radiocarbon dating (Migowski et al., 2004), and historical records (Marco et al., 2003). The archeological site of Tell Ateret tells us a remarkable story about the earthquake history of the Northern segment of the DSF, tens of kilometers from the Sea of Galilee and on the active fault. Ellenblum et al. (2015) excavated this site and correlated old structures with historical data. They found alternating earthquake slip that shifted old constructions, dating back to the Iron age. Since the 11^{th} century, at least 4 earthquakes of magnitude $6.3 < M_w < 7.1$ struck the area of Tell Ateret with over 8 meters of total accumulated slip. The 1927 M_w6.3 earthquake occurred near the city of Jericho. The exact location of the event is controversial but generally assumed to be North of the Dead Sea and just 30-40km East of Jerusalem. The earthquake resulted in considerable casualties and damage in Jericho and surrounding towns. Estimation of casualties ranges between 250-500 deaths, and 400-700 injuries (Zohar and Marco, 2012). The most recent damaging earthquake along the DSF occurred in November 1995 at the Gulf of Aqaba and near the town of Nuweiba, Egypt, with a magnitude M_w7.2. With very little GNSS data for the period spanning the earthquake origin time, Baer et al. (1999) examined the surface deformation associated with this event using four SAR images by the ERS-1 and ERS-2 satellites. They used different static fault models to determine 1.4–3 meters of averaged slip.

Since 2017, the Israeli seismic network has been undergoing significant upgrades with added stations and data centers (Kurzon et al., 2020). These are part of the implementation of a national Earthquake Early Warning system named *TRUAA*. Nof and Kurzon (2021) presented an overview of the system and initial performance during the deployment phase. In a more recent study, Nof et al. (2021) estimated the performance of the system during the initial operational phase over 8 months. For earthquake magnitude determination, Ground Motion Prediction Equations (GMPEs) were adopted from Lior and Ziv (2018). They found alert delays that are as low as 3 seconds, and source parameters estimation is within the accepted range of uncertainty; mean magnitude error of 0.38, median location error of $\sim$5km, and median time errors of 0.8

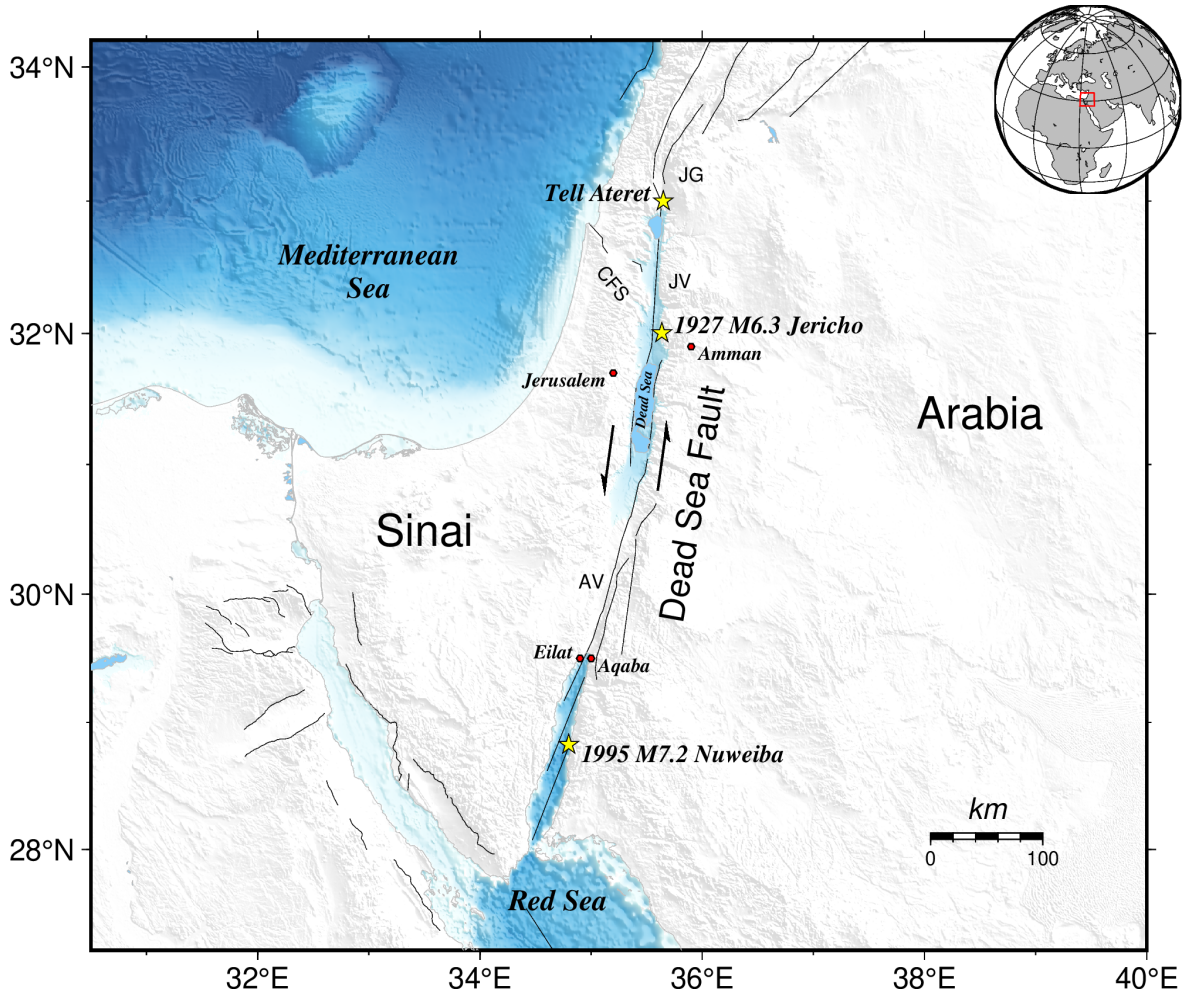

Figure 4.1. Our study area of the Dead Sea Fault. Black arrows show the relative plate motion between the Arabia plate and Sinai subplate. Significant earthquakes from the last century and the archeological site of Tell Ateret are denoted by yellow stars. Major cities are denoted by red hexagons. AV - Arava Valley, JV - Jordan Valley, JG - Jordan Gorge, CFS - Carmel Fault System. Black lines are tectonic faults from GEM Global Active Faults Database (Styron and Pagani, 2020).

seconds. The dataset used in this study consists of 41 earthquakes in the range of $2.1 < M_w < 3.7$, and lack large magnitude events for more complete statistics. The system is now operational with alerts to limited areas for $4.2 < M_w < 6.0$ events, and a country-wide alert for $M_w \geq 6.0$ earthquakes.

Both the DSF and the San Andreas Fault (SAF) are continental transform plate boundaries with a similar faulting style that deviates from a simple shear and has some component of shortening at local scale (Weber et al., 2009). However, the SAF has a significantly faster slip rate of up to ∼35mm/year (Tong et al., 2014) and earthquake recurrence intervals of 50-100 years (Page and Felzer, 2015) compared to ∼500 years for a strong earthquake ($M_w \geq 6.5$) in the DSF (Hamiel et al., 2009). Another fundamental difference is that the DSF originated in thick, cold lithosphere of ∼80km while the SAF is evolving in a highly variable thermal state with a ∼30km lithospheric thickness (Weber et al., 2009). Like the SAF, the DSF system has newer splays branching from the original transform. The Carmel Fault System (CFS) within the Sinai subplate consists of northwest-southeast trending faults and extends from the central part of the Jordan Valley, just north of the Dead Sea, to the Mediterranean Sea. Both extensional and left lateral motion was identified along the CFS with sub-millimeter slip rates (Sadeh et al., 2012). The slip style, locking depth, and slip rates along the CFS are poorly constrained due to its diffusivity. The CFS experienced a M_w5.3 earthquake in 1984 (Hofstetter et al., 1996), indicating that this region is seismically active.

4.2 Velocity Field from GNSS Positioning and Past Studies

Several studies have used GNSS displacements and velocities to examine the long-term deformation of the DSF region (e.g., Le Beon et al., 2008; Masson et al., 2015). In a more recent study, Gomez et al. (2020) derived an elastic block model for the greater region of the DSF system and found that slip rates decrease northwards along the transform; from 5.0 to 2.2 millimeters per year. Although their main goal was to inspect intraplate deformation,

they also calculated strain-rates and dilatation where station density is sufficient. Compared to the Southern Dead Sea Fault segment, they found a lower rate of strain accumulation along the northern segment. Additional deformation along the Carmel Fault Section could be one explanation for these observations. Local GNSS studies using a combination of campaign and continuous data were performed in the Northern (Hamiel et al., 2016) and Southern (Hamiel et al., 2018b) Jordan Valley sections, Southern Arava Valley section (Hamiel et al., 2018a), and the Southern Dead Sea Basin (Hamiel and Piatibratova, 2019). Left panel of Figure 4.2 shows the available GNSS stations in the region, together with the regional seismicity from 1981 to 2020. Several slip rates were observed with varying locking depth from $\sim$10 to $\sim$20km. Hamiel and Piatibratova, 2021 gathered the longest GNSS dataset in the DSF region, with 23 years of GNSS measurements from 209 campaign and 60 continuous stations. Together with slip rates that are comparable to previous studies, they found shallow creep at two sections; at the Southern edge of the Sea of Galilee ($\sim$2.3mm/yr) and Southern edge of the Dead Sea ($\sim$3.4mm/yr). These sections are spatially correlated with the distribution of thick Halite layers, that may promote velocity strengthening behavior that allows shallow creep.

Deformation along the Carmel Fault System (or Carmel-Gilboa Fault System) is oblique left-lateral and normal, with relative velocities that are $\sim$1mm/yr and below. The deformation area is considered diffusive and its existing knowledge is somewhat ambiguous. In fact, Reinking et al. (2011) suggested both left and right-lateral motion along the fault plane in their dislocation model, although their 10 years of GNSS measurements was poorly fitted to this model. They concluded that an additional sub-fault branch to the Southwest could lead to a better fit. In another GNSS positioning study, Sadeh et al. (2012) identified oblique motion with $\sim$0.7mm/yr of left-lateral and 0.6mm/yr extensional rates. These values are comparable with the most recent study by Hamiel and Piatibratova (2021), who determined $\sim$0.5mm/yr left-lateral and $\sim$0.6-1.1mm/yr fault-normal deformation from their block model in this region. Due to the fault's slow deformation and diffusivity, past observations using GNSS data and satellite imaging techniques are mostly within the measurement noise levels. To date, Nof et al. (2008) is the only InSAR

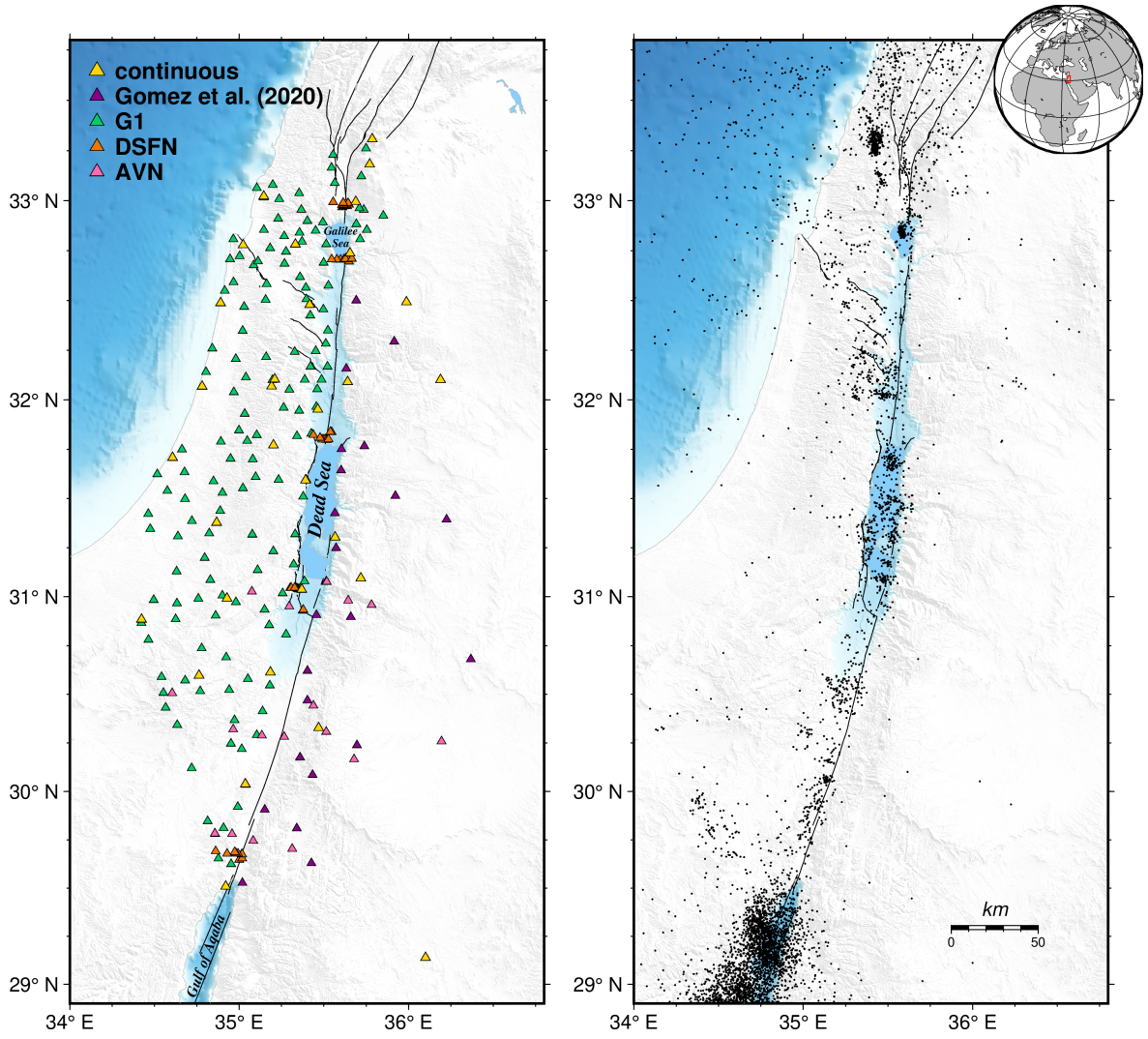

Figure 4.2. Left panel shows the available GNSS stations around the Dead Sea Fault region. Continuous stations in yellow, stations from Gomez et al. (2020) in purple, stations from G1 – Geodetic campaign network of Israel (Sadeh et al., 2012) in green, DSFN – Dead Sea Fault campaign network (Hamiel et al., 2016; Hamiel et al., 2018a; Hamiel and Piatibratova, 2019) in orange, AVN – Arava Valley campaign network (Le Beon et al., 2008; Masson et al., 2015) in pink. Right panel shows regional seismicity from 1981-2020 by the Geological Survey of Israel (updated after Wetzler and Kurzon (2016)), for earthquakes with determined local magnitude of $M_l \geq 2.0$). Main fault segments of the Dead Sea Fault are from Sharon et al. (2020).

study for tectonic deformation that was performed in this area. Nof et al. (2008) processed 9 years of ERS-1 and ERS-2 images (between 1992 and 2001) and found low signal-to-noise ratios, despite using different signal-enhancing methods, and no decisive displacements associated with the CFS.

The Gulf of Aqaba, just South of the Arava Valley section, was extensively studied since the 1995 M_w7.2 Nuweiba earthquake. Ribot et al. (2021) studied the Gulf of Aqaba by multibeam bathymetry and concluded that there is a potential for an additional earthquake rupture of magnitude M_w7+, either strike-slip or normal, that could possibly trigger a devastating tsunami. Li et al. (2021) processed Sentinel-1 satellite images between 2014 and 2020, and used burst-overlap interferometry (BOI) technique to solve for the satellite along track deformation in the Gulf of Aqaba. The along track component of deformation can reveal important information about the tectonic deformation in the region, due to the mostly north-south azimuth of the Dead Sea Fault. Li et al. (2021) found a clear left-lateral movement of 4.2-5mm/yr that is in agreement with GNSS measurements in the Gulf of Aqaba region. Based on their 2D dislocation models, there seems to be a general decrease in locking depth at the southern part of the Gulf as a result of a sharper velocity gradient across the fault. Castro-Perdomo et al. (2021) used GNSS positioning data in the same area and suggested an apparent reduction of locking depth from the inland portion towards the south. They attribute some of their residuals to postseismic deformation associated with the 1995 M_w7.2 Nuweiba earthquake. However, GNSS measurements of a similar event such as the 2010 M_w7.2 El Mayor-Cucapah (Rollins et al., 2015) seems to stabilize around the long-term deformation after $\sim$5 years. With their GNSS surveys conducted more than 20 years after the 1995 M_w7.2 Nuweiba event (between 2015 and 2019), and given its medium magnitude, this scenario is unlikely.

The purpose of this study is to produce detailed velocity and strain rate fields along the DSF by combining GNSS and InSAR measurements. The objectives are (1) to resolve the accumulated strain and varying slip rates in different sections of the fault, (2) examine creeping sections and their shallow creep rates, locked sections and their locking depths, and if signal

allows (3) explore the spatial extent of the Carmel Fault System together with its faulting style (transverse versus extensional) and slip rate accommodation. We would like to examine these topics to better understand earthquake recurrence interval and the general seismic hazard in the area. The combination of GNSS and InSAR measurements for this purpose should allow results with better spatial resolution compared to Gomez et al., 2020 and Hamiel and Piatibratova, 2021. That is, to include InSAR data to overcome sparse GNSS network distribution particularly east of the Dead Sea Fault region. In comparison with Li et al. (2021), we aim for an improved study by exploring a larger region, including the northern segments of Arava Valley and Jordan Valley.

Velocity estimates from GNSS positioning, whether continuous or campaign stations, are generally obtained with a parametric model in the form of

$$\begin{aligned} y(t_i) &= a(t_0) + b(t_i) \\ &\quad + A_0 \sin(w_0 t_i + \varphi_0) + A_1 \sin 2w_1 t_i + \varphi_1 \\ &\quad + \sum_{j=1}^{n_g} g_j H(t_i - T_g) \end{aligned} \tag{4.1}$$

where $y(t_i)$ is the observed displacement in millimeters at epoch t_i, $a(t_0)$ is the value at the initial epoch t_0, and b represents the linear rate (slope) in millimeter per year of interseismic motion. The parameters A_0, φ_0, and A_1, φ_1, are the amplitudes and phases of annual and semiannual motions, respectively. Discontinuities in the time series (also known as noncoseismic "jumps") are often due to GNSS antenna replacements that mostly are recorded in the metadata of the specific station. These are treated with the parameter g_j that represents n_g possible offsets in millimeters due to noncoseismic change at epoch T_g, and H denotes the Heaviside step function. Note that in Equation 4.1 we did not account for coseismic offsets and postseismic deformation as in Klein et al. (2019) since no significant earthquake occurred in the region since the 1995 M_w7.2 Nuweiba earthquake. However, Baer et al. (1999) and Baer et al. (2001) found considerable amount of surface displacement associated with both coseismic and postseismic deformation

around the Red Sea. We assume here that stations at the southernmost edge of our study area, that are more than 100km away from the epicenter, were not significantly affected by the postseismic deformation of the 1995 M_w7.2 Nuweiba event.

We gather GNSS velocities in the Dead Sea Fault region available from Hamiel and Piatibratova (2021). To convert velocities from the International Terrestrial Reference Frame 2014 (ITRF14: Altamimi et al. (2016)) to a local reference frame where the Sinai subplate is held fixed, we use the following relationship (Bock and Wdowinski, 2020) for each GNSS station:

$$\begin{bmatrix} v_E \\ v_N \\ v_U \end{bmatrix} = \omega r \begin{bmatrix} \sin(\theta_P)\cos(\theta_G) - \cos(\theta_P)\sin(\theta_G)\cos(\lambda_G - \lambda_P) \\ \cos(\theta_P)\sin(\lambda_G - \lambda_P) \\ 0 \end{bmatrix} \tag{4.2}$$

where ω is the angular velocity of the Sinai plate's Euler pole defined as the intersection point on Earth's surface spherical coordinates (θ_P, λ_P), r is the earth radius, and (θ_G, λ_G) is the GNSS station's geographic coordinates. From Euler's theorem, the motion of the rigid plates is on a spherical earth's surface so that vertical velocity v_U is zero. For the reference frame conversion, we use the parameters for the Euler pole of the Sinai plate with respect to ITRF14: ω=0.428 °/Myr and (θ_P, λ_P)=(348.81°,54.72°), obtained by Hamiel and Piatibratova (2021). GNSS velocities in Sinai fixed reference frame are shown in Figure 4.3, for both campaign (left) and continuous (right) stations. The velocity field shows a clear left-lateral deformation. However, as mentioned before, some areas experience a sharp change in velocity between the two sides of the fault while others with a more gradual change, suggesting that different segments of the fault are varying between shallow creep and locked fault behavior. Both Figures 4.2 and 4.3 show the sparseness of the GNSS network on the east side of the Dead Sea Fault compared to the its west side. Continuous GNSS stations are sampled more frequently and therefore result in a more precise long-term velocity over time, but making up only $\sim$14% of the entire data set in

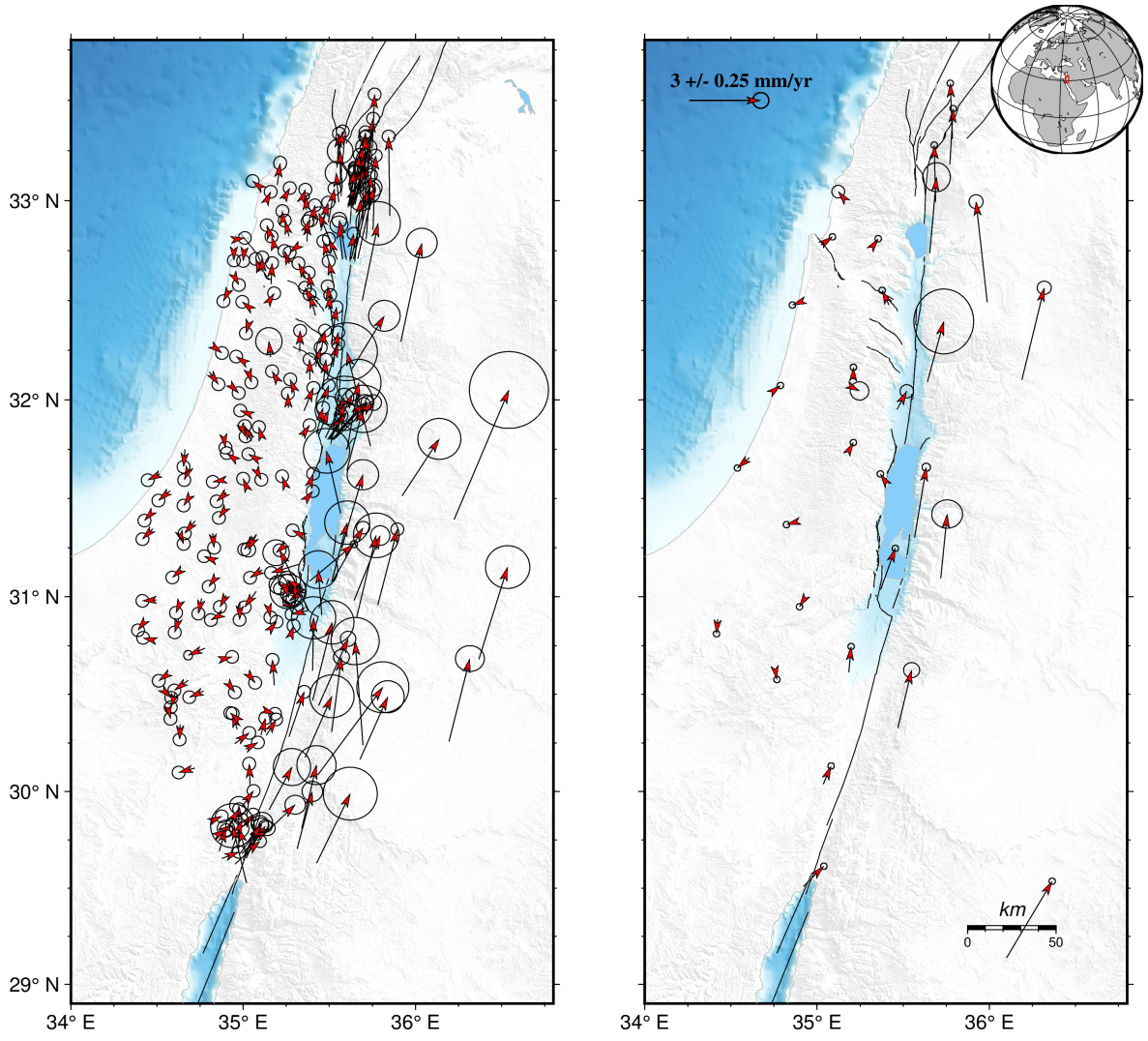

Figure 4.3. Long-term GNSS velocities from campaign (left) and continuous (right) stations. Velocities and their uncertainties are presented with respect to the Sinai fixed reference frame.

the region. The Arava Valley, Dead Sea Basin, and Jordan Valley all serve as a natural boundary between the state of Israel (west) and Jordan (east). Mostly due to political reasons there is hardly any collaborative geophysical research and data sharing between the two countries, despite the seismic hazard. We would like to overcome this spatial limitation with the advantage of InSAR imagery.

4.3 Seven Years of InSAR Line-Of-Sight Displacements

Over the last decade, InSAR has become a common methodology for crustal deformation studies with increasing data availability and open-source programs that facilitate the analysis of displacement (Sandwell et al., 2011; Biggs and Wright, 2020; Xu et al., 2021). While GNSS has a higher temporal resolution of mostly 24-hour sampling (or 1Hz for high-rate), InSAR has higher spatial resolution of tens of meters and up to several meters for commercial satellites. However, Sentinel-1 satellite has a repeating period of only $\sim$6 days (Torres et al., 2012). Furthermore, specifically for the DSF region, InSAR has the ability to measure deformation along the eastern part of the fault where GNSS coverage is limited (Figures 4.2 and 4.3). An important improvement with InSAR is the near fault coverage in areas with good coherence while other slip rates and locking depths inferred from GNSS studies are mostly lacking near field observations. That is with the exception of $\sim$6 GNSS surveys crossing the fault by the Dead Sea Fault (DSF) and Arava Valley (AV) networks (see Figure 4.3), providing higher spatial resolution at these specific locations. By combining both measurements one can benefit from higher GNSS temporal resolution and higher InSAR spatial resolution, providing a better view of the study area and information about short-term (Jin and Fialko, 2020; Xiao et al., 2021) and long-term (Tymofyeyeva and Fialko, 2018; Weiss et al., 2020; Xu et al., 2021) fault processes.

We gather more than 7 years of Sentinel-1 images in both ascending and descending acquisitions that covers our region of interest (Figure 4.4). The total number of images is 368 and 352 for ascending and descending tracks, respectively. We acquire images from October 2014 to

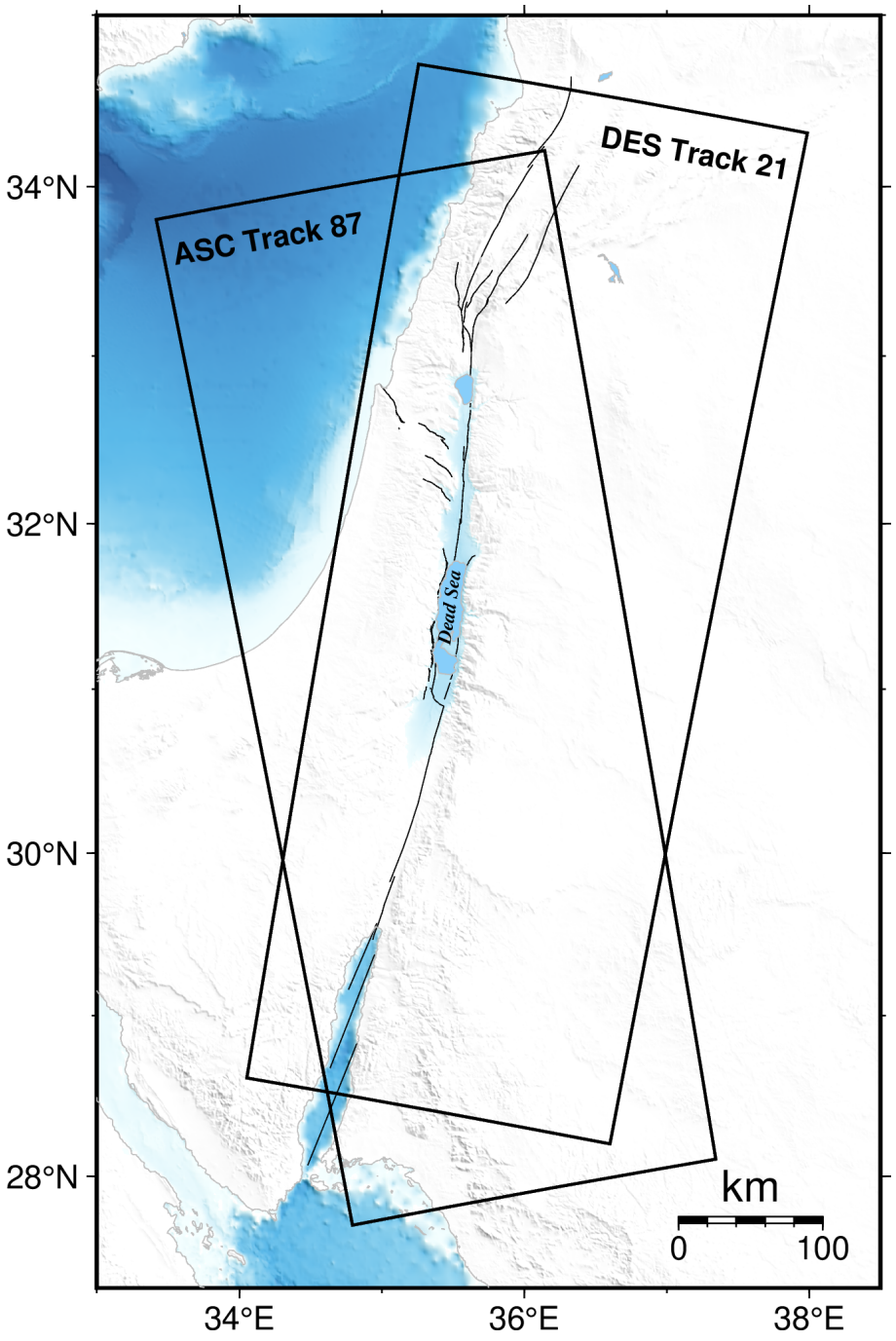

Figure 4.4. Areas of available scenes from ascending track 87 and descending track 21 of Sentinet-1AB satellites. Hundreds of SAR images are freely available by the European Space Agency (ESA) for each area in black rectangle.

January 2022, with a 12-day repeating period of Sentinel-1A alone and a 6-day repeating period starting with the launch of Sentinel-1B in mid 2016 (Figure 4.5). All data preprocessing, phase difference calculations, and further analysis is done using the open source InSAR processing system GMTSAR (Sandwell et al., 2011) linked to the Generic Mapping Tools (GMT) software (Wessel and Smith, 1998; Wessel et al., 2013). For each track, we choose a reference image around the spatial and temporal baselines centered on June 2018 (red dots in Figure 4.5), and align all secondary images accordingly. We select interferogram pairs based on spatial baseline threshold of 200 meters (Xu et al., 2017; Xu et al., 2021) and a temporal baseline threshold of 40 days. We mask out low coherence pixels for the resulting interferograms and use a statistical-cost, network-flow algorithm (SNAPHU) for phase unwrapping to estimate surface displacements in meters given image phase difference in radians (Chen and Zebker, 2002). We then find an area of good coherence and pin all interferograms to that reference region by subtracting its spatial averaged value. To compute the average Line-of-Sight (LOS) velocities for each track, we use the Small Baseline Subset (SBAS) approach (Berardino et al., 2002) that includes a common-scene stacking atmospheric correction (Tymofyeyeva and Fialko, 2015; Xu et al., 2017). To mitigate potential bias from short temporal baselines alone (Ansari et al., 2020) and due to the expected small tectonic deformation in the region, we refine the network of interferograms by adding long ($\sim$1 year) temporal baseline pairs as an input for the SBAS time series algorithm (blue lines in Figure 4.5). The total number of interferograms is more than 4000 for both ascending and descending tracks. Output velocities in the LOS direction are projected from satellite system of azimuth and range to geographic coordinates.

We tie InSAR LOS velocities to GNSS horizontal velocities as a first step of the integration, while we do the component decomposition from both data types next (Chapter 4.4). This step is done to constrain the InSAR data to agree with GNSS velocities at large spatial wavelengths of $\sim$60km, similar to the SURF (Sum-Remove-Filter-Restore) approach (Wei et al., 2010; Tong et al., 2013). We use GNSS velocities from both continuous and campaign networks as an input in the ITRF14 reference frame (Altamimi et al., 2016). For each GNSS station,

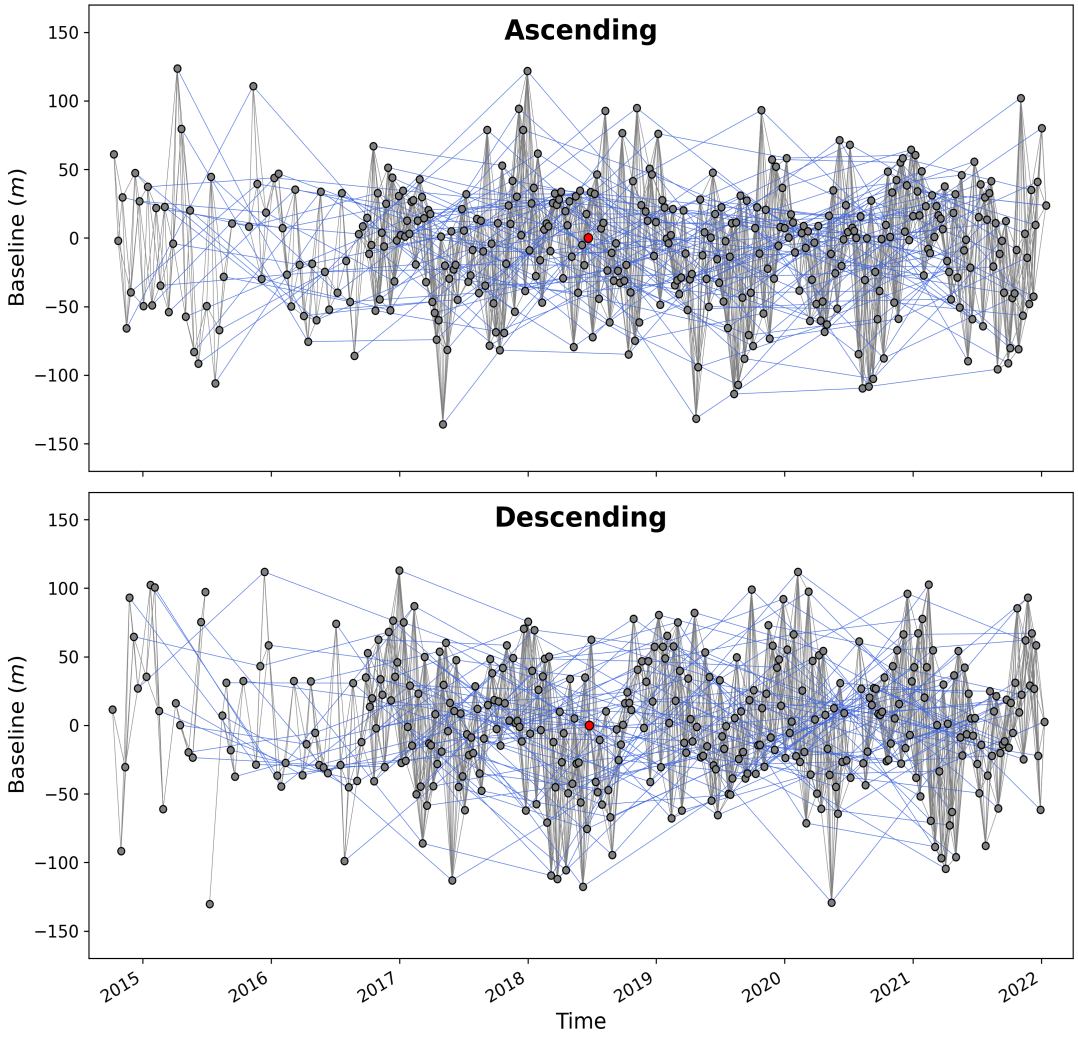

Figure 4.5. Interferogram networks from Sentinel-1 satellite ascending track 87 (top) and descending track 21 (bottom). All secondary images (grey dots) were aligned to a reference image (red dots) around June 2018. Grey lines denote interferograms that are connected with short temporal baselines of < 40 days, blue lines denote interferograms that are connected with long temporal baselines of $\sim$1 year. All interferograms has a spatial baseline of < 200 meters.

we generate a look vector of the reference image and convert to LOS direction of motion. We use vertical velocities from continuous GNSS sites only, as campaign networks obtain vertical velocities that are less accurate. All continuous GNSS stations show a vertical velocity below 1mm/yr, with the exception of Metsoke Dragot station (DRAG) laying close to the Dead Sea shoreline that experiences $\sim$2.8mm/yr uplift. Therefore the inclusion of vertical velocities in this process does not significantly change our results. We then take the difference between InSAR and GNSS velocities in LOS direction and compute its median over $\sim$100 square km blocks using GMT's *blockmedian* to combine nearby measurements and avoid aliasing short wavelengths. We then use GMT's *surface* with a tension factor of $\frac{1}{2}$, and filter the fitted surface with a 10km wavelength Gaussian filter corresponds to a characteristic spacing of GNSS stations in the Sinai plate (left panel of Figure 4.2, and Hamiel and Piatibratova, 2021). We then subtract the LOS velocity difference surface from the InSAR LOS velocity grid to get GNSS tied InSAR results (Figure 4.6). The integrated LOS velocities shows a general velocity change between the two sides of the fault of up to $\sim$15mm/yr in ITRF14 reference frame, for the ascending track. The descending track that is almost parallel to the DSF does not show a clear tectonic related signal. Areas of high vertical deformation rates appear in the same color for both tracks, mostly around the Dead Sea. Additionally, just north of the Sea of Galilee we find a stripe of noisy pixels across the two subswaths of the descending track velocity field that is probably a result of a few bad images. One could visually inspect several images in this region to be excluded before the SBAS analysis to minimize this effect.

Vertical deformation of up to tens of centimeters per year is also apparent in Line-of-Sight (LOS) velocity maps of Figure 4.6. Generally, areas showing the same colorscale for both ascending and descending track velocities are associated with the vertical component either towards (red) or away (blue) from the satellite. At the vicinity of the Dead Sea, both subsidence and uplift occur at various scales. High evaporation rates in the Dead Sea are close to 1 meter per year, causing a drop in its water table (Vey et al., 2021). This leads to a drop in subsurface pore pressure and eventually compaction, together with subsurface material dissolution and sinkholes

formation (Baer et al., 2018; Nof et al., 2019). Nof et al. (2012) used ERS-1 and ERS-2 InSAR data to show a regional uplift of up to 4mm/yr close to the Dead Sea shorelines, likely due to lithospheric rebound. We do not observe this type of deformation but do capture small scale subsidence, mainly on the western shorelines. We also notice significant subsidence around the southern section of the Dead Sea due to extensive mineral extraction (Al-Hanbali et al., 2005). North of the Dead Sea, there are two subsiding regions, near the city of Jericho to the west of DSF and Juwafat on the eastern side, apparently from ground water extraction and farming (Hötzl et al., 2008).

4.4 Combination of GNSS and InSAR Observations for a 3D Velocity Field

Although velocities in the Line-of-Sight (LOS) show a gradient across the Dead Sea Fault, mostly by the ascending acquisition (left panel of Figure 4.6), we would like to reveal more tectonic-related features by decomposition to horizontal and vertical components of deformation. We first resample the Sentinel-1 LOS velocities to the same $\sim$500 by 500 meters grid that covers the common area of both ascending and descending velocity maps. To calculate the full 3D velocity field, we note that both viewing geometries are relatively insensitive to north-south motion and therefore should rely on GNSS direction of motion to help constrain this component. We therefore use the east and north components of velocity from the available GNSS stations in the region as an input to *gpsgridder*. The *gpsgridder* algorithm interpolates a sparse vector dataset based on the Green's functions of an elastic body subjected to in-plane forces (Sandwell and Wessel, 2016). Adjusting the number of eigenvalues in the singular value decomposition (SVD) by the *gpsgridder* achieves smoothing between the GNSS data and model misfit. Sandwell and Wessel (2016) found that using a number of eigenvalues that is $\sim$25% of the number of data points is adequate for GNSS data. For our $\sim$200 GNSS stations with two components each (east and north), we use the 100 largest eigenvalues and a typical Poisson's ratio of $\frac{1}{2}$. The output of

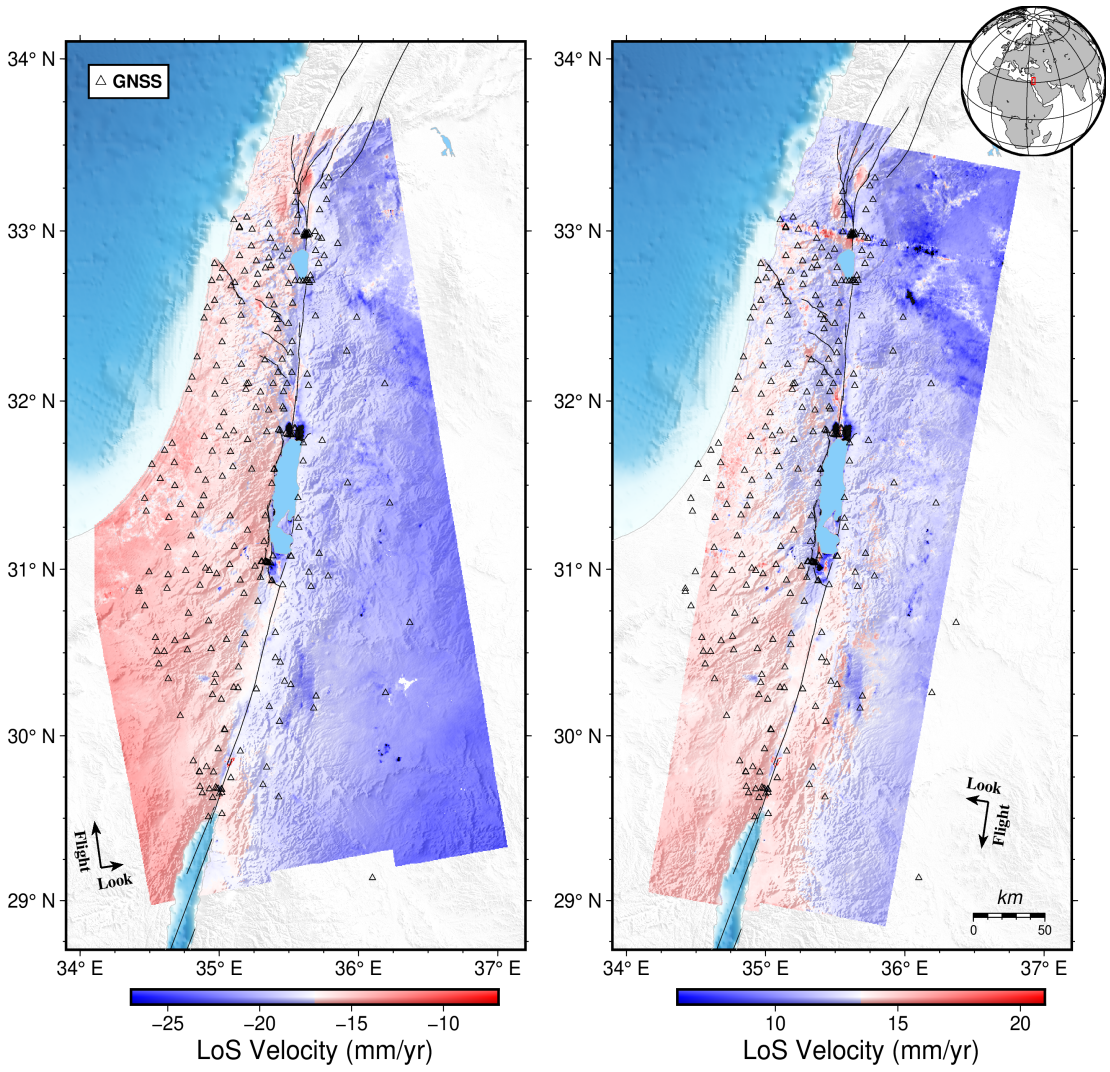

Figure 4.6. Line-of-Sight (LOS) velocities in ITRF14 reference frame for ascending (left) and descending (right) Sentinel-1 satellite tracks, after tying to GNSS velocities. Red colors denote velocity in the direction towards the satellite, while blue colors denote velocity away from it. Satellite flight and look direction is indicated at each panel. GNSS stations denoted as black triangles.

gpsgridder are horizontal GNSS velocities interpolated to the common grid of the InSAR LOS velocities. We then calculate the ratio between horizontal GNSS velocities for each pixel of our grid, defined by:

$$\gamma = \frac{GNSS_N}{GNSS_E} \tag{4.3}$$

where $GNSS_E$ and $GNSS_N$ are east and north components of interpolated GNSS velocities. A similar procedure has been done by Tymofyeyeva and Fialko (2018), although they calculated the azimuth of GNSS velocities by the arctangent of their ratio.

We first separate the east (v_E) and up (v_U) component of velocity by solving the following system equations:

$$\begin{bmatrix} v_a \\ v_d \end{bmatrix} = \begin{bmatrix} e_a + \gamma n_a & u_a \\ e_d + \gamma n_d & u_d \end{bmatrix} \begin{bmatrix} v_E \\ v_N \end{bmatrix} \tag{4.4}$$

where v_a and v_d are InSAR LOS velocities from ascending and descending tracks, respectively. The satellite look vectors at each pixel are $(enu)_a$ and $(enu)_d$ for each track. The north component of velocity is given by the ratio and the resulted east component:

$$v_N = \gamma v_E \tag{4.5}$$

All steps in this decomposition process are done in the ITRF14 reference frame. We transform the velocity components from ITRF14 to a Sinai-fixed reference frame using Equation 4.2.

Weiss et al. (2020) used ∼5 years of Sentinel-1 interferometry in the North Anatolian Fault together with GNSS data to solve for surface velocities. Ou et al. (2022) used ∼4.5 years of Sentinel-1 interferometry and GNSS in the northeastern region of the Tibetan Plateau and decomposed east (v_E) and up + north (v_{UN}) velocities as a first step, before decomposing v_{UN} into

up (v_U) and north (v_N) velocities. They found only negligible differences with a decomposition of north (v_N) and up + east (v_{UE}) velocities and concluded that both methods can be used without significantly affecting the final results. Both Weiss et al. (2020) and Ou et al. (2022) assumed a north component of velocity by the interpolated GNSS data alone, not taking into account the contribution from LOS components. This is mostly due to the dominant east-west direction of tectonic motion in their study areas. In our case of the Dead Sea Fault, most of the tectonic deformation is expected in the north-south component. As we would like to reveal small scale features and overcome the unfavorable GNSS station distribution in the area, we do take into account LOS velocities when solving for the full 3D velocity field. However, unraveling the north-south deformation is a challenge because the satellite's look angles are less sensitive to this component. The resulting 3D velocity field from the combined InSAR and GNSS measurements is shown in Figure 4.7, in the Sinai-fixed reference frame. While noise levels in the velocity components are relatively high, we notice a clear signal resembling a left-lateral strike slip motion in the north component (middle panel) with ∼4-6mm/yr difference between the Sinai subplate and Arabia plate that is in agreement with previous GNSS studies (Gomez et al., 2020; Hamiel and Piatibratova, 2021). Looking at the east-west component (left panel of Figure 4.7), we see deformation similar to pull-apart motion in the area south of the Dead Sea, although with amplitudes that are smaller than the north-south component. Owing to the fact that such behavior was not documented before and previous work in the Arava Valley area suggests pure strike-slip motion, we suggest that this signal may be associated with InSAR time series noise effects.

To examine different segments of the Dead Sea Fault, we focus on several profiles across the fault by looking at both GNSS velocities and our combined GNSS & InSAR velocities. For each profile, we rotate the east (v_E) and north (v_N) components into a fault normal and fault parallel velocities using a simple rotation around the vertical axis:

$$\begin{bmatrix} v_\perp \\ v_\parallel \end{bmatrix} = \begin{bmatrix} \cos\alpha & \sin\alpha \\ -\sin\alpha & \cos\alpha \end{bmatrix} \begin{bmatrix} v_E \\ v_N \end{bmatrix} \tag{4.6}$$

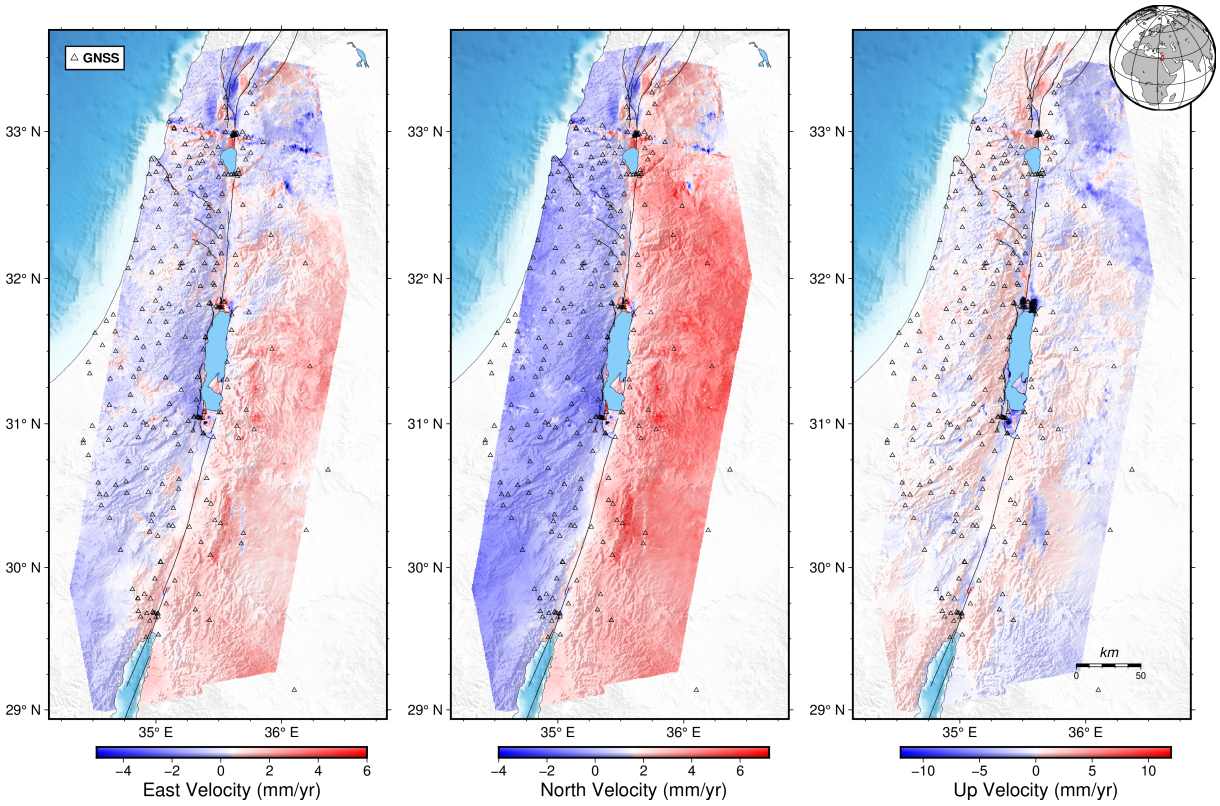

Figure 4.7. East (left), north (middle), and up (right) velocities decomposed from the combination of Sentinel-1 InSAR & GNSS data. Horizontal velocities were converted from ITRF14 into Sinai fixed reference frame. Results are shown in the area common to both ascending and descending satellite tracks. Color scale for the horizontal components was chosen uniformly around the $L1$ norm median of the map.

where $v_\perp$ and $v_\parallel$ are fault perpendicular and fault parallel velocities, respectively. The azimuth of each fault segment (α) is estimated based on the two chosen points along the fault. Dominated by left-lateral deformation, the parallel velocity ($v_\parallel$) should help quantify the slip partitioning in the Dead Sea Fault together with associated locking depths. At each profile, we compare our combined InSAR & GNSS solution with GNSS measurements alone at particular stations. The Jordan Valley section profiles are shown in Figures 4.8 and 4.9, while the Arava Valley section profiles are shown in Figures 4.10 and 4.11. We represent each of our fault segments using a semi-finite 2D dislocation in a homogeneous half-space. The fault parallel surface velocity can be expressed as (Savage and Burford, 1973):

$$v_\parallel = \frac{V_0}{\pi} \arctan \frac{x}{D} \tag{4.7}$$

where V_0 and D are the long-term slip rate and locking depth, respectively, and x is the fault perpendicular distance. For several profiles that were previously studied and showed creeping behavior (A, D, and E), we also use a simple step function to model geodetic slip rates. We use a Levenberg-Marquardt algorithm to perform the least-squares minimization between the model and data points.

The Jordan Valley section of our study area (Figure 4.8) is divided into 3 profiles shown in Figure 4.9 and defined by the letters A-C. Although higher noise levels than the uncertainties in the GNSS velocities are present in our combined InSAR & GNSS solutions (grey dots in Figure 4.9), the dense spatial coverage of the InSAR component clearly compensates for the lack of GNSS data on the east side of the valley. The InSAR & GNSS profiles show a distinct velocity change between the two sides of the fault. Individual GNSS velocities (black triangles in Figure 4.9) mostly agree with the combined solution. In general, GNSS velocities that were estimated using campaign surveys have larger uncertainties compared to continuous sites, as shown by the error bars. Our preferred best-fitting model based on Equation 4.7 is shown as red

curve for at each panel, together with the resulted slip rates and locking depth at the bottom right. These models fit the combined fault parallel velocities with root mean square errors of 0.6-0.8 mm/yr.

Profile A crosses the southern part of the Sea of Galilee and shows a very shallow locking depth of ∼4km with a slip rate of ∼4mm/yr. A previous study by Hamiel et al., 2016 suggests that this segment is freely creeping at the shallow portion of the fault, making it likely that a step function would be a more suitable model in this case. We therefore add a shallow creeping model of a step function resulting in a creeping rate of ∼3mm/yr. However, the sharp velocity change from GNSS stations alone occurs around ±1km distance while the combined solution is best described by a velocity change ∼5km to its west. Profile B in our study region might be crossing two branches of the fault according to the Sharon et al. (2020) fault model. GNSS velocities are slightly larger than our combined solution, but generally agree and show a similar velocity change across the fault. Profile C includes the southern part of the Jordan Valley and the northern section of the Dead Sea where strong vertical deformation is present. This area of the Dead Sea was previously studied by Hamiel et al. (2018b) using GNSS campaign sites (included here) showed a slip rate of 4.8mm/yr with a locking depth of ∼16.5km. These values are slightly different than our higher slip rate of 5.2mm/yr and a larger locking depth of ∼22km. However, seismicity profile along the Dead Sea fault shows that the northern part of the Dead Sea basin experience earthquakes with up to ∼25km depth that are significantly deeper than other parts of the fault (Figure 7 of Hamiel and Piatibratova (2021)). It is worth mentioning that our profile C here includes a larger area than the relatively narrow (30x30km) area studied by Hamiel et al. (2018b).

We divide the Arava Valley section (Figure 4.10) into 6 profiles shown in Figure 4.11 and defined by the letters D-I. Here we notice that velocity gradients between the Sinai and Arabia plates are larger compared to the Jordan Valley section. The azimuth change of the fault in this area may contribute to fault parallel sensitivity by ascending track images taken by Sentinel-1 satellite (∼30% between ascending track and fault azimuth). Here we also notice

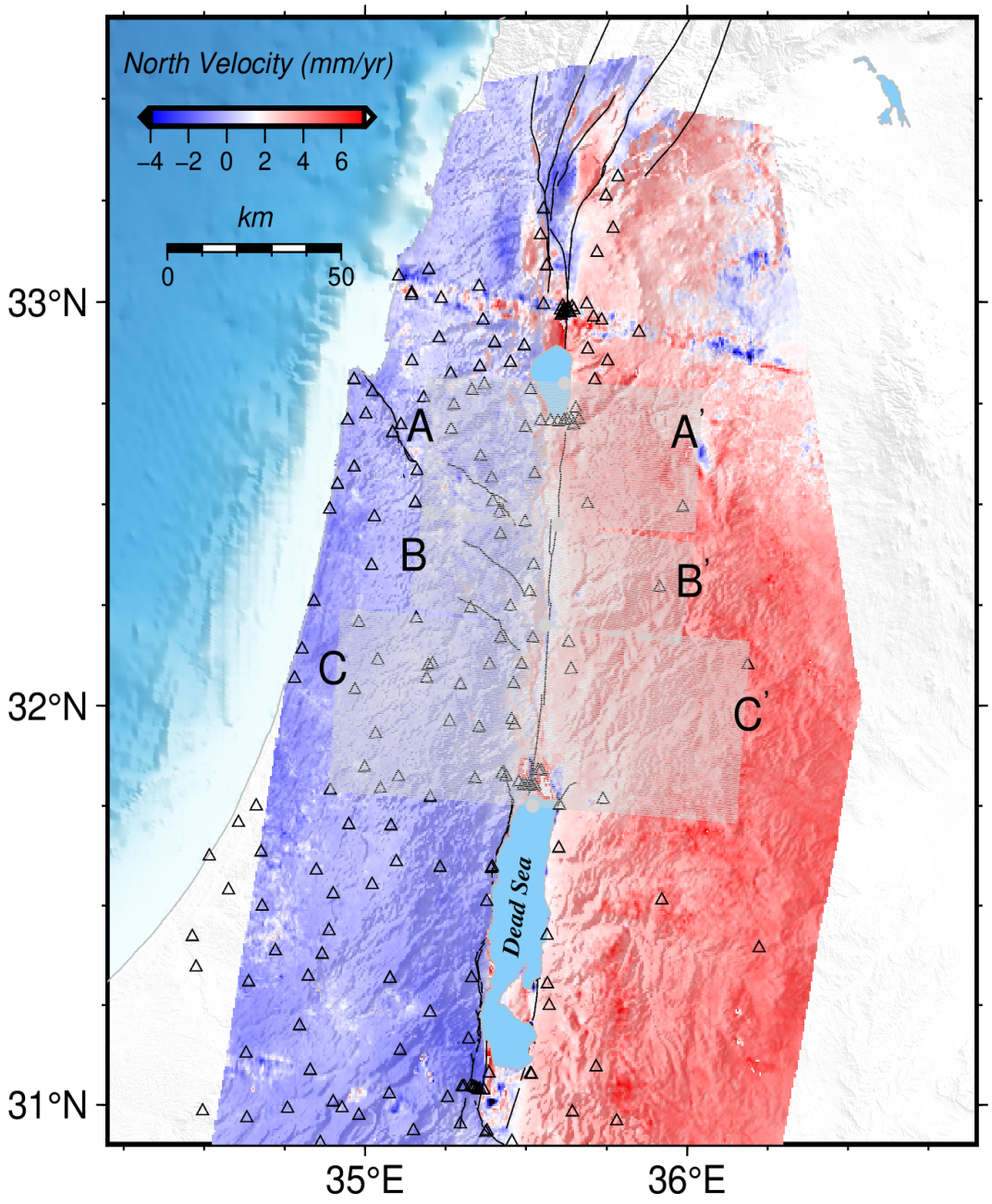

Figure 4.8. Across fault profiles at the Jordan Valley section of the Dead Sea fault. Map colors correspond to the combined InSAR & GNSS velocity field in the north component. GNSS stations are shown as black triangles. Profiles A - C are shown in Figure 4.9 after rotation to fault parallel velocities using Equation 4.6.

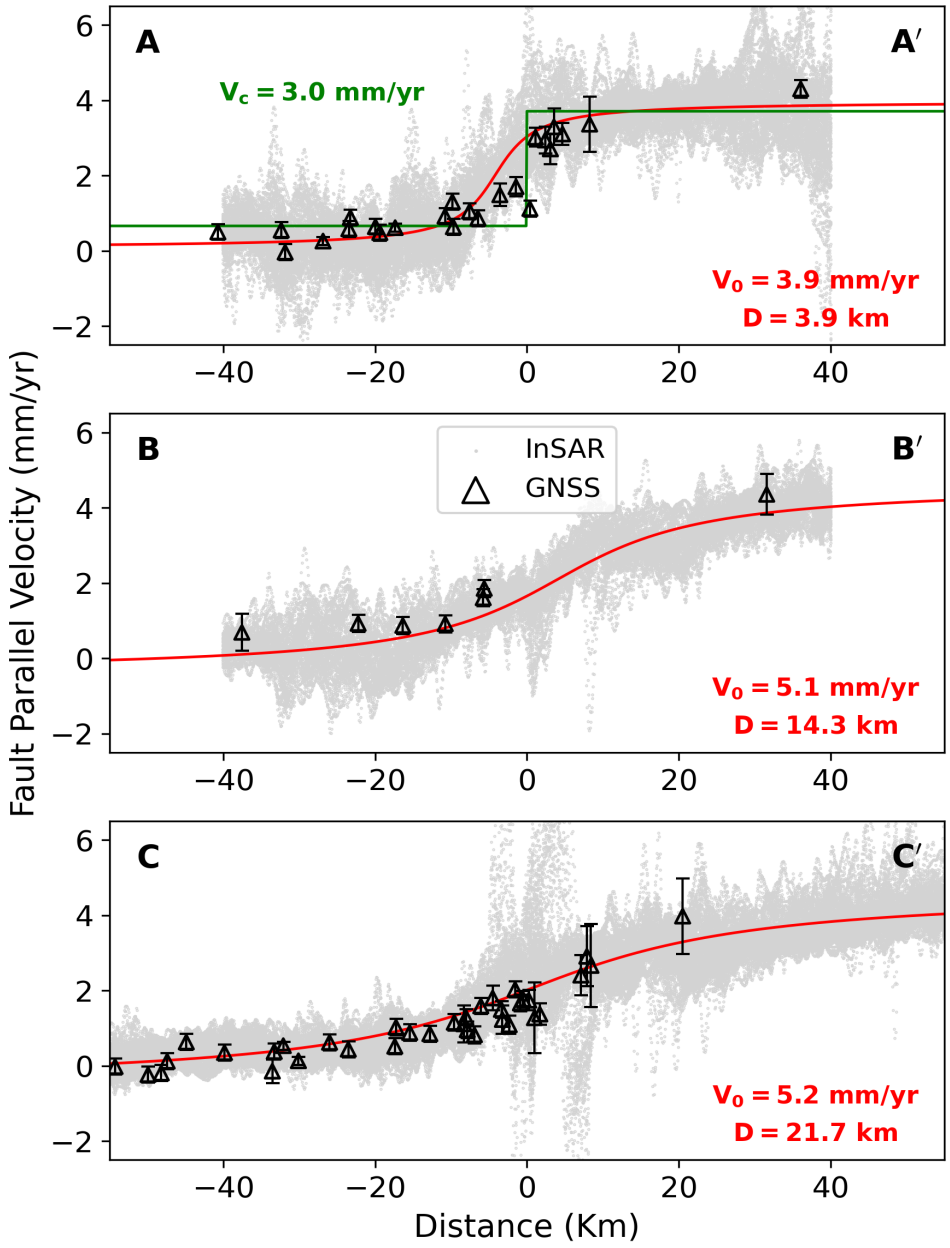

Figure 4.9. Fault parallel velocities of profiles A – C, from Figure 4.8 of the Jordan Valley section. Grey dots correspond to the combined InSAR & GNSS pixel velocities, black triangles correspond to individual GNSS station velocities with $\pm 1\sigma$ uncertainties. The locked fault model that best describes the combined solution (grey dots) is shown as red curve. Resulted slip rate (V_0) and locking depth (D) is shown at the bottom right of each profile's panel. Shallow creeping model is added to profile A and shown as green curve, with its resulted creeping rate (V_c).

a good agreement between our combined velocity field and individual GNSS observations, despite some scatter. Best-fitting models result in root mean squared errors in the range of 0.4-1.1mm/yr. The two northern profiles of D and E show larger best fitting errors due to vertical deformation associated with the Dead Sea and surrounding area may be leaking into the horizontal components. Similar to Profile A, south of the Sea of Galilee, profiles D and E are modeled as shallow creep together with a locked fault yielding creeping rates of 3.6 and 3.9mm/yr for profiles D and E, respectively. Both profiles cover the southern part of the Dead Sea, with profile E covering two additional branches of Sedom and Amazyahu (Hamiel and Piatibratova, 2019). Two previous studies (Hamiel and Piatibratova, 2019; Hamiel and Piatibratova, 2021) suggest that this section experiences shallow creep. Hamiel and Piatibratova (2021) associated both creeping sections (our profile A south of the Sea of Galilee and profiles D-E south of the Dead Sea) to shallow Halite layers, which promote velocity strengthening in the shallow subsurface. Although largely agreeing with the GNSS velocities, profile I resulted in a slip rate of more than 7mm/yr and locking depth of more than 40km that are much larger than a similar profile by Hamiel and Piatibratova (2021) and unrealistic for this region. This might be due to lack of GNSS station coverage on the southwestern edge of our study area. Without far-field constraints, interpolated velocities may introduce a linear behavior outside the region of known observations. Profiles G-H shows an increase in locking depth from $\sim$12km to $\sim$20km, with similar slip rate of $\sim$5mm/yr. These values are slightly larger than other studies near the Gulf of Aqaba (e.g., Li et al., 2021). Hamiel et al. (2018a) who studied the area of profile I suggesting that stress changes associated with the 1995 M_w7.2 Nuweiba event could promote the next earthquake and this section of the Arava Valley is in its final interseismic phase stage. Hamiel and Piatibratova (2021) also found larger values of slip rates at the southern sections of the Dead Sea fault, similar to our case of Arava versus Jordan Valley sections. Slip partitioning on the Carmel Fault can explain these differences between slip rates in the two valleys. Indeed, Gomez et al. (2020) found some intraplate motion in this area and decided to include the Carmel Fault in his block model. In our combined InSAR & GNSS velocity field it is hard to determine

tectonic deformation associated with the Carmel Fault due to its very slow ($\sim$1mm/yr) slip rates that are within our noise levels.

Strain rate models give additional information on the regional tectonics, by telling us about the level of activity and localization of crustal deformation (Kreemer et al., 2003). Since it is directly related to subsurface stress build-up, it usually correlates well with global patterns of earthquake activity and occurrence rates (Kreemer et al., 2002; Kreemer et al., 2014). On a more local scale, strain rates provide the amount of intraplate deformation (Gomez et al., 2020) and an indication of fault slip behavior (shallow creeping versus locked). There are several ways of estimating surface strain rate fields using geodetic measurements (e.g., Shen et al., 2015; Haines et al., 2015; Pagani et al., 2021). In this analysis we continue to use *gpsgridder* (Sandwell and Wessel, 2016) to interpolate both our irregularly distributed GNSS stations and InSAR & GNSS combined velocity fields to create two strain rate models. In both methods, we perform the analysis on a $\sim$10km (0.1°) grid size represents the average distance between GNSS stations in our area, although sparser on the Arabia plate (Hamiel and Piatibratova, 2021). For the GNSS data we simply use 100 eigenvalues ($\sim$25% of our data points), as suggested by Sandwell and Wessel (2016) and described above. For the InSAR & GNSS combined solution we first mask out pixels with high vertical deformation ($|v_U| \geq$ 10mm/yr) that may be leaking into the horizontal components, and a rectangular polygon of the area affected by noisy images from the descending track LOS just north of Sea of Galilee (Figure 4.6, right panel). We then preprocess the horizontal velocity grids by down-sampling (to a $\sim$10km grid size) and run a spatial Gaussian filter with a 50km wavelength. In this analysis, we expect a number of reliable pixels to be approximately $\frac{1}{2}$ of our filtered wavelength (corresponds to $\sim$25km). For our study area of $\sim$270km by 475km, that is 11 x 19 data points for each component, resulting in 418 eigenvalues ($\sim$16% of the total) for the SVD in *gpsgridder*. Once we have the uniform horizontal velocity fields for both GNSS and InSAR & GNSS analysis, we resample our grids to $\sim$500 meters using bicubic interpolation by GMT's *grdsample*. The horizontal strain rate tensor ($\dot{\varepsilon}$) can be written as the spatial derivatives of the horizontal velocities (Turcotte and Schubert, 2002):

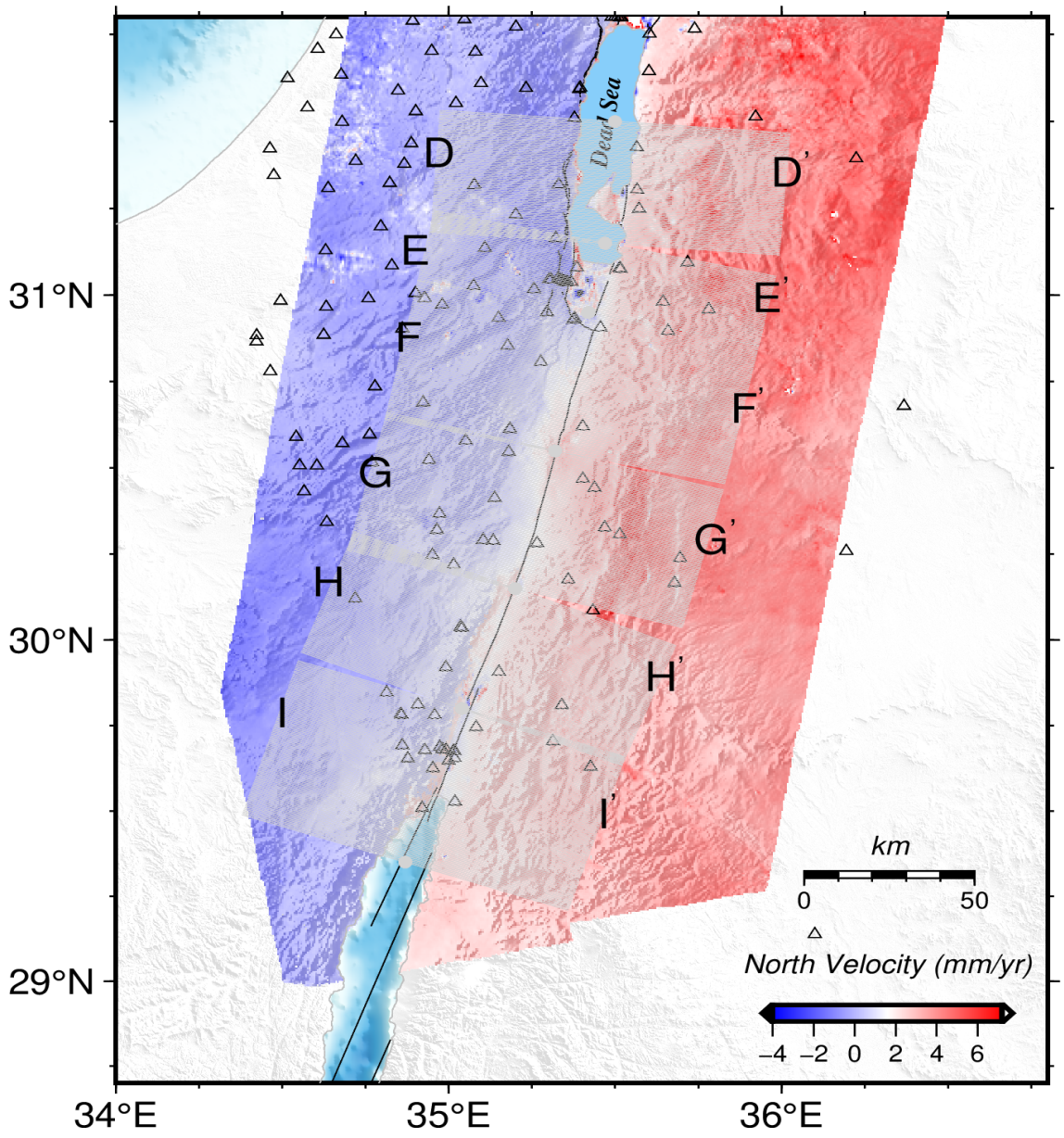

Figure 4.10. Across fault profiles at the Arava Valley section of the Dead Sea fault. Map colors correspond to the combined InSAR & GNSS velocity field in the north component. GNSS stations are shown as black triangles. Profiles D - I are shown in Figure 4.11 after rotation to fault parallel velocities using Equation 4.6.

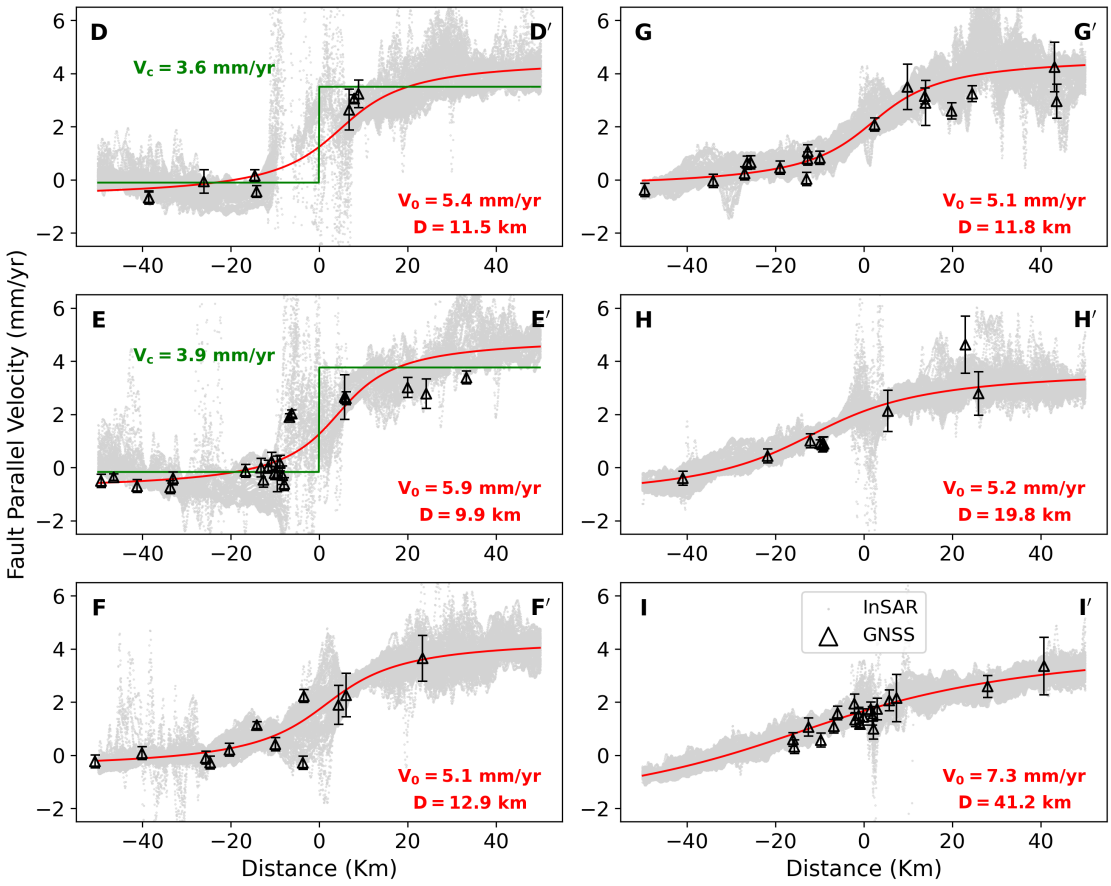

Figure 4.11. Fault parallel velocities of profiles D – I, from Figure 4.10 of the Arava Valley section. Grey dots correspond to the combined InSAR & GNSS pixel velocities, black triangles correspond to individual GNSS station velocities with $\pm 1\sigma$ uncertainties. The locked fault model that best describes the combined solution (grey dots) is shown as red curve. Resulted slip rate (V_0) and locking depth (D) is shown at the bottom right of each profile's panel. Shallow creeping model is added to profiles D and E and shown as green curve, with its resulted creeping rate (V_c).

$$\dot{\varepsilon} = \begin{bmatrix} \dot{\varepsilon}_{xx} & \dot{\varepsilon}_{xy} \\ \dot{\varepsilon}_{yx} & \dot{\varepsilon}_{yy} \end{bmatrix} = \begin{bmatrix} \frac{\partial v_E}{\partial x} & \frac{1}{2}(\frac{\partial v_N}{\partial x} + \frac{\partial v_E}{\partial y}) \\ \frac{1}{2}(\frac{\partial v_E}{\partial y} + \frac{\partial v_N}{\partial x}) & \frac{\partial v_N}{\partial y} \end{bmatrix} \tag{4.8}$$

From which we can derive the maximum shear rate ($\dot{\varepsilon}_{shear}$), the 2^{nd} invariant ($\dot{\varepsilon}_{II}$), and horizontal dilatation rate ($\dot{\varepsilon}_{\triangle}$) of the tensor are:

$$\begin{aligned} \dot{\varepsilon}_{shear} &= \frac{1}{2}\sqrt{\dot{\varepsilon}_{xy}^2 + (\dot{\varepsilon}_{xx} - \dot{\varepsilon}_{yy})^2} \\ \dot{\varepsilon}_{II} &= \sqrt{\dot{\varepsilon}_{xx}^2 + 2\dot{\varepsilon}_{xy}^2 + \dot{\varepsilon}_{yy}^2} \\ \dot{\varepsilon}_{\triangle} &= \dot{\varepsilon}_{xx} + \dot{\varepsilon}_{yy} \end{aligned} \tag{4.9}$$

Results for the 2^{nd} invariant model of the Dead Sea Fault region are presented in Figure 4.12, for both GNSS and InSAR & GNSS combination.

Our strain rate models display high strains along the Dead Sea Fault tectonic features and generally in agreement with areas that experienced earthquake in the past ∼40 years (Figure 4.2). As shown in Figure 4.12, high values of the $2^n d$ invariant strain rate, $\dot{\varepsilon}_{II}$, (up to ∼100 nanostrain per year) are found along the northern section of the Arava Valley, and the northern section of the Jordan valley. Recent strain analysis by both Gomez et al. (2020) and Hamiel and Piatibratova (2021) suggest a similar range of $\dot{\varepsilon}_{II}$ values. For comparison, strain rates exceed 150 nanostrain/yr along the North Anatolian Fault in Turkey (Weiss et al., 2020), and 200 nanostrain/yr along the San Andreas Fault area in California (Xu et al., 2021) especially in known creeping sections. Ou et al. (2022) found more than 400 nanostrain/yr along two creeping sections at the northeast Tibetan Plateau. In both of our strain rate models, we do not see significant strain rates along the Carmel Fault Section. That is probably due to very slow slip rate (∼1mm/yr) that was previously reported in this area (Sadeh et al., 2012; Hamiel and Piatibratova, 2021). Comparing these results to our profiles analysis, we notice that fault segments with sharp velocity change between

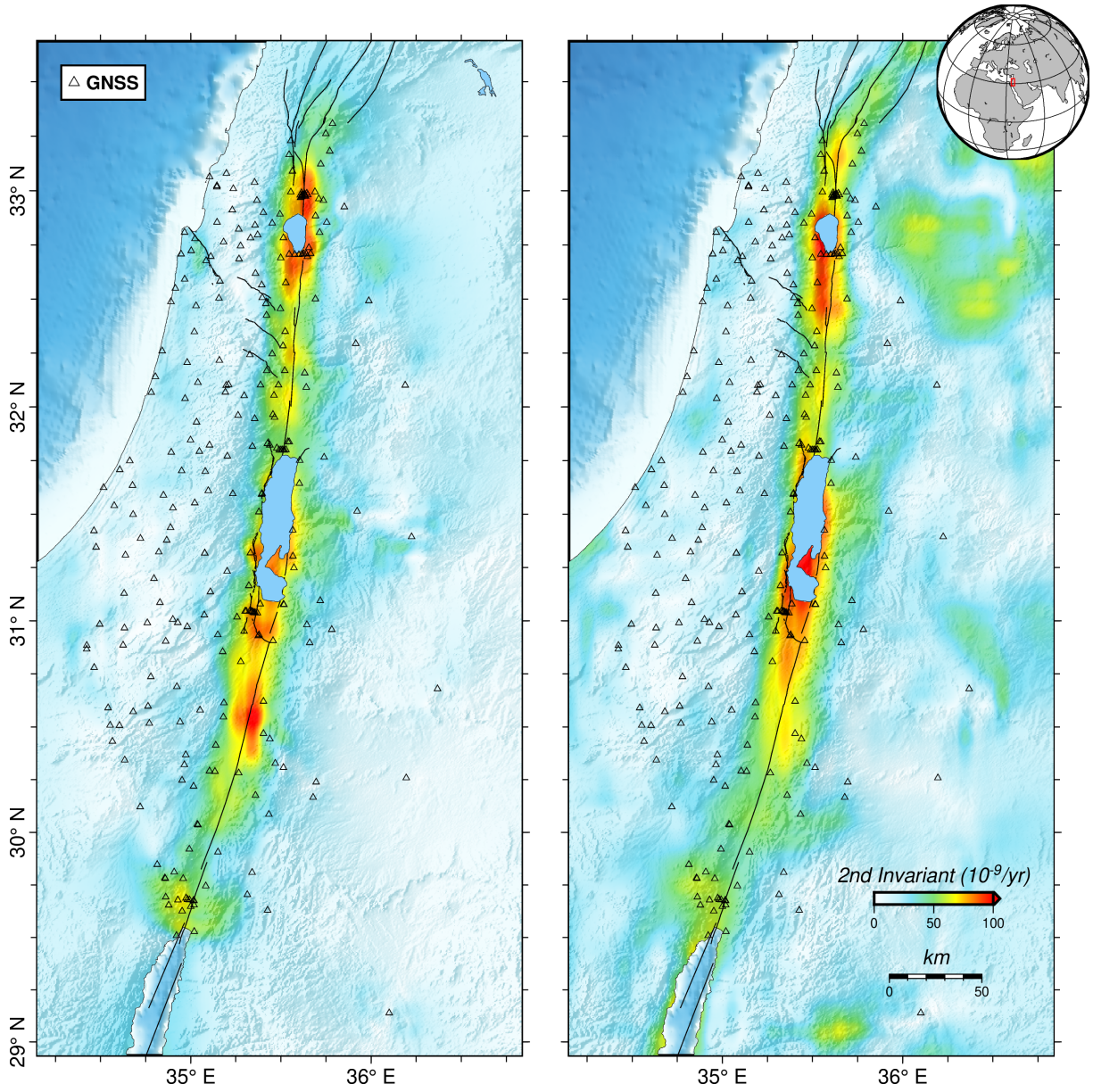

Figure 4.12. Second invariant of the horizontal strain rates from GNSS (left) and InSAR & GNSS (right) models for the Dead Sea Fault region. Black triangles show GNSS sites locations. Main fault segments of the Dead Sea Fault are from Sharon et al. (2020).

the Sinai and Arabia plates (profiles A, D, and E) experience the highest strain rates. From Equation 4.8, creeping sections with larger spatial velocity gradient are expected to show larger values of strain. On the other hand, fault locking is consistent with the width of the strain area. As opposed to these creeping profiles, a few sections exhibit smoother velocity changes and larger locking depths such as B, C, and H, showing smaller strain values that are more spread out away from the fault. Lower strain rates at this middle section of the Arava valley is consistent with Gomez et al. (2020). Hamiel and Piatibratova (2021) suggest a strain rate model with higher strains along the entire Arava Valley, with slight decrease towards the south which is consistent with their deeper locking depth. However, these two models have coarse resolution of $\sim$10km compared to our final model of $\sim$500 meters grid size. Generally, these locked fault areas are known to build-up subsurface stress and therefore are more prone to experience medium sized earthquakes in strike-slip environments. Based on historical records (discussed in Chapter 4.1), the Dead Sea Fault and its branches are capable of producing earthquakes with maximum magnitudes of M_w7.5-7.8 (Nof and Allen, 2016). Our combined InSAR & GNSS model (right panel of Figure 4.12) reveals more strain accumulation in some areas where GNSS station distribution is sparse. For example, the east shoreline of the Dead Sea and at its southern section in the vicinity of Sedom and Amazyahu faults. Additionally, a small section of the West Boundary Fault (WBF) at the northwestern edge of the Dead Sea is highlighted by higher strain in the combined model compared to GNSS alone. Shallow creeping was not previously documented in this segment (Hamiel et al., 2018b). The middle section of the Jordan valley, where no GNSS campaigns were conducted, shows $\sim$20-30 nanostrain/yr higher strain rates in the InSAR & GNSS model compared to GNSS alone. Similarly, the very north edge of our study area at Mount Hermon, shows up to $\sim$50 nanostrain/yr in the combined model while GNSS alone does not show strain accumulation. InSAR LOS also introduces noise that is most likely due to vertical deformation, in the northeast region of our study area. There are two regions where the combined model results in slightly lower strain rates compared to the GNSS alone: the middle section of the Arava Valley, and north of the Sea of Galilee. In both cases, the combined

model (Figure 4.12, right panel) results in an extra $\sim$25 nanostrain/yr. Taking into account the noisy images affecting the descending track's LOS velocity (Figure 4.6, right panel), the region north of the Sea of Galilee may not be reliable.

Acknowledgements

Chapter 4 is currently in preparation for publication as: Golriz, D., Xu, X., Hamiel, Y., Bock, Y., Sandwell D. T. "Interseismic Deformation in the Dead Sea Fault Region Revealed by InSAR and GNSS Measurements", in prep. The dissertation author was the primary investigator and author of this material.

Chapter 5

Summary and Future Outlook

The studies that comprise this dissertation consider the combination of geophysical data sets to investigate the different phases of the crustal deformation cycle. The optimal combination of seismic (i.e., strong-motion accelerometers, broadband seismometers) and geodetic (i.e., Global Navigation Satellite Systems - GNSS, Interferometric Synthetic Aperture Radar - InSAR) measurements provides a more robust image of physical processes in tectonically active environments, which can then be used for hazards mitigation. In Chapter 1 we lay out the research questions and motivation behind these studies. We also introduce the geophysical data types used throughout this dissertation and discussed their advantages with respect to observing the crustal deformation cycle and how they complement each other.

In Chapter 2 we introduce a new physics-based approach to define the coseismic phase of the crustal deformation cycle and its transition to early postseismic deformation using seismic velocities and 1Hz GNSS displacements from interwoven regional networks. Current practice in coseismic studies is to use daily GNSS positioning, or to assume a single time window for all affected stations when using high-rate GNSS positioning. We study ten earthquakes with a range of magnitudes and focal mechanisms and show that we are able to capture both static and dynamic components of earthquake deformation within our calculated coseismic time window, for each station individually. The average width of the coseismic time window can vary from less than a minute in the vicinity of a moderate strike-slip event to more than 6 minutes at farther

distances from great earthquakes. By using the measure of total energy release of the signal we get a more focused picture of the transition to postseismic deformation. The coseismic window gets extended as the separation of the different seismic phases such as surface waves become more pronounced, and possibly due to path, site, and source directivity effects. By comparing daily static offsets with the ones derived from our windowing technique, we show that GNSS displacements that are based on daily positioning include significant contributions from the very first hours of postseismic deformation following the earthquake and before the next day's position. For the ten earthquakes in this study, we find that surface deformation in the early postseismic period has a median value of 20% of the coseismic motion and exhibits significant spatial variations within a day of an event.

We further examine the contribution from early postseismic deformation and assess the impact of merging postseismic and coseismic displacements on earthquake fault slip models. We compare daily displacement time series input, as adopted in numerous studies, with our rapid estimates over a several-minute coseismic time window. Based on our inversions of four of the earthquakes, significant postseismic slip can propagate throughout the rupture area and are on the order of up to 1 meter for a strong normal faulting event, 2 meters for the two major strike-slip events, and up to 6 meters for the great thrust event. Additionally, slip inversions that rely on daily displacement results in larger earthquake magnitude estimates. For the great 2011 M_w9.1 Tohoku-oki earthquake, we also see significant vertical displacements of several centimeters within a 10-minute window compared to the rapid coseismic window of 2-6 minutes. Thus, the choice of the high-rate GNSS data window can result in significant intermingling of coseismic slip associated with seismic rupture and postseismic slip. Distinguishing the transition from the coseismic to the postseismic phase is critical, not only for improving fault slip models, but also for understanding the earthquake source and its evolution.

Future studies will be needed to assess the significance of our definition of the coseismic phase to achieving a better insight into the physical processes underlying the crustal deformation cycle. Since postseismic deformation generally decays exponentially, the slip over the first

few hours is greatest and should be taken into account for a more detailed postseismic model. Improved postseismic modeling can shed light on different postseismic processes and their individual contributions (e.g., afterslip versus viscoelastic relaxation versus poroelastic rebound). Defining and quantifying early postseismic deformation can be a crucial component in understanding crustal rheology as it controls the evolution of postseismic decay. However, high-rate GNSS displacements are often not readily available within sparser networks compared to daily displacements. Similarly, InSAR repeat-cycles suffers from relatively inferior temporal sampling rate of at least a few days. To account for the early postseismic deformation, one can potentially take static offsets from high-rate GNSS as the ground truth of earthquake coseismic deformation. Substracting these "true" coseismic offsets from GNSS and/or InSAR data that spans both the coseismic phase and early postseismic, will likely result in more complete (including the first few hours) postseismic displacements. Future warning systems and coseismic studies should also take these results into consideration for both real-time earthquake characterization and post-processed data fitting. Keeping our individual stations' coseismic time window relatively short and spanning mostly around earthquake shaking ensures the exclusion of long wavelength noise that is typical in high-rate GNSS positioning, mostly due to multipath (Genrich and Bock, 2006). Therefore, a more precise coseismic time window analysis should provide more robust earthquake source parameters that rely on a maximum amplitude relative to a fixed position before the start of earthquake shaking (e.g, PGD: peak-ground-displacement), differentiating the position before and after earthquake shaking (static offset), and for displacement integration (e.g., M_{wg} magnitude estimate described in Chapter 3). This is important for GNSS stations experience low signal-to-noise ratio.

In Chapter 3 we focus on the coseismic phase of the crustal deformation cycle and address the problem of real-time magnitude determination for local tsunami warnings. Magnitude estimates that rely on seismic data alone appear to saturate during earthquakes that are greater than M_w7-8 (Schmedes and Archuleta, 2008; Crowell et al., 2013; Baltay and Hanks, 2014; Trugman et al., 2019). In this collaboration with the Pacific Tsunami Warning Center

(PTWC) in Hawaii, we seek to improve initial tsunami warning messages to populations that are close to the earthquake rupture thus having only a few minutes to respond. We present a new magnitude determination method, M_{wg}, that utilizes the combination of seismic and GNSS data (seismogeodesy). Our approach is based on the M_{wp} method (Tsuboi et al., 1995) that was originally developed for P wave portion of broadband seismic data. To rapidly estimate earthquake magnitude for medium to large thrust events, we use the integration of vertical seismogeodetic displacements as the representation of earthquake seismic moment (Aki and Richards, 2002). By combining high-rate GNSS displacements with strong-motion accelerations at collocated stations, we estimate broadband seismogeodetic displacement and velocity waveforms and circumvent limitations associated with double-integration of regional-to-teleseismic broadband velocity, triple-integration of accelerations, and less precise (and lower rate) GNSS data only. To demonstrate our M_{wg} approach, we replay observed GNSS and strong motion data in real-time simulations for nine tsunamigenic earthquakes in the Pacific basin in the 7.2 $< M_w <$ 9.1 magnitude range. We are able to estimate station-by-station moment magnitude using the far-field P wave term of the earthquake displacement field in a homogeneous elastic medium. Our results show a precision of 0.18 magnitude units for 8 thrust faulting events and 0.32 magnitude units for a single normal faulting event, within 2-3 minutes of earthquake onset time. We compare our M_{wg} with other magnitude determination methods that rely on high-rate GNSS displacements: the Peak-Ground-Displacement (PGD) magnitude scaling, M_{pgd} (Crowell et al., 2013; Melgar et al., 2015a; Ruhl et al., 2019), and W phase Centroid Moment Tensor magnitude, M_{ww} (Kanamori and Rivera, 2008; Riquelme et al., 2016). Rapid results using M_{pgd} tends to be closer to the true magnitude over the first $\sim$1 minute, as it relies on the peak values of displacement records. However, M_{wg} stabilizes and gives more accurate results mostly at 2-3 minutes after rupture initiation. Compared to M_{ww}, M_{wg} converges to a comparable result slightly faster. The timing of these magnitude estimates is expected to vary with different earthquake source time functions. Our approach is earthquake specific in contrast to empirical methods that rely on historical earthquake records.

The major findings from Chapter 3 indicate that our magnitude determination approach is particularly well suited to local tsunami warning systems where response time is essential and to rapid analysis of tsunami earthquakes with complex fault mechanisms. These results motivate the further development of seismogeodetic networks across tectonically active regions. By demonstrating the scenario of interleaved high-rate GNSS and seismic instruments in Chapter 2, we show that we can obtain a coseismic time window for M_{wg} integration at GNSS site locations. Upgrading existing GNSS stations could be done with inexpensive Micro-Electro Mechanical System (MEMS) accelerometers (Saunders et al., 2016; Goldberg and Bock, 2017). We therefore advocate for large-scale seismogeodetic network expansion to mitigate the risks to vulnerable populations and infrastructure. Since most local tsunamis are caused by thrust events, we have not considered strike-slip fault mechanisms in this study although this is certainly of interest for rapid magnitude estimation for earthquake early warning systems such as ShakeAlert (Given et al., 2014; Kohler et al., 2020) in the U.S. West Coast, which includes major strike-slip fault regimes. For that purpose, one should account for the other (S wave) terms in the earthquake displacement field model and use the horizontal seismogeodetic components to obtain a reliable estimate for strike-slip earthquakes.

Although at this point we do not take into account the radiation pattern term in our calculation (see Equation 3.3), our M_{wg} errors do not appear to be spatial correlated with earthquake focal mechanism according to Figure 3.5. Meaning that we do not observe M_{wg} estimate errors associated with the exclusion of radiation pattern terms (A^i in Equation 3.1). To calculate the radiation pattern terms at each GNSS site in real-time, one must assume, a-priori, a focal mechanism for the occurring earthquake. Focal mechanism estimates from first P wave polarities (Hardebeck and Shearer, 2002; Hardebeck and Shearer, 2003) are feasible but only associated with the initial rupture at the epicenter and can often be significantly different from the slip mechanism of the entire rupture (the centroid). For real-time purposes, one can assume that rupture occurs down-dip of the trench from a known model such as *Slab1.0* (Hayes et al., 2012) and use a generalized thrust focal mechanism as an input for radiation pattern term calculations.

Accounting for regional focal mechanisms from past earthquakes and microseismicity may also contribute to real-time estimates of the radiation pattern effect. Peak times from our integrated vertical displacements occur mostly after the expected S wave arrival. We therefore speculate that different seismic phases may contribute to our observed signal. Synthetic tests could be useful to quantify the contribution from each of the terms in the general earthquake displacement field model (Equation 3.1), that might shed some light on the separation of far-, intermediate-, and near-field terms of P and S waves. Peak times of maximum value of integrated displacements can also play a role in the assessment of earthquake source centroid time. Earthquakes causing tsunami waves that are larger than expected based on their magnitude (i.e., tsunami earthquakes) have been recognized to have low rupture speed and longer durations (Kanamori, 1972; Polet and Kanamori, 2000; Ye et al., 2016). Therefore, identification of tsunami earthquakes based on the earthquake centroid time can add crucial information to tsunami warning messages.

In Chapter 4 we turn our attention to the interseismic phase of the crustal deformation cycle. We explore the long-term deformation along the Dead Sea Fault region. There are several challenging aspects to this study; relatively slow slip rate of $\sim$5mm/yr in the area requires a large number of satellite images (and hence interferograms) to resolve, and the mostly north-south striking fault orientation is not ideal. Different studies investigated long-term deformation from both InSAR & GNSS data, including the North Anatolian Fault (Hussain et al., 2018; Weiss et al., 2020), San Andreas Fault (Lindsey et al., 2014a; Tymofyeyeva and Fialko, 2018; Xu et al., 2021), and the Tibetan Plateau (Ou et al., 2022). In the few studies investigating slip rates of the order of millimeters, the faults are mostly oriented east-west, making InSAR Line-of-Sight (LOS) a favorable observation technique (e.g., Haiyuan Fault system, Huang et al., 2019). In our study, the politics in the Middkle East limits scientific communication and collaborations between neighboring countries, resulting in unfavorable GNSS station distribution across the fault. For these reasons, we need to take special care with our InSAR and GNSS analysis to reveal tectonic signals related to the Dead Sea Fault.

We process more than 7 years of Sentinel-1 InSAR data, from 2014 - 2022, together

with ∼200 GNSS stations in the region from both campaign and continuous networks. We use the open source GMTSAR software (Sandwell et al., 2011) to preprocess, align all images to a reference image, and calculating phase difference to generate more than 4000 interferogram pairs. We use these unwrapped phase interferograms to estimate LOS velocities for both ascending and descending satellite tracks using the SBAS algorithm (Berardino et al., 2002). We then tie the InSAR LOS velocities to GNSS data within our study area. Results show some left-lateral deformation across the fault, mostly from the ascending track velocity field. To decompose LOS into east, north, and vertical velocities, we use *gpsgridder* (Sandwell and Wessel, 2016) together with GNSS velocity azimuths. Surface velocities in the north-south component show a clear left-lateral deformation across the two sides of the Sinai and Arabia tectonic plates. Although not the focus of this dissertation, vertical deformation from various sources (e.g., subsurface compaction, sinkholes, mineral extraction) is also apparent in the velocity field. By looking at several profiles across the fault we are able to model reasonable slip rates (5-6mm/yr) and locking depths (10-20km) that are in agreement with other studies (Hamiel and Piatibratova, 2021), with the exception of one non-realistic profile results where GNSS stations are too sparse to constrain the far field velocity away from the fault. While most sections seem to be locked, we found two segments with potential shallow creep of 3-4mm/yr. Previous studies that rely on GNSS data alone also suggest shallow creep at these segments (Hamiel et al., 2016; Hamiel and Piatibratova, 2019).

We further investigate different sections of the Dead Sea Fault by calculating spatial derivatives of the horizontal velocities and calculating the 2^{nd} invariant of the strain rate tensor. Both GNSS and InSAR & GNSS models show strain accumulation along the Dead Sea Fault with as much as ∼100 nanostrain/yr that is in agreement with previous strain rate analysis by regional GNSS (Gomez et al., 2020; Hamiel and Piatibratova, 2021). We do not find evidence for high strain rates in the Carmel Fault System (Figure 4.12). We find strong correlations between high strain areas and creeping sections from our 2D profile modeling. Our combined model highlights areas where the GNSS network is sparse, potentially discovering new areas of

localized shallow deformation and advancing our knowledge of the crustal deformation cycle in this region. We show the value of combining InSAR and GNSS measurements for more detailed surface deformation analysis and modeling, through the better spatial resolution of SAR images, to a north-south striking fault. The combination of ascending and descending tracks is useful for decomposition of LOS motion into mostly vertical and east components, because of the satellite's look angle. To get a better resolution for the north component, one could combine LOS with burst-overlap interferometry (BOI) to resolve the along track direction of motion (Grandin et al., 2016; Yague-Martinez et al., 2019; Li et al., 2021). However, burst-overlap interferometry strongly depends on temporal coherence that is significantly lower north of the Arava Valley in our study area (Figure 5.1). By having hundreds of images and taking careful analysis, BOI can give useful information in decomposition, although covering a smaller portion of the surface. Future directions include addressing vertical deformation that is apparent from our velocity grids into subsurface modeling such as groundwater volume changes and interaction with Dead Sea evaporation rates. Freely available Sentinel-1 InSAR data from the European Space Agency (ESA) were available for this study. we anticipate improved relationships between neighboring countries to allow for GNSS network expansion, contributing to improved seismic hazard mitigation.

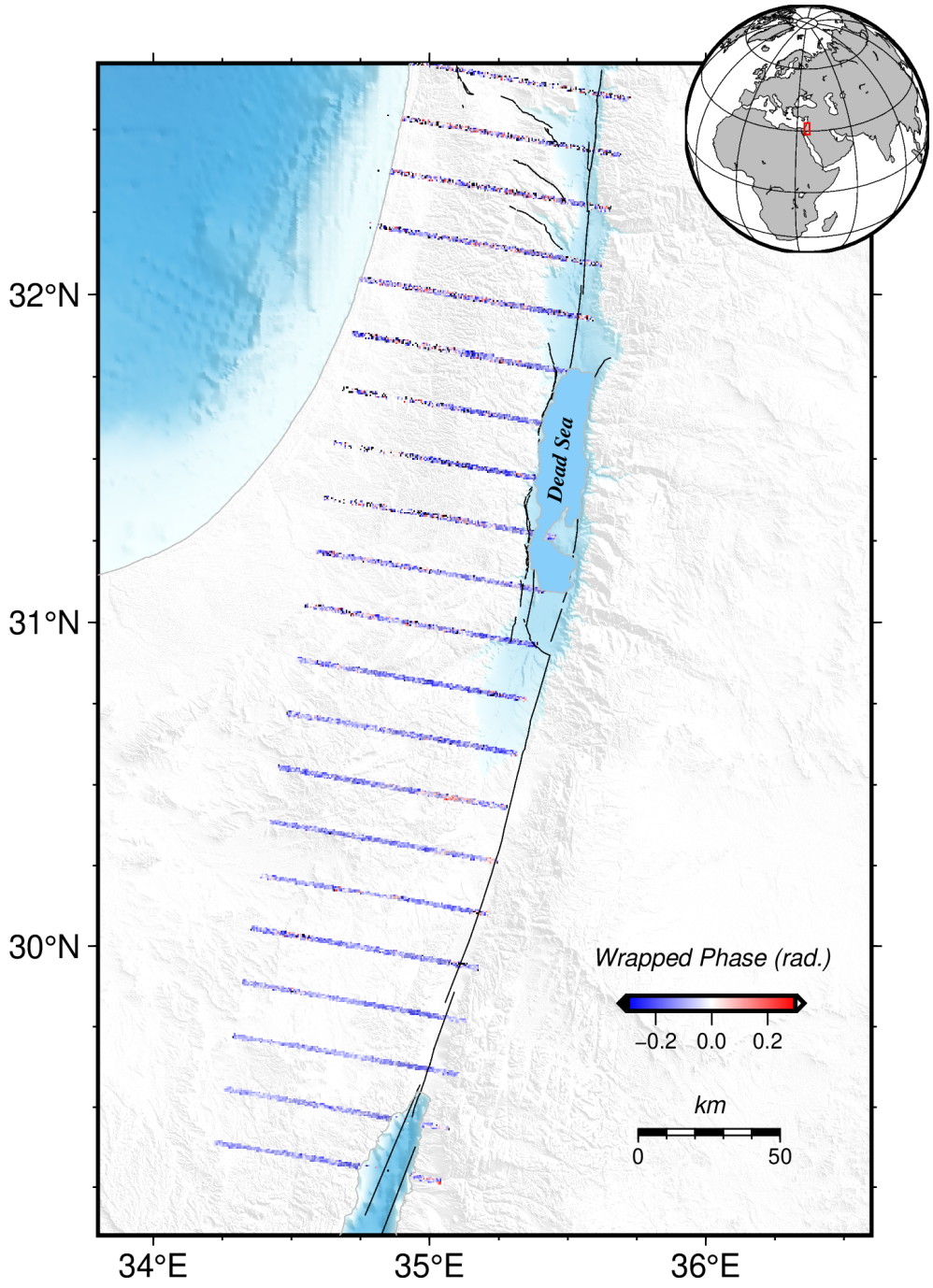

Figure 5.1. Example burst-overlap interferometry from one subswath of descending track. Notice how phase becomes noisy as coherence is going down moving north.

Appendix A

High-Rate GNSS and Seismogeodetic Data Archive for Historical Earthquakes

The usefulness of high-rate GNSS observations for crustal deformation was first demonstrated by Genrich and Bock (1992) for small aperture surveys across the San Andreas fault in Parkfield, California. High-rate real-time positioning with GNSS reference networks was implemented at the same location in Langbein and Bock (2004) and observed coseismic displacements during the 2004 M_w6.0 Parkfield earthquake (Langbein et al., 2005). GNSS networks are now operational in the US (including Alaska and Hawaii), Mexico, Japan, Chile, New Zealand, Greece, Indonesia, Nepal, and in most tectonically active regions on Earth. While daily positioning gives a good measurement of the plate motion and plate boundary deformation in the context of interseismic and postseismic deformation, high-rate ($\geq$1Hz) positioning can measure both static and dynamic motions associated with an earthquake (Larson et al., 2003; Bock et al., 2004; Blewitt et al., 2009), i.e. "GPS Seismology". With the improvements of data communications and computing power in recent decades, many GNSS networks have been upgraded and now include stations that transmit high-rate data in real time. For example, Japan's GEONET (Sagiya et al., 2000; Sagiya, 2004) consists of more than 1200 stations, Network of the Americas (NOTA) with over 1200 real-time stations (Murray et al., 2019), Centro Seismológico Nacional (CSN) network in Chile with over 170 stations (Baez et al., 2018), and NOANET in Greece (Chousianitis et al., 2021).

Real-time products of GNSS positioning can be useful for static fault slip models (e.g., Langbein et al., 2005; Melgar et al., 2013b), rapid centroid moment tensor solutions (Melgar et al., 2012; O'Toole et al., 2013), and regression of Peak-Ground-Displacements versus distance for magnitude determination (Crowell et al., 2013; Melgar et al., 2015a; Ruhl et al., 2019). Therefore, earthquake and tsunami warning systems that rely mostly on seismic data, are shifting towards including GNSS displacements as part of their algorithms: GlarmS (Grapenthin et al., 2014), BEFORES (Minson et al., 2014a) in the Western U.S., G-FAST (Crowell et al., 2018) in Chile, and REGARD (Kawamoto et al., 2016b) in Japan.

Here we present a data archive of historical earthquakes that consists of high-rate GNSS displacements and seismogeodetic waveforms (displacements and velocities). In Chapter 1.2, we discuss the usefulness of the seismogeodetic combination compared to traditional seismic instrumentation. We post-processed continuous GNSS stations recorded in real time during several earthquakes to estimate both dynamic shaking and static offsets. Positioning methods include relative positioning (Langbein and Bock, 2004) using the RTD software (Bock et al., 2000) and Precise Point Positioning (PPP) (Ge et al., 2008; Geng et al., 2012) using the PRIDE PPP-AR software (Geng et al., 2019). Previous data archiving of high-rate GNSS displacements recorded for 29 earthquakes was published by Ruhl et al. (2019). In this analysis, we add records of more recent events (e.g., 2019 M_w7.1 and M6.4 Ridgecrest earthquakes, 2020 M_w7.8 Simeonof earthquake, 2021 M_w8.2 Chignic earthquake) and the seismogeodetic solutions that provide lower noise levels (Saunders et al., 2016) and higher sampling rates for collocated stations (within 5km). We obtain strong-motion accelerometer data from different sources such as the IRIS Web Services (IRIS Data Services), the Center for Engineering Strong Motion Data (CESMD), and the National Research Institute for Earth Science and Disaster Resilience (NIED). For seismogeodetic solutions, we correct for instrument response and follow the procedure described in Bock et al. (2011), with an acceleration multiplier of 10. We list the archived earthquakes in Table A.1, together with each earthquake's magnitude (from the USGS), origin time, location, number of stations (GNSS and collocations), and processing method. Figure A.1

Table A.1. List of historical earthquakes that are archived, with number of records and GNSS processing method.

Name	Date	Country	M_w*	#GNSS	#SG	GNSS Positioning
Anchorage	2018-11-30	USA	7.1	29	6	PPP
Chignic	2021-07-29	USA	8.2	48	6	PPP
El Mayor-Cucapah	2010-04-04	Mexico	7.2	115	33	PPP
Eureka	2014-03-10	USA	6.8	25	0	PPP
Fukushima	2011-04-11	Japan	6.6	172	72	Relative
Kilauea	2018-05-04	USA	6.9	15	4	PPP
Kodiak	2018-01-23	USA	7.9	64	0	PPP
Kumamoto	2016-04-15	Japan	7.0	277	133	Relative
Miyagi	2011-03-09	Japan	7.3	347	120	Relative
Napa	2014-08-24	USA	6.0	117	44	PPP
Parkfield	2004-09-28	USA	6.0	12	0	Relative
Rat Islands	2014-06-23	USA	7.9	4	1	PPP
Ridgecrest	2019-07-06	USA	7.1	490	156	PPP
Ridgecrest Foreshock	2019-07-04	USA	6.4	207	55	PPP
Sand Point	2020-10-19	USA	7.6	13	5	PPP
Simeonof	2020-07-22	USA	7.8	26	5	PPP
Tohoku-oki	2011-03-11	Japan	9.1	1019	345	Relative
Tokachi-oki	2003-09-25	Japan	8.3	366	130	Relative

* Earthquake magnitudes are taken from the United States Geological Survey (USGS).

shows a global map of our archived earthquakes.

Data are stored in both *miniSEED* and *ASCII* formats for user convenience. Figure A.2 shows the structure of the archive inside the main directory of the archive (NASA MEaSUREs - username: anonymous; password: your e-mail address), with supporting information at SOPAC - Seismogeodetic Waveforms). The *EarthquakeTable.txt* file contains information about each event that includes the name of the directory, country, magnitude, origin time, location, number of records, maximum hypocentral distance, and GNSS processing method. The maximum epicentral distance for which we store data is defined manually after inspection of the waveforms and where earthquake shaking diminishes. That is to avoid storing waveforms that are not useful and contain mostly noise. The *Readme.txt* file contains general information about the data archive. Each earthquake's directory consists of three data subdirectories: *GNSS* (high-rate 1Hz displacements), *kdisp* (very high-rate seismogeodetic displacements), and *kvel* (very high-rate seismogeodetic velocities). In addition to the data directories, each earthquake's directory

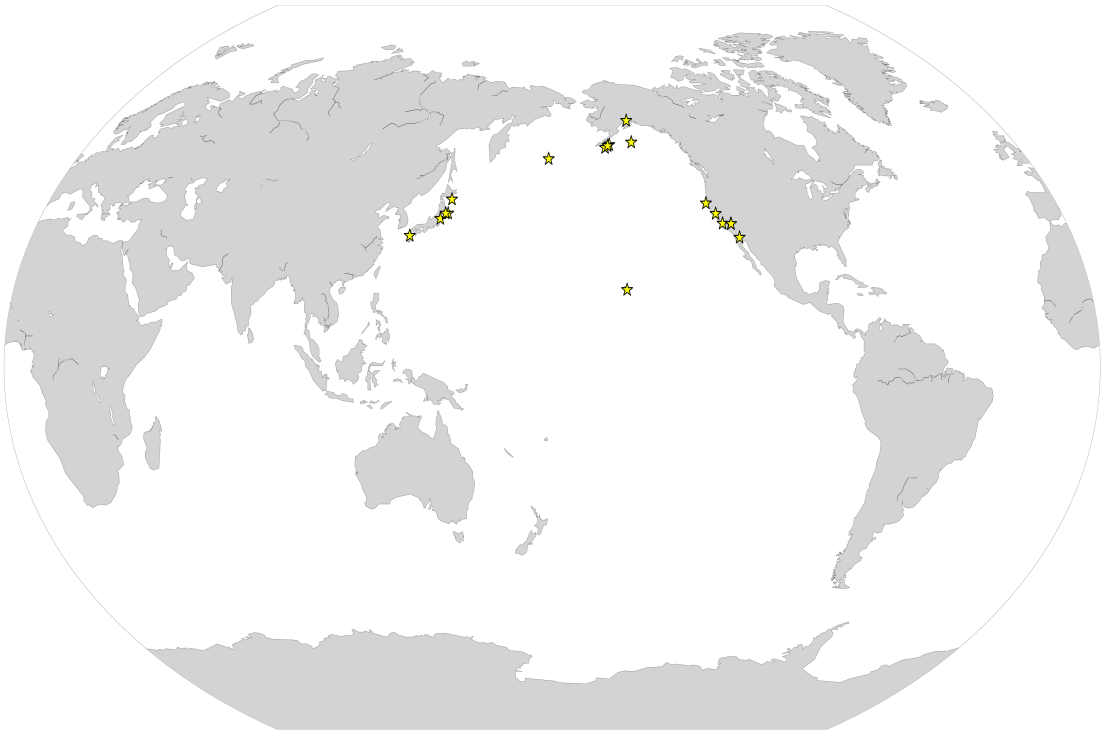

Figure A.1. Historical earthquakes with archived high-rate GNSS displacements and seismo-geodetic waveforms.

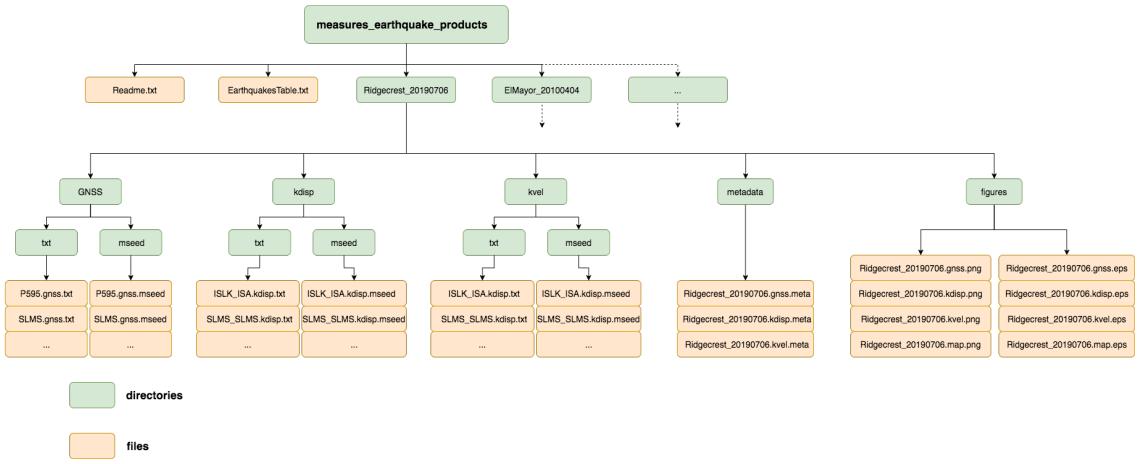

Figure A.2. Data and metadata structure of the archive. Directories are in green, while files are in orange. Each earthquake directory has the same structure as the *Ridgecrest*$_2$0190706*exampleabove*.

contains *metadata* and *figures* subdirectories. Each data type has a metadata file with relevant information such as station location, code, sampling-rate, gain and units. Inside the *figures* subdirectory there are time series plots and a map, to give a sense of the available data and amplitudes of shaking for a particular event. Figures are available in both *png* and *pdf* formats.

We show here an example set of figures for the 2021 M_w8.2 Chignic, Alaska earthquake. Figure A.3 shows a map of available stations with high-rate and seismogeodetic records. In this case, there are 48 1Hz displacement records, 6 out of them with a collocated (or nearby) strong-motion accelerometer, which we combine to estimate seismogeodetic solutions (SG). Figure A.4 shows the high-rate GNSS displacements. We see shaking up to 800km away from the earthquake, and static offsets up to 200km away. Figure A.5 and A.6 shows the seismogeodetic solutions using our Kalman filter for this event (Bock et al., 2011). As expected, not as many stations have a collocated accelerometer and therefore the number of records is significantly smaller. However, these waveforms have reduced noise levels and higher sampling rates (100-200Hz). The length of these records is usually from 1 minute prior to 5-10 minutes after earthquake origin time. The exception to this is Japan data that is triggered automatically by the Japan Meteorological Agency (JMA) and therefore available from 15 seconds before P wave arrival and $\sim$5 minutes

afterwards. Other seismic networks also have triggered records are therefore not available for the entire desirable time window, unlike other seismic networks for which we can obtain continuous data (i.e., Northern California Seismic Network, Berkeley Seismic Network, etc.). The length of GNSS displacements is usually the choice of the data processor. Generally, one can process the whole day of the earthquake or a few hours before and after origin time. Exceptions to that are stations that fail while recording or during earthquake shaking. For example, several GNSS stations from the 2003 M_w8.3 Tokachi-oki earthquake stopped recording during the severe shaking. Several near-field stations, recorded during the 2011 M_w9.1 Tohoku-oki earthquake, are missing data points but continued operating with additional recordings.

The extraction of earthquake source parameters is done using the coseismic time window analysis described in Chapter 2. We estimate static offsets by taking the difference in position before and after the coseismic time window, by averaging 10-seconds of data. The peak-ground-displacement (PGD) is defined as the maximum of the root-mean-square of all three components of displacements within the coseismic time window. For several earthquakes in our archive, we add a *rapid.params* file that contains products such as coseismic time window, static offset for each component, PGD, PGD time, and signal-to-noise (SNR) ratio. We expect that these products and data archive will be beneficial for users in conducting their research and save processing time. We advocate for more high-rate GNSS stations, particularly in real-time, that could contribute for earthquake and tsunami warning systems. This could be done by upgrading existing GNSS stations with an inexpensive Micro-Electro Mechanical System (MEMS) accelerometer directly to the GNSS monument such as described in Saunders et al. (2016) and Goldberg and Bock (2017).

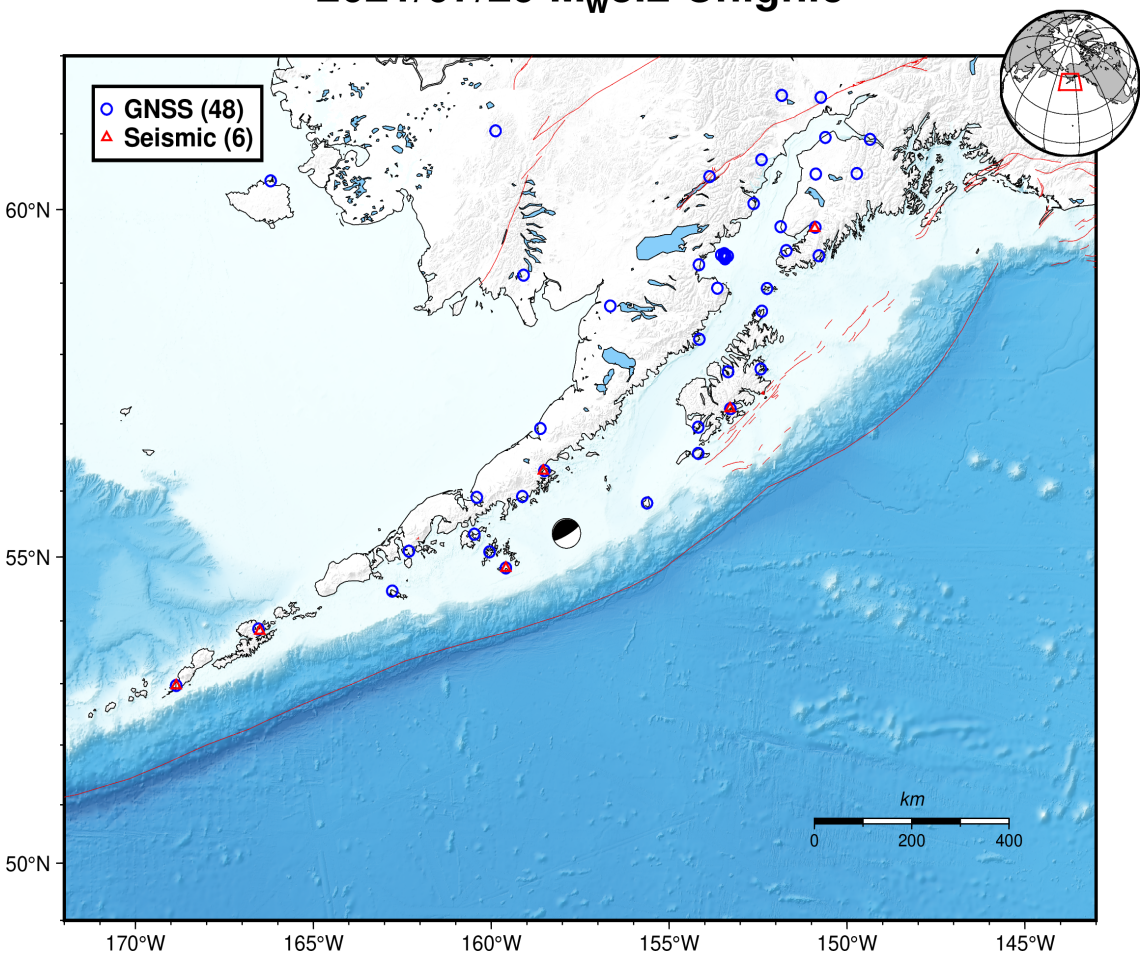

Figure A.3. A map figure showing the available stations for the 2021 M_w8.2 Chignic, Alaska earthquake. High-rate GNSS stations are in blue circles, strong-motion accelerometers (that were used as an input for seismogeodetic solutions) in red triangles. Global faults from Styron and Pagani (2020) denoted by thin red lines.

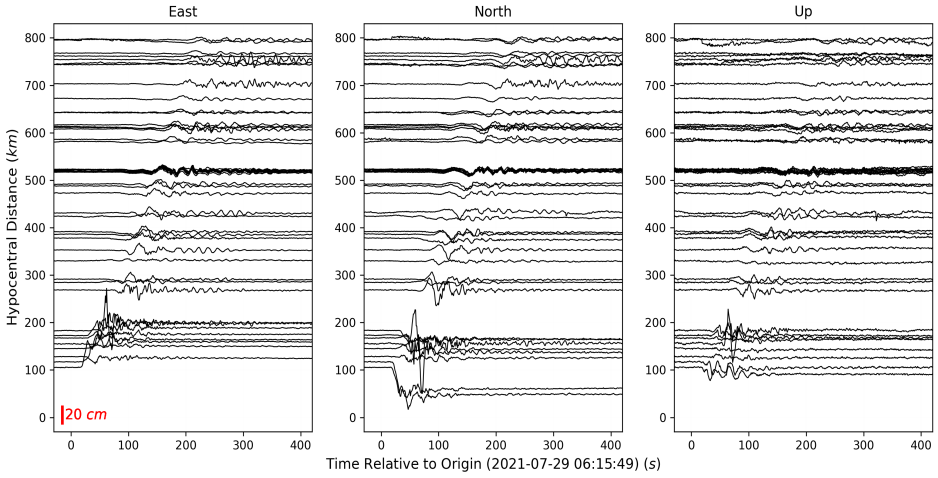

Figure A.4. High-rate (1Hz) GNSS displacements available for the 2021 $M_2$8.2 Chignic, Alaska earthquake.

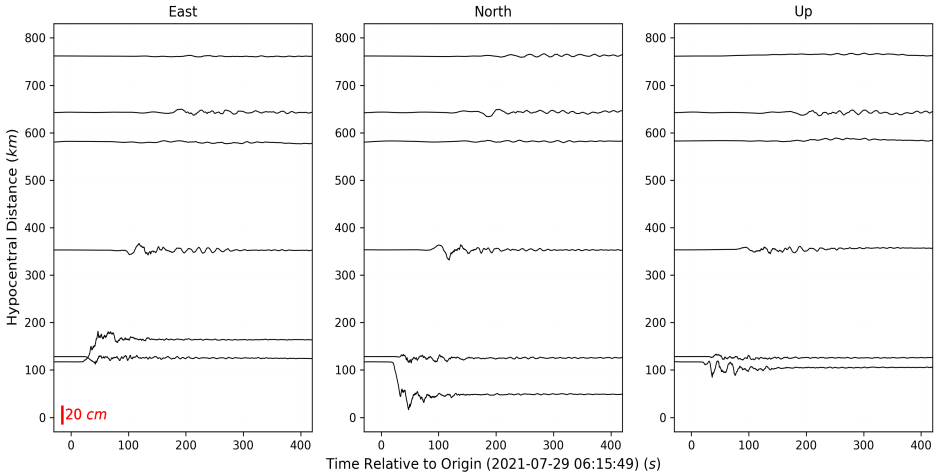

Figure A.5. Very high-rate ($\geq$100Hz) seismogeodetic velocities available for the 2021 M_w8.2 Chignic, Alaska earthquake.

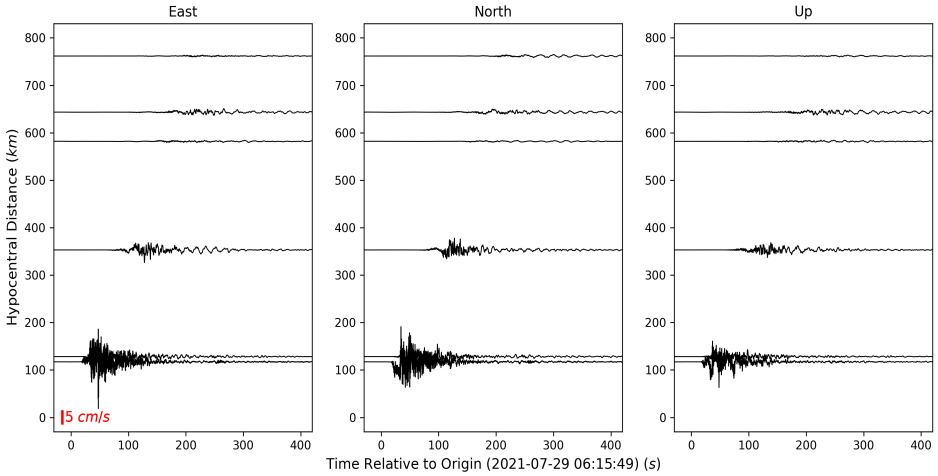

Figure A.6. Very high-rate ($\geq$100Hz) seismogeodetic displacements available for the 2021 M_w8.2 Chignic, Alaska earthquake.

Acknowledgements

Portions of Appendix A are currently in preparation for online repository publication as: Golriz, D., Bock, Y. ”High-Rate GNSS and Seismogeodetic Data Archive for Historical Earthquakes”, in prep. The dissertation author was the primary investigator and author of this

References

Aki, K., & Richards, P. G. (2002). *Quantitative seismology*.

Al-Hanbali, A., Al-Bilbisi, H., & Kondoh, A. (2005). The environmental problem of the dead sea using remote sensing and gis techniques. *Proceedings of the 11th CEReS International Symposium on Remote Sensing*, 13–14.

Allen, R. (1982). Automatic phase pickers: Their present use and future prospects. *Bulletin of the Seismological Society of America*, *72*(6B), S225–S242.

Allen, R. V. (1978). Automatic earthquake recognition and timing from single traces. *Bulletin of the seismological society of America*, *68*(5), 1521–1532.

Allen, R. M., & Kanamori, H. (2003). The potential for earthquake early warning in southern california. *Science*, *300*(5620), 786–789.

Altamimi, Z., Rebischung, P., Métivier, L., & Collilieux, X. (2016). Itrf2014: A new release of the international terrestrial reference frame modeling nonlinear station motions. *Journal of geophysical research: solid earth*, *121*(8), 6109–6131.

Ammon, C. J., Kanamori, H., Lay, T., & Velasco, A. A. (2006). The 17 july 2006 java tsunami earthquake. *Geophysical Research Letters*, *33*(24).

Ansari, H., De Zan, F., & Parizzi, A. (2020). Study of systematic bias in measuring surface deformation with sar interferometry. *IEEE Transactions on Geoscience and Remote Sensing*, *59*(2), 1285–1301.

Aoi, S., Kunugi, T., Nakamura, H., & Fujiwara, H. (2011). Deployment of new strong motion seismographs of k-net and kik-net. In *Earthquake data in engineering seismology* (pp. 167–186). Springer.

Atkinson, G. M., & Boore, D. M. (2006). Earthquake ground-motion prediction equations for eastern north america. *Bulletin of the seismological society of America*, *96*(6), 2181–2205.

Baer, G., Magen, Y., Nof, R., Raz, E., Lyakhovsky, V., & Shalev, E. (2018). Insar measurements and viscoelastic modeling of sinkhole precursory subsidence: Implications for sinkhole formation, early warning, and sediment properties. *Journal of Geophysical Research: Earth Surface*, *123*(4), 678–693.

Baer, G., Sandwell, D., Williams, S., Bock, Y., & Shamir, G. (1999). Coseismic deformation associated with the november 1995, mw= 7.1 nuweiba earthquake, gulf of elat (aqaba), detected by synthetic aperture radar interferometry. *Journal of Geophysical Research: Solid Earth*, *104*(B11), 25221–25232.

Baer, G., Shamir, G., Sandwell, D., & Bock, Y. (2001). Crustal deformation during 6 years spanning the m w= 7.2 1995 nuweiba earthquake, analyzed by interferometric synthetic aperture radar. *Israel Journal of Earth Sciences*, *50*(1).

Baez, J. C., Leyton, F., Troncoso, C., del Campo, F., Bevis, M., Vigny, C., Moreno, M., Simons, M., Kendrick, E., Parra, H., et al. (2018). The chilean gnss network: Current status and progress toward early warning applications. *Seismological Research Letters*, *89*(4), 1546–1554.

Bai, Y., Ye, L., Yamazaki, Y., Lay, T., & Cheung, K. (2018). The 4 may 2018 mw 6.9 hawaii island earthquake and implications for tsunami hazards. *Geophysical Research Letters*, *45*(20), 11–040.

Bakun, W., Aagaard, B., Dost, B., Ellsworth, W., Hardebeck, J., Harris, R., Ji, C., Johnston, M., Langbein, J., Lienkaemper, J., et al. (2005). Implications for prediction and hazard assessment from the 2004 parkfield earthquake. *Nature*, *437*(7061), 969–974.

Baltay, A. S., & Hanks, T. C. (2014). Understanding the magnitude dependence of pga and pgv in nga-west 2 data. *Bulletin of the Seismological Society of America*, *104*(6), 2851–2865.

Barbot, S., & Fialko, Y. (2010). A unified continuum representation of post-seismic relaxation mechanisms: Semi-analytic models of afterslip, poroelastic rebound and viscoelastic flow. *Geophysical Journal International*, *182*(3), 1124–1140.

Barbot, S., Fialko, Y., & Bock, Y. (2009). Postseismic deformation due to the mw 6.0 2004 parkfield earthquake: Stress-driven creep on a fault with spatially variable rate-and-state friction parameters. *Journal of Geophysical Research: Solid Earth*, *114*(B7).

Barrientos, S., et al. (2018). The seismic network of chile. *Seismological Research Letters*, *89*(2A), 467–474.

Beavan, J., Motagh, M., Fielding, E. J., Donnelly, N., & Collett, D. (2012). Fault slip models of the 2010–2011 canterbury, new zealand, earthquakes from geodetic data and observations of postseismic ground deformation. *New Zealand Journal of Geology and Geophysics*, *55*(3), 207–221.

Berardino, P., Fornaro, G., Lanari, R., & Sansosti, E. (2002). A new algorithm for surface deformation monitoring based on small baseline differential sar interferograms. *IEEE Transactions on geoscience and remote sensing*, *40*(11), 2375–2383.

Beroza, G. C., & Ide, S. (2011). Slow earthquakes and nonvolcanic tremor. *Annual review of Earth and planetary sciences*, *39*, 271–296.

Bhattacharya, P., & Viesca, R. C. (2019). Fluid-induced aseismic fault slip outpaces pore-fluid migration. *Science*, *364*(6439), 464–468.

Biggs, J., & Wright, T. J. (2020). How satellite insar has grown from opportunistic science to routine monitoring over the last decade. *Nature Communications*, *11*(1), 1–4.

Bird, P., & Kagan, Y. Y. (2004). Plate-tectonic analysis of shallow seismicity: Apparent boundary width, beta, corner magnitude, coupled lithosphere thickness, and coupling in seven tectonic settings. *Bulletin of the Seismological Society of America*, *94*(6), 2380–2399.

Blewitt, G., Hammond, W. C., Kreemer, C., Plag, H.-P., Stein, S., & Okal, E. (2009). Gps for real-time earthquake source determination and tsunami warning systems. *Journal of Geodesy*, *83*(3), 335–343.

Blewitt, G., Kreemer, C., Hammond, W. C., Plag, H.-P., Stein, S., & Okal, E. (2006). Rapid determination of earthquake magnitude using gps for tsunami warning systems. *Geophysical Research Letters*, *33*(11).

Bock, Y., & Melgar, D. (2016). Physical applications of gps geodesy: A review. *Reports on Progress in Physics*, *79*(10), 106801.

Bock, Y., Melgar, D., & Crowell, B. W. (2011). Real-time strong-motion broadband displacements from collocated gps and accelerometers. *Bulletin of the Seismological Society of America*, *101*(6), 2904–2925.

Bock, Y., Nikolaidis, R. M., de Jonge, P. J., & Bevis, M. (2000). Instantaneous geodetic positioning at medium distances with the global positioning system. *Journal of Geophysical Research: Solid Earth*, *105*(B12), 28223–28253.

Bock, Y., Prawirodirdjo, L., & Melbourne, T. I. (2004). Detection of arbitrarily large dynamic ground motions with a dense high-rate gps network. *Geophysical Research Letters*, *31*(6).

Bock, Y., & Wdowinski, S. (2020). Gnss geodesy in geophysics, natural hazards, climate, and the environment. *Position, Navigation, and Timing Technologies in the 21st Century: Integrated Satellite Navigation, Sensor Systems, and Civil Applications*, *1*, 741–820.

Boore, D. M. (2001). Effect of baseline corrections on displacements and response spectra for several recordings of the 1999 chi-chi, taiwan, earthquake. *Bulletin of the Seismological Society of America*, *91*(5), 1199–1211.

Boore, D. M., Stephens, C. D., & Joyner, W. B. (2002). Comments on baseline correction of digital strong-motion data: Examples from the 1999 hector mine, california, earthquake. *Bulletin of the Seismological Society of America*, *92*(4), 1543–1560.

Brooks, B. A., Murray, J., Svarc, J., Phillips, E., Turner, R., Murray, M., Ericksen, T., Wang, K., Minson, S., Burgmann, R., et al. (2020). Rapid geodetic observations of spatiotemporally varying postseismic deformation following the ridgecrest earthquake sequence: The us geological survey response. *Seismological Research Letters*, *91*(4), 2108–2123.

Bruhat, L., Barbot, S., & Avouac, J.-P. (2011). Evidence for postseismic deformation of the lower crust following the 2004 mw6. 0 parkfield earthquake. *Journal of Geophysical Research: Solid Earth*, *116*(B8).

Bryant, E. (2008). *The underrated hazard*. Springer.

Bürgmann, R., Thatcher, W., & Bickford, M. (2013). Space geodesy: A revolution in crustal deformation measurements of tectonic processes. *Geol. Soc. Am. Spec. Pap.*, *500*, 397–430.

Cabral-Cano, E., Pérez-Campos, X., Márquez-Azúa, B., Sergeeva, M., Salazar-Tlaczani, L., DeMets, C., Adams, D., Galetzka, J., Hodgkinson, K., Feaux, K., et al. (2018). Tlalocnet: A continuous gps-met backbone in mexico for seismotectonic and atmospheric research. *Seismological Research Letters*, *89*(2A), 373–381.

Castro-Perdomo, N., Viltres, R., Masson, F., Klinger, Y., Liu, S., Dhahry, M., Ulrich, P., Bernard, J.-D., Matrau, R., Alothman, A., et al. (2021). Interseismic deformation in the gulf of aqaba from gps measurements. *Geophysical Journal International*.

Chen, C. W., & Zebker, H. A. (2002). Phase unwrapping for large sar interferograms: Statistical segmentation and generalized network models. *IEEE Transactions on Geoscience and Remote Sensing*, *40*(8), 1709–1719.

Chousianitis, K., Papanikolaou, X., Drakatos, G., & Tselentis, G.-A. (2021). Noanet: A continuously operating gnss network for solid-earth sciences in greece. *Seismological Research Letters*, *92*(3), 2050–2064.

Cochran, E. S., Kohler, M. D., Given, D. D., Guiwits, S., Andrews, J., Meier, M.-A., Ahmad, M., Henson, I., Hartog, R., & Smith, D. (2018). Earthquake early warning shakealert system: Testing and certification platform. *Seismological Research Letters*, *89*(1), 108–117.

Crowell, B. W., & Melgar, D. (2020). Slipping the shumagin gap: A kinematic coseismic and early afterslip model of the mw 7.8 simeonof island, alaska, earthquake. *Geophysical Research Letters*, *47*(19), e2020GL090308.

Crowell, B. W., Melgar, D., Bock, Y., Haase, J. S., & Geng, J. (2013). Earthquake magnitude scaling using seismogeodetic data. *Geophysical Research Letters*, *40*(23), 6089–6094.

Crowell, B. W., Schmidt, D. A., Bodin, P., Vidale, J. E., Baker, B., Barrientos, S., & Geng, J. (2018). G-fast earthquake early warning potential for great earthquakes in chile. *Seismological Research Letters*, *89*(2A), 542–556.

Crowell, B. W., Schmidt, D. A., Bodin, P., Vidale, J. E., Gomberg, J., Renate Hartog, J., Kress, V. C., Melbourne, T. I., Santillan, M., Minson, S. E., et al. (2016). Demonstration of the cascadia g-fast geodetic earthquake early warning system for the nisqually, washington, earthquake. *Seismological Research Letters*, *87*(4), 930–943.

DeMets, C., Gordon, R. G., & Argus, D. F. (2010). Geologically current plate motions. *Geophysical journal international*, *181*(1), 1–80.

DeVries, P. M., & Meade, B. J. (2013). Earthquake cycle deformation in the tibetan plateau with a weak mid-crustal layer. *Journal of Geophysical Research: Solid Earth*, *118*(6), 3101–3111.

Ding, K., Freymueller, J. T., Wang, Q., & Zou, R. (2015). Coseismic and early postseismic deformation of the 5 january 2013 m w 7.5 craig earthquake from static and kinematic gps solutions. *Bulletin of the Seismological Society of America*, *105*(2B), 1153–1164.

Dittmann, T., Hodgkinson, K., Morton, J., Mencin, D., & Mattioli, G. S. (2022). Comparing sensitivities of geodetic processing methods for rapid earthquake magnitude estimation. *Seismological Society of America*, *93*(3), 1497–1509.

Dziewonski, A. M., Chou, T.-A., & Woodhouse, J. H. (1981). Determination of earthquake source parameters from waveform data for studies of global and regional seismicity. *Journal of Geophysical Research: Solid Earth*, *86*(B4), 2825–2852.

Ekström, G., Nettles, M., & Dziewoński, A. (2012). The global cmt project 2004–2010: Centroid-moment tensors for 13,017 earthquakes. *Physics of the Earth and Planetary Interiors*, *200*, 1–9.

Elbanna, A., Abdelmeguid, M., Ma, X., Amlani, F., Bhat, H. S., Synolakis, C., & Rosakis, A. J. (2021). Anatomy of strike-slip fault tsunami genesis. *Proceedings of the National Academy of Sciences*, *118*(19), e2025632118.

Ellenblum, R., Marco, S., Kool, R., Davidovitch, U., Porat, R., & Agnon, A. (2015). Archaeological record of earthquake ruptures in tell ateret, the dead sea fault. *Tectonics*, *34*(10), 2105–2117.

Emore, G. L., Haase, J. S., Choi, K., Larson, K. M., & Yamagiwa, A. (2007). Recovering seismic displacements through combined use of 1-hz gps and strong-motion accelerometers. *Bulletin of the Seismological Society of America*, *97*(2), 357–378.

Ergintav, S., McClusky, S., Hearn, E., Reilinger, R., Cakmak, R., Herring, T., Ozener, H., Lenk, O., & Tari, E. (2009). Seven years of postseismic deformation following the 1999, m= 7.4 and m= 7.2, izmit-düzce, turkey earthquake sequence. *Journal of Geophysical Research: Solid Earth*, *114*(B7).

Evans, J. R., & Allen, S. S. (1983). A teleseism-specific detection algorithm for single short-period traces. *Bulletin of the Seismological Society of America*, *73*(4), 1173–1186.

Fan, W., Barbour, A. J., Cochran, E. S., & Lin, G. (2021). Characteristics of frequent dynamic triggering of microearthquakes in southern california. *Journal of Geophysical Research: Solid Earth*, *126*(1), e2020JB020820.

Fan, W., Okuwaki, R., Barbour, A. J., Huang, Y., Lin, G., & Cochran, E. S. (2022). Fast rupture of the 2009 m w 6.9 canal de ballenas earthquake in the gulf of california dynamically triggers seismicity in california. *Geophysical Journal International*, *230*(1), 528–541.

Fan, W., & Shearer, P. M. (2016). Local near instantaneously dynamically triggered aftershocks of large earthquakes. *Science*, *353*(6304), 1133–1136.

Feng, W., Samsonov, S., Qiu, Q., Wang, Y., Zhang, P., Li, T., & Zheng, W. (2020). Orthogonal fault rupture and rapid postseismic deformation following 2019 ridgecrest, california, earthquake sequence revealed from geodetic observations. *Geophysical Research Letters*, *47*(5), e2019GL086888.

Fialko, Y. (2004a). Evidence of fluid-filled upper crust from observations of postseismic deformation due to the 1992 mw7. 3 landers earthquake. *Journal of Geophysical Research: Solid Earth*, *109*(B8).

Fialko, Y. (2004b). Probing the mechanical properties of seismically active crust with space geodesy: Study of the coseismic deformation due to the 1992 mw7. 3 landers (southern california) earthquake. *Journal of Geophysical Research: Solid Earth*, *109*(B3).

Fialko, Y., Sandwell, D., Simons, M., & Rosen, P. (2005). Three-dimensional deformation caused by the bam, iran, earthquake and the origin of shallow slip deficit. *Nature*, *435*(7040), 295–299.

Freed, A. M. (2007). Afterslip (and only afterslip) following the 2004 parkfield, california, earthquake. *Geophysical Research Letters*, *34*(6).

Fukushima, Y., Takada, Y., & Hashimoto, M. (2013). Complex ruptures of the 11 april 2011 mw 6.6 iwaki earthquake triggered by the 11 march 2011 mw 9.0 tohoku earthquake, japan-complex ruptures of mw 6.6 iwaki earthquake triggered by mw 9.0 tohoku earthquake. *Bulletin of the Seismological Society of America*, *103*(2B), 1572–1583.

Ge, M., Gendt, G., Rothacher, M. a., Shi, C., & Liu, J. (2008). Resolution of gps carrier-phase ambiguities in precise point positioning (ppp) with daily observations. *Journal of geodesy*, *82*(7), 389–399.

Geng, J., Bock, Y., Melgar, D., Crowell, B. W., & Haase, J. S. (2013). A new seismogeodetic approach applied to gps and accelerometer observations of the 2012 brawley seismic swarm: Implications for earthquake early warning. *Geochemistry, Geophysics, Geosystems*, *14*(7), 2124–2142.

Geng, J., Chen, X., Pan, Y., Mao, S., Li, C., Zhou, J., & Zhang, K. (2019). Pride ppp-ar: An open-source software for gps ppp ambiguity resolution. *GPS Solutions*, *23*(4), 1–10.

Geng, J., Shi, C., Ge, M., Dodson, A. H., Lou, Y., Zhao, Q., & Liu, J. (2012). Improving the estimation of fractional-cycle biases for ambiguity resolution in precise point positioning. *Journal of Geodesy*, *86*(8), 579–589.

Genrich, J. F., & Bock, Y. (1992). Rapid resolution of crustal motion at short ranges with the global positioning system. *Journal of Geophysical Research: Solid Earth*, *97*(B3), 3261–3269.

Genrich, J. F., & Bock, Y. (2006). Instantaneous geodetic positioning with 10–50 hz gps measurements: Noise characteristics and implications for monitoring networks. *Journal of Geophysical Research: Solid Earth*, *111*(B3).

Given, D. D., Cochran, E. S., Heaton, T., Hauksson, E., Allen, R., Hellweg, P., Vidale, J., & Bodin, P. (2014). *Technical implementation plan for the shakealert production system: An earthquake early warning system for the west coast of the united states*. US Department of the Interior, US Geological Survey Reston, VA.

Goldberg, D. E., Melgar, D., Sahakian, V., Thomas, A., Xu, X., Crowell, B., & Geng, J. (2020). Complex rupture of an immature fault zone: A simultaneous kinematic model of the 2019 ridgecrest, ca earthquakes. *Geophysical Research Letters*, *47*(3), e2019GL086382.

Goldberg, D., & Bock, Y. (2017). Self-contained local broadband seismogeodetic early warning system: Detection and location. *Journal of Geophysical Research: Solid Earth*, *122*(4), 3197–3220.

Goldberg, D., Melgar, D., Bock, Y., & Allen, R. (2018). Geodetic observations of weak determinism in rupture evolution of large earthquakes. *Journal of Geophysical Research: Solid Earth*, *123*(11), 9950–9962.

Gomez, F., Cochran, W. J., Yassminh, R., Jaafar, R., Reilinger, R., Floyd, M., King, R. W., & Barazangi, M. (2020). Fragmentation of the sinai plate indicated by spatial variation in present-day slip rate along the dead sea fault system. *Geophysical Journal International*, *221*(3), 1913–1940.

Gonzalez-Ortega, A., Fialko, Y., Sandwell, D., Alejandro Nava-Pichardo, F., Fletcher, J., Gonzalez Garcia, J., Lipovsky, B., Floyd, M., & Funning, G. (2014). El mayor-cucapah (mw 7.2) earthquake: Early near-field postseismic deformation from insar and gps observations. *Journal of Geophysical Research: Solid Earth*, *119*(2), 1482–1497.

Graizer, V. (1979). Determination of the true ground displacement by using strong motion records. *Izv. USSR Acad. Sci., Physics Solid Earth*, *15*, 875–885.

Grandin, R., Klein, E., Métois, M., & Vigny, C. (2016). Three-dimensional displacement field of the 2015 mw8. 3 illapel earthquake (chile) from across-and along-track sentinel-1 tops interferometry. *Geophysical Research Letters*, *43*(6), 2552–2561.

Grapenthin, R., Johanson, I. A., & Allen, R. M. (2014). Operational real-time gps-enhanced earthquake early warning. *Journal of Geophysical Research: Solid Earth*, *119*(10), 7944–7965.

Gualandi, A., Liu, Z., & Rollins, C. (2020). Post-large earthquake seismic activities mediated by aseismic deformation processes. *Earth and Planetary Science Letters*, *530*, 115870.

Haines, A. J., Dimitrova, L. L., Wallace, L. M., & Williams, C. A. (2015). *Enhanced surface imaging of crustal deformation: Obtaining tectonic force fields using gps data*. Springer.

Hamiel, Y., Amit, R., Begin, Z., Marco, S., Katz, O., Salamon, A., Zilberman, E., & Porat, N. (2009). The seismicity along the dead sea fault during the last 60,000 years. *Bulletin of the Seismological Society of America*, *99*(3), 2020–2026.

Hamiel, Y., Masson, F., Piatibratova, O., & Mizrahi, Y. (2018a). Gps measurements of crustal deformation across the southern arava valley section of the dead sea fault and implications to regional seismic hazard assessment. *Tectonophysics*, *724*, 171–178.

Hamiel, Y., & Piatibratova, O. (2019). Style and distribution of slip at the margin of a pull-apart structure: Geodetic investigation of the southern dead sea basin. *Journal of Geophysical Research: Solid Earth*, *124*(11), 12023–12033.

Hamiel, Y., & Piatibratova, O. (2021). Spatial variations of slip and creep rates along the southern and central dead sea fault and the carmel–gilboa fault system. *Journal of Geophysical Research: Solid Earth*, *126*(9), e2020JB021585.

Hamiel, Y., Piatibratova, O., & Mizrahi, Y. (2016). Creep along the northern jordan valley section of the dead sea fault. *Geophysical Research Letters*, *43*(6), 2494–2501.

Hamiel, Y., Piatibratova, O., Mizrahi, Y., Nahmias, Y., & Sagy, A. (2018b). Crustal deformation across the jericho valley section of the dead sea fault as resolved by detailed field and geodetic observations. *Geophysical Research Letters*, *45*(7), 3043–3050.

Hao, J., Ji, C., & Yao, Z. (2017). Slip history of the 2016 mw 7.0 kumamoto earthquake: Intraplate rupture in complex tectonic environment. *Geophysical Research Letters*, *44*(2), 743–750.

Hardebeck, J. L., & Shearer, P. M. (2002). A new method for determining first-motion focal mechanisms. *Bulletin of the Seismological Society of America*, *92*(6), 2264–2276.

Hardebeck, J. L., & Shearer, P. M. (2003). Using s/p amplitude ratios to constrain the focal mechanisms of small earthquakes. *Bulletin of the Seismological Society of America*, *93*(6), 2434–2444.

Harris, R. A. (2017). Large earthquakes and creeping faults. *Reviews of Geophysics*, *55*(1), 169–198.

Hatzfeld, D., Ziazia, M., Kementzetzidou, D., Hatzidimitriou, P., Panagiotopoulos, D., Makropoulos, K., Papadimitriou, P., & Deschamps, A. (1999). Microseismicity and focal mechanisms at the western termination of the north anatolian fault and their implications for continental tectonics. *Geophysical Journal International*, *137*(3), 891–908.

Hayes, G. P. (2017). The finite, kinematic rupture properties of great-sized earthquakes since 1990. *Earth and Planetary Science Letters*, *468*, 94–100.

Hayes, G. P., Wald, D. J., & Johnson, R. L. (2012). Slab1. 0: A three-dimensional model of global subduction zone geometries. *Journal of Geophysical Research: Solid Earth*, *117*(B1).

Hetland, E., & Hager, B. H. (2006). The effects of rheological layering on post-seismic deformation. *Geophysical Journal International*, *166*(1), 277–292.

Hirshorn, B. (2007). The pacific tsunami warning center response to the mw6. 7 kiholo bay earthquake and lessons for the future. *Seism Res Lett*, *78*, 299.

Hirshorn, B., Weinstein, S., & Meyers, R. (2009). Earthquake source parameters, rapid estimates for tsunami warning. *Encyclopedia of Complexity and Systems Science*, *3*, 2–657.

Hirshorn, B., Weinstein, S., Wang, D., Koyanagi, K., Becker, N., & McCreery, C. (2021). Earthquake source parameters: Rapid estimates for tsunami forecasts and warnings. In *Complexity in tsunamis, volcanoes, and their hazards* (pp. 299–333). Springer.

Hodgkinson, K. M., Mencin, D. J., Feaux, K., Sievers, C., & Mattioli, G. S. (2020). Evaluation of earthquake magnitude estimation and event detection thresholds for real-time gnss networks: Examples from recent events captured by the network of the americas. *Seismological Research Letters*, *91*(3), 1628–1645.

Hofstetter, A., Van Eck, T., & Shapira, A. (1996). Seismic activity along fault branches of the dead sea-jordan transform system: The carmel-tirtza fault system. *Tectonophysics*, *267*(1-4), 317–330.

Hoshiba, M., & Ozaki, T. (2014). Earthquake early warning and tsunami warning of the japan meteorological agency, and their performance in the 2011 off the pacific coast of tohoku earthquake (mw9.0). In *Early warning for geological disasters* (pp. 1–28). Springer.

Hötzl, H., Möller, P., & Rosenthal, E. (2008). *The water of the jordan valley: Scarcity and deterioration of groundwater and its impact on the regional development*. Springer Science & Business Media.

Huang, Y., Qiao, X., Freymueller, J. T., Wang, Q., Yang, S., Tan, K., & Zhao, B. (2019). Fault geometry and slip distribution of the 2013 mw 6.6 lushan earthquake in china constrained by gps, insar, leveling, and strong motion data. *Journal of Geophysical Research: Solid Earth*, *124*(7), 7341–7353.

Hussain, E., Wright, T. J., Walters, R. J., Bekaert, D. P., Lloyd, R., & Hooper, A. (2018). Constant strain accumulation rate between major earthquakes on the north anatolian fault. *Nature communications*, *9*(1), 1–9.

Im, K., Elsworth, D., Marone, C., & Leeman, J. (2017). The impact of frictional healing on stick-slip recurrence interval and stress drop: Implications for earthquake scaling. *Journal of Geophysical Research: Solid Earth*, *122*(12), 10–102.

Ito, T., Ozawa, K., Watanabe, T., & Sagiya, T. (2011). Slip distribution of the 2011 off the pacific coast of tohoku earthquake inferred from geodetic data. *Earth, planets and space*, *63*(7), 627–630.

Iwan, W. D., Moser, M. A., & Peng, C.-Y. (1985). Some observations on strong-motion earthquake measurement using a digital accelerograph. *Bulletin of the Seismological Society of America*, *75*(5), 1225–1246.

Jacobs, A., Sandwell, D., Fialko, Y., & Sichoix, L. (2002). The 1999 (m w 7.1) hector mine, california, earthquake: Near-field postseismic deformation from ers interferometry. *Bulletin of the Seismological Society of America*, *92*(4), 1433–1442.

Jiang, J., Bock, Y., & Klein, E. (2021). Coevolving early afterslip and aftershock signatures of a san andreas fault rupture. *Science Advances*, *7*(15), eabc1606.

Jiang, J., & Lapusta, N. (2017). Connecting depth limits of interseismic locking, microseismicity, and large earthquakes in models of long-term fault slip. *Journal of Geophysical Research: Solid Earth*, *122*(8), 6491–6523.

Jin, Z., & Fialko, Y. (2020). Finite slip models of the 2019 ridgecrest earthquake sequence constrained by space geodetic data and aftershock locations. *Bulletin of the Seismological Society of America*, *110*(4), 1660–1679.

Johanson, I. A., Fielding, E. J., Rolandone, F., & Bürgmann, R. (2006). Coseismic and postseismic slip of the 2004 parkfield earthquake from space-geodetic data. *Bulletin of the Seismological Society of America*, *96*(4B), S269–S282.

Johnson, C. E., Bittenbinder, A., Bogaert, B., Dietz, L., & Kohler, W. (1995). Earthworm: A flexible approach to seismic network processing. *Iris newsletter*, *14*(2), 1–4.

Johnson, C. E., Lindh, A., & Hirshorn, B. (1997). Robust regional phase association.

Jolivet, R., Simons, M., Duputel, Z., Olive, J.-A., Bhat, H., & Bletery, Q. (2020). Interseismic loading of subduction megathrust drives long-term uplift in northern chile. *Geophysical Research Letters*, *47*(8), e2019GL085377.

Jónsson, S., Segall, P., Pedersen, R., & Björnsson, G. (2003). Post-earthquake ground movements correlated to pore-pressure transients. *Nature*, *424*(6945), 179–183.

Kanamori, H. (1972). Mechanism of tsunami earthquakes. *Physics of the earth and planetary interiors*, *6*(5), 346–359.

Kanamori, H. (1977). The energy release in great earthquakes. *Journal of geophysical research*, *82*(20), 2981–2987.

Kanamori, H. (1993). W phase. *Geophysical research letters*, *20*(16), 1691–1694.

Kanamori, H., & Rivera, L. (2008). Source inversion ofwphase: Speeding up seismic tsunami warning. *Geophysical Journal International*, *175*(1), 222–238.

Kaneko, Y., Fialko, Y., Sandwell, D. T., Tong, X., & Furuya, M. (2013). Interseismic deformation and creep along the central section of the north anatolian fault (turkey): Insar observations and implications for rate-and-state friction properties. *Journal of Geophysical Research: Solid Earth*, *118*(1), 316–331.

Käufl, P., Valentine, A. P., O'Toole, T. B., & Trampert, J. (2014). A framework for fast probabilistic centroid-moment-tensor determination—inversion of regional static displacement measurements. *Geophysical Journal International*, *196*(3), 1676–1693.

Kawamoto, S., Hiyama, Y., Kai, R., Suga, F., Yamaguchi, K., Furuya, T., Abe, S., & Takamatsu, N. (2016a). Crustal deformation caused by the 2016 kumamoto earthquake revealed by geonet. *Bulletin of the Geospatial Information Authority of Japan*, *64*, 27–33.

Kawamoto, S., Hiyama, Y., Ohta, Y., & Nishimura, T. (2016b). First result from the geonet real-time analysis system (regard): The case of the 2016 kumamoto earthquakes. *Earth, Planets and Space*, *68*(1), 1–12.

Kennet, B. (1991). Iaspei 1991 seismological tables. *Terra Nova*, *3*(2), 122–122.

Kido, M., Osada, Y., Fujimoto, H., Hino, R., & Ito, Y. (2011). Trench-normal variation in observed seafloor displacements associated with the 2011 tohoku-oki earthquake. *Geophysical Research Letters*, *38*(24).

Kikuchi, M., & Ishida, M. (1993). Source retrieval for deep local earthquakes with broadband records. *Bulletin of the Seismological Society of America*, *83*(6), 1855–1870.

Klein, E., Bock, Y., Xu, X., Sandwell, D. T., Golriz, D., Fang, P., & Su, L. (2019). Transient deformation in california from two decades of gps displacements: Implications for a three-dimensional kinematic reference frame. *Journal of Geophysical Research: Solid Earth*, *124*(11), 12189–12223.

Kobayashi, T., Tobita, M., Koarai, M., Okatani, T., Suzuki, A., Noguchi, Y., Yamanaka, M., & Miyahara, B. (2012). Insar-derived crustal deformation and fault models of normal faulting earthquake (m j 7.0) in the fukushima-hamadori area. *Earth, planets and space*, *64*(12), 1209–1221.

Kohler, M. D., Smith, D. E., Andrews, J., Chung, A. I., Hartog, R., Henson, I., Given, D. D., de Groot, R., & Guiwits, S. (2020). Earthquake early warning shakealert 2.0: Public rollout. *Seismological Research Letters*, *91*(3), 1763–1775.

Kouba, J., Lahaye, F., & Tétreault, P. (2017). Precise point positioning. In *Springer handbook of global navigation satellite systems* (pp. 723–751). Springer.

Kreemer, C., Blewitt, G., & Klein, E. C. (2014). A geodetic plate motion and global strain rate model. *Geochemistry, Geophysics, Geosystems*, *15*(10), 3849–3889.

Kreemer, C., Holt, W. E., & Haines, A. J. (2002). The global moment rate distribution within plate boundary zones. *Plate boundary zones*, *30*, 173–190.

Kreemer, C., Holt, W. E., & Haines, A. J. (2003). An integrated global model of present-day plate motions and plate boundary deformation. *Geophysical Journal International*, *154*(1), 8–34.

Kurzon, I., Nof, R. N., Laporte, M., Lutzky, H., Polozov, A., Zakosky, D., Shulman, H., Goldenberg, A., Tatham, B., & Hamiel, Y. (2020). The “truaa” seismic network: Upgrading the israel seismic network—toward national earthquake early warning system. *Seismological Society of America*, *91*(6), 3236–3255.

Langbein, J., Murray, J., & Snyder, H. (2006). Coseismic and initial postseismic deformation from the 2004 parkfield, california, earthquake, observed by global positioning system, electronic distance meter, creepmeters, and borehole strainmeters. *Bulletin of the Seismological Society of America*, *96*(4B), S304–S320.

Langbein, J., & Bock, Y. (2004). High-rate real-time gps network at parkfield: Utility for detecting fault slip and seismic displacements. *Geophysical Research Letters*, *31*(15).

Langbein, J., Borcherdt, R., Dreger, D., Fletcher, J., Hardebeck, J. L., Hellweg, M., Ji, C., Johnston, M., Murray, J. R., Nadeau, R., et al. (2005). Preliminary report on the 28 september 2004, m 6.0 parkfield, california earthquake. *Seismological Research Letters*, *76*(1), 10–26.

Larson, K. M. (2009). Gps seismology. *Journal of Geodesy*, *83*(3), 227–233.

Larson, K. M., Bodin, P., & Gomberg, J. (2003). Using 1-hz gps data to measure deformations caused by the denali fault earthquake. *Science*, *300*(5624), 1421–1424.

Laske, G., Masters, G., Ma, Z., & Pasyanos, M. (2013). Update on crust1. 0—a 1-degree global model of earth's crust. *Geophysical research abstracts*, *15*(15), 2658.

Lau, N., Tymofyeyeva, E., & Fialko, Y. (2018). Variations in the long-term uplift rate due to the altiplano–puna magma body observed with sentinel-1 interferometry. *Earth and Planetary Science Letters*, *491*, 43–47.

Lay, T., Ye, L., Kanamori, H., & Satake, K. (2018). Constraining the dip of shallow, shallowly dipping thrust events using long-period love wave radiation patterns: Applications to the 25 october 2010 mentawai, indonesia, and 4 may 2018 hawaii island earthquakes. *Geophysical Research Letters*, *45*(19), 10–342.

Le Beon, M., Klinger, Y., Amrat, A. Q., Agnon, A., Dorbath, L., Baer, G., Ruegg, J.-C., Charade, O., & Mayyas, O. (2008). Slip rate and locking depth from gps profiles across the southern dead sea transform. *Journal of Geophysical Research: Solid Earth*, *113*(B11).

Li, X., Jónsson, S., & Cao, Y. (2021). Interseismic deformation from sentinel-1 burst-overlap interferometry: Application to the southern dead sea fault. *Geophysical Research Letters*, *48*(16), e2021GL093481.

Lienkaemper, J. J., DeLong, S. B., Domrose, C. J., & Rosa, C. M. (2016). Afterslip behavior following the 2014 m 6.0 south napa earthquake with implications for afterslip forecasting on other seismogenic faults. *Seismological Research Letters*, *87*(3), 609–619.

Lin, A., Satsukawa, T., Wang, M., Mohammadi Asl, Z., Fueta, R., & Nakajima, F. (2016). Coseismic rupturing stopped by aso volcano during the 2016 m w 7.1 kumamoto earthquake, japan. *Science*, *354*(6314), 869–874.

Lindsey, E. O., Fialko, Y., Bock, Y., Sandwell, D. T., & Bilham, R. (2014a). Localized and distributed creep along the southern san andreas fault. *Journal of Geophysical Research: Solid Earth*, *119*(10), 7909–7922.

Lindsey, E. O., Natsuaki, R., Xu, X., Shimada, M., Hashimoto, M., Melgar, D., & Sandwell, D. T. (2015). Line-of-sight displacement from alos-2 interferometry: Mw 7.8 gorkha earthquake and mw 7.3 aftershock. *Geophysical Research Letters*, *42*(16), 6655–6661.

Lindsey, E. O., Sahakian, V. J., Fialko, Y., Bock, Y., Barbot, S., & Rockwell, T. K. (2014b). Interseismic strain localization in the san jacinto fault zone. *Pure and Applied Geophysics*, *171*(11), 2937–2954.

Lior, I., & Ziv, A. (2018). The relation between ground motion, earthquake source parameters, and attenuation: Implications for source parameter inversion and ground motion prediction equations. *Journal of Geophysical Research: Solid Earth*, *123*(7), 5886–5901.

Lior, I., Ziv, A., & Madariaga, R. (2016). P-wave attenuation with implications for earthquake early warning. *Bulletin of the Seismological Society of America*, *106*(1), 13–22.

Liu, C., Lay, T., & Xiong, X. (2018). Rupture in the 4 may 2018 mw 6.9 earthquake seaward of the kilauea east rift zone fissure eruption in hawaii. *Geophysical Research Letters*, *45*(18), 9508–9515.

Liu, C., Lay, T., Xiong, X., & Wen, Y. (2020). Rupture of the 2020 mw 7.8 earthquake in the shumagin gap inferred from seismic and geodetic observations. *Geophysical Research Letters*, *47*(22), e2020GL090806.

Liu, L., Jafarov, E. E., Schaefer, K. M., Jones, B. M., Zebker, H. A., Williams, C. A., Rogan, J., & Zhang, T. (2014). Insar detects increase in surface subsidence caused by an arctic tundra fire. *Geophysical research letters*, *41*(11), 3906–3913.

Lorito, S., Romano, F., Atzori, S., Tong, X., Avallone, A., McCloskey, J., Cocco, M., Boschi, E., & Piatanesi, A. (2011). Limited overlap between the seismic gap and coseismic slip of the great 2010 chile earthquake. *Nature Geoscience*, *4*(3), 173–177.

Lyons, S., & Sandwell, D. (2003). Fault creep along the southern san andreas from interferometric synthetic aperture radar, permanent scatterers, and stacking. *Journal of Geophysical Research: Solid Earth*, *108*(B1).

Madariaga, R., Ruiz, S., Rivera, E., Leyton, F., & Baez, J. C. (2019). Near-field spectra of large earthquakes. *Pure and Applied Geophysics*, *176*(3), 983–1001.

Magnani, M. B., Blanpied, M. L., DeShon, H. R., & Hornbach, M. J. (2017). Discriminating between natural versus induced seismicity from long-term deformation history of intraplate faults. *Science advances*, *3*(11), e1701593.

Marco, S., Hartal, M., Hazan, N., Lev, L., & Stein, M. (2003). Archaeology, history, and geology of the ad 749 earthquake, dead sea transform. *Geology*, *31*(8), 665–668.

Marco, S., Stein, M., Agnon, A., & Ron, H. (1996). Long-term earthquake clustering: A 50,000-year paleoseismic record in the dead sea graben. *Journal of Geophysical Research: Solid Earth*, *101*(B3), 6179–6191.

Marone, C. J., Scholtz, C., & Bilham, R. (1991). On the mechanics of earthquake afterslip. *Journal of Geophysical Research: Solid Earth*, *96*(B5), 8441–8452.

Marsan, D. (2005). The role of small earthquakes in redistributing crustal elastic stress. *Geophysical Journal International*, *163*(1), 141–151.

Masson, F., Hamiel, Y., Agnon, A., Klinger, Y., & Deprez, A. (2015). Variable behavior of the dead sea fault along the southern arava segment from gps measurements. *comptes rendus geoscience*, *347*(4), 161–169.

Mattioli, G. S., Phillips, D. A., Hodgkinson, K. M., Walls, C., Mencin, D. J., Bartel, B. A., Charlevoix, D. J., Crosby, C., Gottlieb, M. J., Henderson, B., et al. (2020). The gage data and field response to the 2019 ridgecrest earthquake sequence. *Seismological Research Letters*, *91*(4), 2075–2086.

Mavrommatis, A. P., Segall, P., & Johnson, K. M. (2014). A decadal-scale deformation transient prior to the 2011 mw 9.0 tohoku-oki earthquake. *Geophysical Research Letters*, *41*(13), 4486–4494.

Melbourne, T. I., Szeliga, W. M., Santillan, V. M., & Scrivner, C. W. (2021). Global navigational satellite system seismic monitoring. *Bulletin of the Seismological Society of America*, *111*(3), 1248–1262.

Melgar, D., Allen, R. M., Riquelme, S., Geng, J., Bravo, F., Baez, J. C., Parra, H., Barrientos, S., Fang, P., Bock, Y., et al. (2016). Local tsunami warnings: Perspectives from recent large events. *Geophysical Research Letters*, *43*(3), 1109–1117.

Melgar, D., & Bock, Y. (2015). Kinematic earthquake source inversion and tsunami runup prediction with regional geophysical data. *Journal of Geophysical Research: Solid Earth*, *120*(5), 3324–3349.

Melgar, D., Bock, Y., & Crowell, B. W. (2012). Real-time centroid moment tensor determination for large earthquakes from local and regional displacement records. *Geophysical Journal International*, *188*(2), 703–718.

Melgar, D., Bock, Y., Sanchez, D., & Crowell, B. W. (2013a). On robust and reliable automated baseline corrections for strong motion seismology. *Journal of Geophysical Research: Solid Earth*, *118*(3), 1177–1187.

Melgar, D., Crowell, B. W., Bock, Y., & Haase, J. S. (2013b). Rapid modeling of the 2011 mw 9.0 tohoku-oki earthquake with seismogeodesy. *Geophysical Research Letters*, *40*(12), 2963–2968.

Melgar, D., Crowell, B. W., Geng, J., Allen, R. M., Bock, Y., Riquelme, S., Hill, E. M., Protti, M., & Ganas, A. (2015a). Earthquake magnitude calculation without saturation from the scaling of peak ground displacement. *Geophysical Research Letters*, *42*(13), 5197–5205.

Melgar, D., Geng, J., Crowell, B. W., Haase, J. S., Bock, Y., Hammond, W. C., & Allen, R. M. (2015b). Seismogeodesy of the 2014 mw6. 1 napa earthquake, california: Rapid response and modeling of fast rupture on a dipping strike-slip fault. *Journal of Geophysical Research: Solid Earth*, *120*(7), 5013–5033.

Melgar, D., & Hayes, G. P. (2019). Characterizing large earthquakes before rupture is complete. *Science Advances*, *5*(5), eaav2032.

Migowski, C., Agnon, A., Bookman, R., Negendank, J. F., & Stein, M. (2004). Recurrence pattern of holocene earthquakes along the dead sea transform revealed by varve-counting and radiocarbon dating of lacustrine sediments. *Earth and Planetary Science Letters*, *222*(1), 301–314.

Milliner, C., Bürgmann, R., Inbal, A., Wang, T., & Liang, C. (2020). Resolving the kinematics and moment release of early afterslip within the first hours following the 2016 mw 7.1 kumamoto earthquake: Implications for the shallow slip deficit and frictional behavior of aseismic creep. *Journal of Geophysical Research: Solid Earth*, *125*(9), e2019JB018928.

Minson, S. E., Baltay, A. S., Cochran, E. S., Hanks, T. C., Page, M. T., McBride, S. K., Milner, K. R., & Meier, M.-A. (2019). The limits of earthquake early warning accuracy and best alerting strategy. *Scientific reports*, *9*(1), 1–13.

Minson, S. E., Murray, J. R., Langbein, J. O., & Gomberg, J. S. (2014a). Real-time inversions for finite fault slip models and rupture geometry based on high-rate gps data. *Journal of Geophysical Research: Solid Earth*, *119*(4), 3201–3231.

Minson, S. E., Simons, M., Beck, J., Ortega, F., Jiang, J., Owen, S., Moore, A., Inbal, A., & Sladen, A. (2014b). Bayesian inversion for finite fault earthquake source models–ii: The 2011 great tohoku-oki, japan earthquake. *Geophysical Journal International*, *198*(2), 922–940.

Miyazaki, S., Larson, K. M., Choi, K., Hikima, K., Koketsu, K., Bodin, P., Haase, J., Emore, G., & Yamagiwa, A. (2004). Modeling the rupture process of the 2003 september 25 tokachi-oki (hokkaido) earthquake using 1-hz gps data. *Geophysical Research Letters*, *31*(21).

Miyazaki, S., McGuire, J. J., & Segall, P. (2011). Seismic and aseismic fault slip before and during the 2011 off the pacific coast of tohoku earthquake. *Earth, planets and space*, *63*(7), 637–642.

Mizoguchi, K., Uehara, S.-i., & Ueta, K. (2012). Surface fault ruptures and slip distributions of the m w 6.6 11 april 2011 hamadoori, fukushima prefecture, northeast japan, earthquake. *Bulletin of the Seismological Society of America*, *102*(5), 1949–1956.

Mori, N., Takahashi, T., Yasuda, T., & Yanagisawa, H. (2011). Survey of 2011 tohoku earthquake tsunami inundation and run-up. *Geophysical research letters*, *38*(7).

Murray, J. R., Bartlow, N., Bock, Y., Brooks, B. A., Foster, J., Freymueller, J., Hammond, W. C., Hodgkinson, K., Johanson, I., López-Venegas, A., et al. (2019). Regional global navigation satellite system networks for crustal deformation monitoring. *Seismological Research Letters*, *91*(2A), 552–572.

Myer, D., Sandwell, D., Brooks, B., Foster, J., & Shimada, M. (2008). Inflation along kilauea's southwest rift zone in 2006. *Journal of Volcanology and Geothermal Research*, *177*(2), 418–424.

Nadeau, R. M., Michelini, A., Uhrhammer, R. A., Dolenc, D., & McEvilly, T. V. (2004). Detailed kinematics, structure and recurrence of micro-seismicity in the safod target region. *Geophysical Research Letters*, *31*(12).

Nikolaidis, R. M., Bock, Y., de Jonge, P. J., Shearer, P., Agnew, D. C., & Van Domselaar, M. (2001). Seismic wave observations with the global positioning system. *Journal of Geophysical Research: Solid Earth*, *106*(B10), 21897–21916.

Nof, R. N., Abelson, M., Raz, E., Magen, Y., Atzori, S., Salvi, S., & Baer, G. (2019). Sar interferometry for sinkhole early warning and susceptibility assessment along the dead sea, israel. *Remote Sensing*, *11*(1), 89.

Nof, R. N., & Allen, R. M. (2016). Implementing the elarms earthquake early warning algorithm on the israeli seismic networkimplementing the elarms earthquake early warning algorithm on the israeli seismic network. *Bulletin of the Seismological Society of America*, *106*(5), 2332–2344.

Nof, R. N., Baer, G., Eyal, Y., & Novali, F. (2008). Current surface displacement along the carmel fault system in israel from insar stacking and psinsar. *Israel Journal of Earth Sciences*, *57*(2).

Nof, R. N., & Kurzon, I. (2021). Truaa—earthquake early warning system for israel: Implementation and current status. *Seismological Research Letters*, *92*(1), 325–341.

Nof, R. N., Lior, I., & Kurzon, I. (2021). Earthquake early warning system in israel—towards an operational stage. *Frontiers in Earth Science*, 452.

Nof, R., Ziv, A., Doin, M.-P., Baer, G., Fialko, Y., Wdowinski, S., Eyal, Y., & Bock, Y. (2012). Rising of the lowest place on earth due to dead sea water-level drop: Evidence from sar interferometry and gps. *Journal of Geophysical Research: Solid Earth*, *117*(B5).

Nykolaishen, L., Dragert, H., Wang, K., James, T. S., & Schmidt, M. (2015). Gps observations of crustal deformation associated with the 2012 m w 7.8 haida gwaii earthquake. *Bulletin of the Seismological Society of America*, *105*(2B), 1241–1252.

Ohta, Y., Hino, R., Inazu, D., Ohzono, M., Ito, Y., Mishina, M., Iinuma, T., Nakajima, J., Osada, Y., Suzuki, K., et al. (2012). Geodetic constraints on afterslip characteristics following the march 9, 2011, sanriku-oki earthquake, japan. *Geophysical research letters*, *39*(16).

Okada, Y. (1985). Surface deformation due to shear and tensile faults in a half-space. *Bulletin of the seismological society of America*, *75*(4), 1135–1154.

Okada, Y., Kasahara, K., Hori, S., Obara, K., Sekiguchi, S., Fujiwara, H., & Yamamoto, A. (2004). Recent progress of seismic observation networks in japan—hi-net, f-net, k-net and kik-net—. *Earth, Planets and Space*, *56*(8), xv–xxviii.

Okal, E. A., Fritz, H. M., Synolakis, C. E., Borrero, J. C., Weiss, R., Lynett, P. J., Titov, V. V., Foteinis, S., Jaffe, B. E., Liu, P. L.-F., et al. (2010). Field survey of the samoa tsunami of 29 september 2009. *Seismological Research Letters*, *81*(4), 577–591.

O'Toole, T. B., Valentine, A. P., & Woodhouse, J. H. (2013). Earthquake source parameters from gps-measured static displacements with potential for real-time application. *Geophysical research letters*, *40*(1), 60–65.

Ou, Q., Daout, S., Weiss, J., Shen, L., Lazeckỳ, M., Wright, T., & Parsons, B. (2022). Large-scale interseismic strain mapping of the ne tibetan plateau from sentinel-1 interferometry. *Journal of Geophysical Research: Solid Earth*, e2022JB024176.

Ozawa, S., Nishimura, T., Suito, H., Kobayashi, T., Tobita, M., & Imakiire, T. (2011). Coseismic and postseismic slip of the 2011 magnitude-9 tohoku-oki earthquake. *Nature*, *475*(7356), 373–376.

Pagani, C., Bodin, T., Métois, M., & Lasserre, C. (2021). Bayesian estimation of surface strain rates from global navigation satellite system measurements: Application to the southwestern united states. *Journal of Geophysical Research: Solid Earth*, *126*(6), e2021JB021905.

Page, M., & Felzer, K. (2015). Southern san andreas fault seismicity is consistent with the gutenberg–richter magnitude–frequency distribution. *Bulletin of the Seismological Society of America*, *105*(4), 2070–2080.

Peltzer, G., Rosen, P., Rogez, F., & Hudnut, K. (1998). Poroelastic rebound along the landers 1992 earthquake surface rupture. *Journal of Geophysical Research: Solid Earth*, *103*(B12), 30131–30145.

Peña, C., Metzger, S., Heidbach, O., Bedford, J., Bookhagen, B., Moreno, M., Oncken, O., & Cotton, F. (2022). Role of poroelasticity during the early postseismic deformation of the 2010 maule megathrust earthquake. *Geophysical Research Letters*, e2022GL098144.

Polet, J., & Kanamori, H. (2000). Shallow subduction zone earthquakes and their tsunamigenic potential. *Geophysical Journal International*, *142*(3), 684–702.

Pollitz, F. F., Brooks, B., Tong, X., Bevis, M. G., Foster, J. H., Bürgmann, R., Smalley Jr, R., Vigny, C., Socquet, A., Ruegg, J.-C., et al. (2011). Coseismic slip distribution of the february 27, 2010 mw 8.8 maule, chile earthquake. *Geophysical Research Letters*, *38*(9).

Pollitz, F. F., Murray, J. R., Svarc, J. L., Wicks, C., Roeloffs, E., Minson, S. E., Scharer, K., Kendrick, K., Hudnut, K. W., Nevitt, J., et al. (2020). Kinematics of fault slip associated with the 4–6 july 2019 ridgecrest, california, earthquake sequence. *Bulletin of the Seismological Society of America*, *110*(4), 1688–1700.

Ponti, D. J., Blair, J. L., Rosa, C. M., Thomas, K., Pickering, A. J., Akciz, S., Angster, S., Avouac, J.-P., Bachhuber, J., Bacon, S., et al. (2020). Documentation of surface fault rupture and ground-deformation features produced by the 4 and 5 july 2019 mw 6.4 and mw 7.1 ridgecrest earthquake sequence. *Seismological Research Letters*, *91*(5), 2942–2959.

Prieto, G. A., Shearer, P. M., Vernon, F. L., & Kilb, D. (2004). Earthquake source scaling and self-similarity estimation from stacking p and s spectra. *Journal of Geophysical Research: Solid Earth*, *109*(B8).

Ragon, T., Sladen, A., Bletery, Q., Vergnolle, M., Cavalié, O., Avallone, A., Balestra, J., & Delouis, B. (2019). Joint inversion of coseismic and early postseismic slip to optimize the information content in geodetic data: Application to the 2009 m w 6.3 l'aquila earthquake, central italy. *Journal of Geophysical Research: Solid Earth*, *124*(10), 10522–10543.

Reinking, J., Smit-Philipp, H., & Even-Tzur, G. (2011). Surface deformation along the carmel fault system, israel. *Journal of Geodynamics*, *52*(3-4), 321–331.

Ribot, M., Klinger, Y., Jónsson, S., Avsar, U., Pons-Branchu, E., Matrau, R., & Mallon, F. L. (2021). Active faults' geometry in the gulf of aqaba, southern dead sea fault, illuminated by multibeam bathymetric data. *Tectonics*, *40*(4), e2020TC006443.

Riquelme, S., Bravo, F., Melgar, D., Benavente, R., Geng, J., Barrientos, S., & Campos, J. (2016). W phase source inversion using high-rate regional gps data for large earthquakes. *Geophysical Research Letters*, *43*(7), 3178–3185.

Riquelme, S., Medina, M., Bravo, F., Barrientos, S., Campos, J., & Cisternas, A. (2018). W-phase real-time implementation and network expansion from 2012 to 2017: The experience in chile. *Seismological Research Letters*, *89*(6), 2237–2248.

Rivera, L., & Kanamori, H. (2009). Using w phase for regional tsunami warning and rapid earthquake hazard assessment. *The 2nd International Workshop on Earthquake Early Warning*.

Rogers, G., & Dragert, H. (2003). Episodic tremor and slip on the cascadia subduction zone: The chatter of silent slip. *science*, *300*(5627), 1942–1943.

Rollins, C., Barbot, S., & Avouac, J.-P. (2015). Postseismic deformation following the 2010 m=7.2 el mayor-cucapah earthquake: Observations, kinematic inversions, and dynamic models. *Pure and Applied Geophysics*, *172*(5), 1305–1358.

Rosi, A., Tofani, V., Tanteri, L., Tacconi Stefanelli, C., Agostini, A., Catani, F., & Casagli, N. (2018). The new landslide inventory of tuscany (italy) updated with ps-insar: Geomorphological features and landslide distribution. *Landslides*, *15*(1), 5–19.

Ross, Z. E., Rollins, C., Cochran, E. S., Hauksson, E., Avouac, J.-P., & Ben-Zion, Y. (2017). Aftershocks driven by afterslip and fluid pressure sweeping through a fault-fracture mesh. *Geophysical Research Letters*, *44*(16), 8260–8267.

Ross, Z. E., Trugman, D. T., Hauksson, E., & Shearer, P. M. (2019). Searching for hidden earthquakes in southern california. *Science*, *364*(6442), 767–771.

Rubin, A. M., & Ampuero, J.-P. (2005). Earthquake nucleation on (aging) rate and state faults. *Journal of Geophysical Research: Solid Earth*, *110*(B11).

Ruhl, C. J., Melgar, D., Geng, J., Goldberg, D. E., Crowell, B. W., Allen, R. M., Bock, Y., Barrientos, S., Riquelme, S., Baez, J. C., et al. (2019). A global database of strong-motion displacement gnss recordings and an example application to pgd scaling. *Seismological Research Letters*, *90*(1), 271–279.

Sadeh, M., Hamiel, Y., Ziv, A., Bock, Y., Fang, P., & Wdowinski, S. (2012). Crustal deformation along the dead sea transform and the carmel fault inferred from 12 years of gps measurements. *Journal of Geophysical Research: Solid Earth*, *117*(B8).

Sagiya, T. (2004). A decade of geonet: 1994-2003 the continuous gps observation in japan and its impact on earthquake studies. *Earth, planets and space*, *56*(8), xxix–xli.

Sagiya, T., Miyazaki, S., & Tada, T. (2000). Continuous gps array and present-day crustal deformation of japan. *Pure and applied Geophysics*, *157*(11), 2303–2322.

Salditch, L., Stein, S., Neely, J., Spencer, B. D., Brooks, E. M., Agnon, A., & Liu, M. (2020). Earthquake supercycles and long-term fault memory. *Tectonophysics*, *774*, 228289.

Sandwell, D., Mellors, R., Tong, X., Wei, M., & Wessel, P. (2011). Gmtsar: An insar processing system based on generic mapping tools.

Sandwell, D. T., Sichoix, L., Agnew, D., Bock, Y., & Minster, J.-B. (2000). Near real-time radar interferometry of the mw 7.1 hector mine earthquake. *Geophysical Research Letters*, *27*(19), 3101–3104.

Sandwell, D. T., & Wessel, P. (2016). Interpolation of 2-d vector data using constraints from elasticity. *Geophysical Research Letters*, *43*(20), 10–703.

Sato, M., Fujita, M., Matsumoto, Y., Ishikawa, T., Saito, H., Mochizuki, M., & Asada, A. (2013). Interplate coupling off northeastern japan before the 2011 tohoku-oki earthquake, inferred from seafloor geodetic data. *Journal of Geophysical Research: Solid Earth*, *118*(7), 3860–3869.

Satriano, C., Kiraly, E., Bernard, P., & Vilotte, J.-P. (2012). The 2012 mw 8.6 sumatra earthquake: Evidence of westward sequential seismic ruptures associated to the reactivation of a n-s ocean fabric. *Geophysical Research Letters*, *39*(15).

Saunders, J. K., Goldberg, D. E., Haase, J. S., Bock, Y., Offield, D. G., Melgar, D., Restrepo, J., Fleischman, R. B., Nema, A., Geng, J., et al. (2016). Seismogeodesy using gps and low-cost mems accelerometers: Perspectives for earthquake early warning and rapid response. *Bulletin of the Seismological Society of America*, *106*(6), 2469–2489.

Savage, J., & Burford, R. (1973). Geodetic determination of relative plate motion in central california. *Journal of Geophysical Research*, *78*(5), 832–845.

Schmedes, J., & Archuleta, R. J. (2008). Near-source ground motion along strike-slip faults: Insights into magnitude saturation of pgv and pga. *Bulletin of the Seismological Society of America*, *98*(5), 2278–2290.

Scott, E. (2021). Strike-slip tsunamis. *Nature Reviews Earth & Environment*, *2*(6), 379–379.

Shao, G., Ji, C., & Zhao, D. (2011). Rupture process of the 9 march, 2011 mw 7.4 sanriku-oki, japan earthquake constrained by jointly inverting teleseismic waveforms, strong motion data and gps observations. *Geophysical Research Letters*, *38*(7).

Sharon, M., Sagy, A., Kurzon, I., Marco, S., & Rosensaft, M. (2020). Assessment of seismic sources and capable faults through hierarchic tectonic criteria: Implications for seismic hazard in the levant. *Natural Hazards and Earth System Sciences*, *20*(1), 125–148.

Shelly, D. R. (2020). A high-resolution seismic catalog for the initial 2019 ridgecrest earthquake sequence: Foreshocks, aftershocks, and faulting complexity. *Seismological Research Letters*, *91*(4), 1971–1978.

Shen, Z.-K., Jackson, D. D., Feng, Y., Cline, M., Kim, M., Fang, P., & Bock, Y. (1994). Postseismic deformation following the landers earthquake, california, 28 june 1992. *Bulletin of the Seismological Society of America*, *84*(3), 780–791.

Shen, Z.-K., Wang, M., Zeng, Y., & Wang, F. (2015). Optimal interpolation of spatially discretized geodetic data. *Bulletin of the Seismological Society of America*, *105*(4), 2117–2127.

Shirahama, Y., Yoshimi, M., Awata, Y., Maruyama, T., Azuma, T., Miyashita, Y., Mori, H., Imanishi, K., Takeda, N., Ochi, T., et al. (2016). Characteristics of the surface ruptures

associated with the 2016 kumamoto earthquake sequence, central kyushu, japan. *Earth, Planets and Space*, *68*(1), 1–12.

Shirzaei, M., & Bürgmann, R. (2013). Time-dependent model of creep on the hayward fault from joint inversion of 18 years of insar and surface creep data. *Journal of Geophysical Research: Solid Earth*, *118*(4), 1733–1746.

Shrivastava, M. N., González, G., Moreno, M., Chlieh, M., Salazar, P., Reddy, C., Báez, J. C., Yáñez, G., González, J., & de la Llera, J. C. (2016). Coseismic slip and afterslip of the 2015 mw 8.3 illapel (chile) earthquake determined from continuous gps data. *Geophysical Research Letters*, *43*(20), 10–710.

Simons, M., Minson, S. E., Sladen, A., Ortega, F., Jiang, J., Owen, S. E., Meng, L., Ampuero, J.-P., Wei, S., Chu, R., et al. (2011). The 2011 magnitude 9.0 tohoku-oki earthquake: Mosaicking the megathrust from seconds to centuries. *science*, *332*(6036), 1421–1425.

Smyth, A., & Wu, M. (2007). Multi-rate kalman filtering for the data fusion of displacement and acceleration response measurements in dynamic system monitoring. *Mechanical Systems and Signal Processing*, *21*(2), 706–723.

Stein, R. S. (1999). The role of stress transfer in earthquake occurrence. *Nature*, *402*(6762), 605–609.

Styron, R., & Pagani, M. (2020). The gem global active faults database. *Earthquake Spectra*, *36*(1_suppl), 160–180.

Sun, Q., Zhang, L., Ding, X., Hu, J., Li, Z., & Zhu, J. (2015). Slope deformation prior to zhouqu, china landslide from insar time series analysis. *Remote Sensing of Environment*, *156*, 45–57.

Tanioka, Y., Ruff, L., & Satake, K. (1997). What controls the lateral variation of large earthquake occurrence along the japan trench? *Island Arc*, *6*(3), 261–266.

Toda, S., & Tsutsumi, H. (2013). Simultaneous reactivation of two, subparallel, inland normal faults during the m w 6.6 11 april 2011 iwaki earthquake triggered by the m w 9.0

tohoku-oki, japan, earthquake. *Bulletin of the Seismological Society of America*, *103*(2B), 1584–1602.

Tong, X., Sandwell, D., & Schmidt, D. (2018). Surface creep rate and moment accumulation rate along the aceh segment of the sumatran fault from l-band alos-1/palsar-1 observations. *Geophysical Research Letters*, *45*(8), 3404–3412.

Tong, X., Sandwell, D., & Smith-Konter, B. (2013). High-resolution interseismic velocity data along the san andreas fault from gps and insar. *Journal of Geophysical Research: Solid Earth*, *118*(1), 369–389.

Tong, X., Sandwell, D., Luttrell, K., Brooks, B., Bevis, M., Shimada, M., Foster, J., Smalley Jr, R., Parra, H., Báez Soto, J. C., et al. (2010). The 2010 maule, chile earthquake: Downdip rupture limit revealed by space geodesy. *Geophysical Research Letters*, *37*(24).

Tong, X., Smith-Konter, B., & Sandwell, D. T. (2014). Is there a discrepancy between geological and geodetic slip rates along the san andreas fault system? *Journal of Geophysical Research: Solid Earth*, *119*(3), 2518–2538.

Torres, R., Snoeij, P., Geudtner, D., Bibby, D., Davidson, M., Attema, E., Potin, P., Rommen, B., Floury, N., Brown, M., et al. (2012). Gmes sentinel-1 mission. *Remote sensing of environment*, *120*, 9–24.

Trugman, D. T., Page, M. T., Minson, S. E., & Cochran, E. S. (2019). Peak ground displacement saturates exactly when expected: Implications for earthquake early warning. *Journal of Geophysical Research: Solid Earth*, *124*(5), 4642–4653.

Tsuboi, S., Abe, K., Takano, K., & Yamanaka, Y. (1995). Rapid determination of mw from broadband p waveforms. *Bulletin of the Seismological Society of America*, *85*(2), 606–613.

Tsuboi, S., Whitmore, P. M., & Sokolowski, T. J. (1999). Application of m wp to deep and teleseismic earthquakes. *Bulletin of the Seismological Society of America*, *89*(5), 1345–1351.

Turcotte, D. L., & Schubert, G. (2002). *Geodynamics*. Cambridge university press.

Turner, R. C., Nadeau, R. M., & Bürgmann, R. (2013). Aseismic slip and fault interaction from repeating earthquakes in the loma prieta aftershock zone. *Geophysical Research Letters*, *40*(6), 1079–1083.

Twardzik, C., Vergnolle, M., Sladen, A., & Avallone, A. (2019). Unravelling the contribution of early postseismic deformation using sub-daily gnss positioning. *Scientific reports*, *9*(1), 1–12.

Tymofyeyeva, E., & Fialko, Y. (2015). Mitigation of atmospheric phase delays in insar data, with application to the eastern california shear zone. *Journal of Geophysical Research: Solid Earth*, *120*(8), 5952–5963.

Tymofyeyeva, E., & Fialko, Y. (2018). Geodetic evidence for a blind fault segment at the southern end of the san jacinto fault zone. *Journal of Geophysical Research: Solid Earth*, *123*(1), 878–891.

Tymofyeyeva, E., Fialko, Y., Jiang, J., Xu, X., Sandwell, D., Bilham, R., Rockwell, T. K., Blanton, C., Burkett, F., Gontz, A., et al. (2019). Slow slip event on the southern san andreas fault triggered by the 2017 m w 8.2 chiapas (mexico) earthquake. *Journal of Geophysical Research: Solid Earth*, *124*(9), 9956–9975.

Vey, S., Al-Halbouni, D., Haghighi, M. H., Alshawaf, F., Vüllers, J., Güntner, A., Dick, G., Ramatschi, M., Teatini, P., Wickert, J., et al. (2021). Delayed subsidence of the dead sea shore due to hydro-meteorological changes. *Scientific reports*, *11*(1), 1–10.

Waldhauser, F., & Schaff, D. P. (2008). Large-scale relocation of two decades of northern california seismicity using cross-correlation and double-difference methods. *Journal of Geophysical Research: Solid Earth*, *113*(B8).

Wang, D., Becker, N. C., Walsh, D., Fryer, G. J., Weinstein, S. A., McCreery, C. S., Sardiña, V., Hsu, V., Hirshorn, B. F., Hayes, G. P., et al. (2012a). Real-time forecasting of the april 11, 2012 sumatra tsunami. *Geophysical Research Letters*, *39*(19).

Wang, K., & Bürgmann, R. (2020). Co-and early postseismic deformation due to the 2019 ridgecrest earthquake sequence constrained by sentinel-1 and cosmo-skymed sar data. *Seismological Research Letters*, *91*(4), 1998–2009.

Wang, K., Hu, Y., & He, J. (2012b). Deformation cycles of subduction earthquakes in a viscoelastic earth. *Nature*, *484*(7394), 327–332.

Wdowinski, S., Bock, Y., Baer, G., Prawirodirdjo, L., Bechor, N., Naaman, S., Knafo, R., Forrai, Y., & Melzer, Y. (2004). Gps measurements of current crustal movements along the dead sea fault. *Journal of Geophysical Research: Solid Earth*, *109*(B5).

Weber, M., Abu-Ayyash, K., Abueladas, A., Agnon, A., Alasonati-Tašárová, Z., Al-Zubi, H., Babeyko, A., Bartov, Y., Bauer, K., Becken, M., et al. (2009). Anatomy of the dead sea transform from lithospheric to microscopic scale. *Reviews of Geophysics*, *47*(2).

Wei, M., Sandwell, D., & Fialko, Y. (2009). A silent mw 4.7 slip event of october 2006 on the superstition hills fault, southern california. *Journal of Geophysical Research: Solid Earth*, *114*(B7).

Wei, M., Sandwell, D., & Smith-Konter, B. (2010). Optimal combination of insar and gps for measuring interseismic crustal deformation. *Advances in Space Research*, *46*(2), 236–249.

Wei, S., Fielding, E., Leprince, S., Sladen, A., Avouac, J.-P., Helmberger, D., Hauksson, E., Chu, R., Simons, M., Hudnut, K., et al. (2011). Superficial simplicity of the 2010 el mayor–cucapah earthquake of baja california in mexico. *Nature geoscience*, *4*(9), 615–618.

Weiss, J., Walters, R., Wright, T., Morishita, Y., Lazecky, M., Wang, H., Hussain, E., & Hooper, A. (2020). Measuring anatolian plate velocity and strain with sentinel-1 insar and gnss data: Implications for fault locking, seismic hazard, and crustal dynamics. *EGU General Assembly Conference Abstracts*, 11156.

Wessel, P., & Smith, W. H. (1998). New, improved version of generic mapping tools released. *Eos, Transactions American Geophysical Union*, *79*(47), 579–579.

Wessel, P., Smith, W. H., Scharroo, R., Luis, J., & Wobbe, F. (2013). Generic mapping tools: Improved version released. *Eos, Transactions American Geophysical Union*, *94*(45), 409–410.

Wetzler, N., & Kurzon, I. (2016). The earthquake activity of israel: Revisiting 30 years of local and regional seismic records along the dead sea transform. *Seismological Research Letters*, *87*(1), 47–58.

Whitmore, P. M., Tsuboi, S., Hirshorn, B., & Sokolowski, T. J. (2002). Magnitude-dependent correction for mwp. *Science of Tsunami Hazards*.

Williams, R. T., Goodwin, L. B., Sharp, W. D., & Mozley, P. S. (2017). Reading a 400,000-year record of earthquake frequency for an intraplate fault. *Proceedings of the National Academy of Sciences*, *114*(19), 4893–4898.

Withers, M., Aster, R., Young, C., Beiriger, J., Harris, M., Moore, S., & Trujillo, J. (1998). A comparison of select trigger algorithms for automated global seismic phase and event detection. *Bulletin of the Seismological Society of America*, *88*(1), 95–106.

Wright, T. J., Houlié, N., Hildyard, M., & Iwabuchi, T. (2012). Real-time, reliable magnitudes for large earthquakes from 1 hz gps precise point positioning: The 2011 tohoku-oki (japan) earthquake. *Geophysical research letters*, *39*(12).

Xiao, Z., Freymueller, J. T., Grapenthin, R., Elliott, J. L., Drooff, C., & Fusso, L. (2021). The deep shumagin gap filled: Kinematic rupture model and slip budget analysis of the 2020 mw 7.8 simeonof earthquake constrained by gnss, global seismic waveforms, and floating insar. *Earth and Planetary Science Letters*, *576*, 117241.

Xu, P., Shu, Y., Liu, J., Nishimura, T., Shi, Y., & Freymueller, J. T. (2019). A large scale of apparent sudden movements in japan detected by high-rate gps after the 2011 tohoku mw9. 0 earthquake: Physical signals or unidentified artifacts? *Earth, Planets and Space*, *71*(1), 1–16.

Xu, X., Sandwell, D. T., Klein, E., & Bock, Y. (2021). Integrated sentinel-1 insar and gnss time-series along the san andreas fault system. *Journal of Geophysical Research: Solid Earth*, *126*(11), e2021JB022579.

Xu, X., Sandwell, D. T., & Smith-Konter, B. (2020a). Coseismic displacements and surface fractures from sentinel-1 insar: 2019 ridgecrest earthquakes. *Seismological Research Letters*, *91*(4), 1979–1985.

Xu, X., Sandwell, D. T., Tymofyeyeva, E., Gonzalez-Ortega, A., & Tong, X. (2017). Tectonic and anthropogenic deformation at the cerro prieto geothermal step-over revealed by sentinel-1a insar. *IEEE Transactions on Geoscience and Remote Sensing*, *55*(9), 5284–5292.

Xu, X., Sandwell, D. T., Ward, L. A., Milliner, C. W., Smith-Konter, B. R., Fang, P., & Bock, Y. (2020b). Surface deformation associated with fractures near the 2019 ridgecrest earthquake sequence. *Science*, *370*(6516), 605–608.

Xu, X., Tong, X., Sandwell, D. T., Milliner, C. W., Dolan, J. F., Hollingsworth, J., Leprince, S., & Ayoub, F. (2016). Refining the shallow slip deficit. *Geophysical Journal International*, *204*(3), 1867–1886.

Yagi, Y., Okuwaki, R., Enescu, B., Kasahara, A., Miyakawa, A., & Otsubo, M. (2016). Rupture process of the 2016 kumamoto earthquake in relation to the thermal structure around aso volcano. *Earth, Planets and Space*, *68*(1), 1–6.

Yague-Martinez, N., Prats-Iraola, P., Pinheiro, M., & Jaeger, M. (2019). Exploitation of burst overlapping areas of tops data. application to sentinel-1. *IGARSS 2019-2019 IEEE International Geoscience and Remote Sensing Symposium*, 2066–2069.

Ye, L., Lay, T., Kanamori, H., & Rivera, L. (2016). Rupture characteristics of major and great (mw 7.0) megathrust earthquakes from 1990 to 2015: 1. source parameter scaling relationships. *Journal of Geophysical Research: Solid Earth*, *121*(2), 826–844.

Yokota, Y., Ishikawa, T., & Watanabe, S.-i. (2018). Seafloor crustal deformation data along the subduction zones around japan obtained by gnss-a observations. *Scientific data*, *5*(1), 1–11.

Yue, H., Ross, Z. E., Liang, C., Michel, S., Fattahi, H., Fielding, E., Moore, A., Liu, Z., & Jia, B. (2017). The 2016 kumamoto mw= 7.0 earthquake: A significant event in a fault–volcano system. *Journal of Geophysical Research: Solid Earth*, *122*(11), 9166–9183.

Zakharova, O., Hainzl, S., & Bach, C. (2013). Seismic moment ratio of aftershocks with respect to main shocks. *Journal of Geophysical Research: Solid Earth*, *118*(11), 5856–5864.

Zeng, Y., & Shen, Z.-K. (2017). A fault-based model for crustal deformation in the western united states based on a combined inversion of gps and geologic inputsa fault-based model for crustal deformation in the wus based on a combined inversion of gps. *Bulletin of the Seismological Society of America*, *107*(6), 2597–2612.

Zhang, J., Zhao, B., Wang, D., Yu, J., & Tan, K. (2021). Dynamic modeling of postseismic deformation following the 2015 mw 7.8 gorkha earthquake, nepal. *Journal of Asian Earth Sciences*, *215*, 104781.

Zhang, M., Ellsworth, W. L., & Beroza, G. C. (2019). Rapid earthquake association and location. *Seismological Research Letters*, *90*(6), 2276–2284.

Zohar, M., & Marco, S. (2012). Re-estimating the epicenter of the 1927 jericho earthquake using spatial distribution of intensity data. *Journal of Applied Geophysics*, *82*, 19–29.

Zumberge, J., Heflin, M., Jefferson, D., Watkins, M., & Webb, F. (1997). Precise point positioning for the efficient and robust analysis of gps data from large networks. *Journal of geophysical research: solid earth*, *102*(B3), 5005–5017.